

MULTISCALE MODELING OF HEALTHY AND DISEASED HUMAN AIRWAYS

by

PARYA AGHASAFARI

(Under the Direction of Ramana Pidaparti)

ABSTRACT

The human respiratory system is a series of organs responsible for taking in oxygen and expelling carbon dioxide. The human lung is the main organ for gas exchange in the human respiratory system and starts from the trachea and ends at the alveoli. During our lifetime different factors might influence the functionality of lung such as; respiratory disease and aging. Complex morphology of the lung causes difficulty in diagnosis and visual interpretation of respiratory disease and age-related changes. In addition, pulmonary function tests are not very sensitive measures of lung disease specifically in early stages of respiratory diseases and we can not repeat the tests to confirm decisive assumption. Moreover, respiratory diseases lead to lung failure, where patients often need mechanical ventilation (MV) devices to assist them in breathing. Many important decisions have to be made once it is determined that a patient needs MV and specialists have to setup proper MV protocols to reduce ventilator induced lung injury (VILI). Hence, computational techniques provide attractive and cost-effective alternative to repeating experimental tests. The main purposes of this dissertation are first developing computational models at different scales and integrating them to investigate influence of life threatening respiratory disease and aging on breathing condition and lung failure. Second, optimizing ventilator protocols specifically for older patients to reduce VILI.

INDEX WORDS: Human lung, Respiratory disease, Aging, Multiscale model, Mechanical ventilation

MULTISCALE MODELING OF HEALTHY AND DISEASED HUMAN AIRWAYS

by

PARYA AGHASAFARI

B.S., Iran University of Science & Technology, Iran, 2011

M.S., Isfahan University of Technology, Iran, 2013

A Dissertation Submitted to the Graduate Faculty
of The University of Georgia in Partial Fulfillment

of the

Requirements for the Degree

DOCTOR OF PHILOSOPHY

ATHENS, GEORGIA

2018

© 2018

Parya Aghasafari

All Rights Reserved

MULTISCALE MODELING OF HEALTHY AND DISEASED HUMAN AIRWAYS

by

PARYA AGHASAFARI

Approved:

Major Professor: Ramana Pidaparti

Committee: K. Melissa Hallow
Xianqiao Wang
Ben Davis

Electronic Version Approved:

Suzanne Barbour
Dean of the Graduate School
The University of Georgia
August 2018

DEDICATION

To my inspiring parents

Behrouz and Tooran

For their love, endless support, encouragement and sacrifices. I would not be where I am today without their support.

ACKNOWLEDGMENTS

I would like to express my special appreciation and thanks to my advisor, Prof. Ramana Pidaparti for his tremendous support, encouragement, and mentorship. I have been extremely lucky to have a supervisor who cared so much about my research.

I would like to thank my thesis committee members: Dr. K. Mellisa Hallow, Dr. Xianqiao Wang, and Dr. Ben Davis, for all of their guidance through this process; their discussion, ideas, and feedback have been absolutely invaluable.

I am truly grateful to my parents for their endless love and support. They have always encouraged and supported me to pursue my dreams. I would like to thank my fiance Ramin for his support, encouragement throughout my PhD. I would like also to thank my sisters and brothers who have always loved and supported me unconditionally.

TABLE OF CONTENTS

	Page
ACKNOWLEDGMENTS	v
LIST OF FIGURES	viii
LIST OF TABLES	xii
CHAPTER	
1 INTRODUCTION AND LITERATURE REVIEW	1
2 INFLUENCE OF TIDAL-VOLUME SETTING, EMPHYSEMA AND ARDS ON HUMAN ALVEOLAR SACS	6
2.1 INTRODUCTION	7
2.2 METHODS	10
2.3 RESULTS	16
2.4 CONCLUSION	22
3 AGING EFFECTS ON ALVEOLAR SACS UNDER MECHANICAL VENTILATION	24
3.1 INTRODUCTION	25
3.2 FSI APPROACH	28
3.3 VOLUME-CONTROLLED VENTILATION MODE	29
3.4 PRESSURE-CONTROLLED VENTILATION MODE	32
3.5 STATISTICAL ANALYSIS	32
3.6 SENSITIVITY ANALYSIS	33
3.7 RESULTS	34
3.8 LIMITATIONS	42

3.9	CONCLUSIONS	43
4	FRactal Geometrical and Structural Properties of Normal and Diseased Bronchial Tree with Age	44
4.1	INTRODUCTION	45
4.2	METHODS	47
4.3	EQUIVALENT ELECTRICAL MODEL FOR BRONCHIAL TREE	48
4.4	RESULTS	50
4.5	CONCLUSION	55
5	Strain-Induced Inflammation in Pulmonary Alveolar Tissue due to Mechanical Ventilation	56
5.1	INTRODUCTION	57
5.2	MATERIALS AND METHODS	59
5.3	CELLULAR AUTOMATA	65
5.4	RESULTS AND DISCUSSION	74
5.5	DISCUSSION	84
5.6	CONCLUSION	87
6	CONCLUSION AND FUTURE WORK	89
	BIBLIOGRAPHY	93
	APPENDIX	
A	SUPPLEMENTAL MATERIALS FOR CHAPTER 3	
	AGING EFFECTS ON ALVEOLAR SACS UNDER MECHANICAL VENTILATION	110

LIST OF FIGURES

2.1	a) Case (1) methodology b) Case (2) methodology.	11
2.2	Case studies a) Healthy alveolar sac model without ARDS , b) Emphysematous alveolar sac model without ARDS, c) Healthy alveolar sac model with ARDS and d) Emphysematous alveolar sac model with ARDS.	12
2.3	Computational domain mesh for Considered cases.	13
2.4	Influence of alveolar sacs' wall motion on recirculation region and alveolar sacs' mechanics.	17
2.5	Velocity streamlines for healthy and emphysematous alveolar sacs with and without ARDS for TV =500 and 714 mL at $t = 0.5$ s (transition from inhalation to exhalation) and $t = 2$ s (End of breathing cycle).	18
2.6	Velocity changes through healthy alveolar sacs model at TV = 500 mL during inhalation $t = 0.2$ s, inhalation to exhalation $t = 0.5$ s and exhalation $t = 0.8$ s.	19
2.7	Pressure-Volume loop for healthy and emphysematous alveolar sacs at TV = 500 and 714 mL.	20
2.8	Work of breathing for a) healthy alveolar sacs at TV=500 mL, b) Emphysematous alveolar sacs at TV=500 mL and c) Emphysematous alveolar sacs at TV=714 mL.	20
2.9	Influence of emphysema, ARDS and recommended TVs for COPD (TV = 714 mL) and ARDS (TV = 428 mL) on maximum strain, stress and WSS within alveolar sac models.	22
3.1	Methodology for volume-controlled analysis	30
3.2	Methodology for pressure-controlled analysis.	33

3.3	Pressure distribution during inhalation ($t=8$ s) and exhalation ($t=9.2$ s) for Case 1 (morphological and tissue properties of the 50-year-old alveolar sacs), Case 2 (morphological of 50-year-old alveolar sacs and tissue properties of 80-year-old alveolar sacs), Case 3 (morphological of 80-year-old alveolar sacs and tissue properties of 50-year-old alveolar sacs), and Case 4 (morphological and tissue properties of 80-year-old alveolar sacs).	36
3.4	Flowrate waveforms for four breathing cycles and pressure-volume loop for different breathing cycles for (B) Model with morphological and tissue properties of the 50-year-old alveolar sacs (Case1) and (C) Model with morphological and tissue properties of the 80-year-old alveolar sacs (Case 4).	37
3.5	(A_1 - A_3) Pressure-volume plots for considered case studies (case 1 with morphological and tissue properties of the 50-year-old alveolar sacs, case 2 morphological of 50-year-old alveolar sacs and tissue properties of 80-year-old alveolar sacs, Case 3 with morphological of 80-year-old alveolar sacs and tissue properties of 50-year-old alveolar sacs, Case 4 with morphological and tissue properties of 80-year-old alveolar sacs) and contribution of tissue properties and morphological changes in older alveolar sacs compliance decline (B) and WOB decrease (C)	38
3.6	Sensitivity of WOB, strain and compliance to volume-controlled mode parameters (TV, breathing frequency and I/E).	42
4.1	Schematic representation of an airway branch bifurcation in bronchial tree. .	48
4.2	Schematic representation of an airway branch bifurcation in bronchial tree. .	49
4.3	a) Bronchial tree and normal and b) diseased airways radius versus bifurcation generation.	51
4.4	FD of normal and diseased bronchial tree at 20, 50 and 80-year-old case studies.	52

4.5	a) Normal and diseased lung fractal tree at 20, 50 and 80-year-old case studies. b) Changes in lung space-filling in diseased condition compare to normal condition at 20, 50 and 80-year-old. c) Changes in lung space-filling with age compare to lung space-filling at 20-year-old case study	53
4.6	Ratio of changes in mechanical properties of airways from 20 to 50-year-old and 50 to 80-year-old (a_1, b_1, c_1) and mechanical properties of diseased airways at 20, 50 and 80-year-old (a_2, a_3 : Airways resistance, b_2, b_3 : Airways inertance, c_2, c_3 : Airways compliance)	54
5.1	Overview of strain-induced inflammation in this study	60
5.2	Alveolar sac model geometry and B.Cs in the current study. a) Fluid domain b) Cut view of solid domain with shell element.	61
5.3	CA with multiple grids, each grid represents the event and dynamics in the tissue. The graph on the left shows the causal path of the events. Each edge associated with plus (+) sign represent positive feedback to the vertex it is pointing on (activation, release/adding concentration, healing), while the one associated with negative sign (-) carries negative feedback (inhibition, damage).	68
5.4	Strain distribution at inhalation ($t=0.2$ s) and exhalation time ($t=0.5, 0.8$ and 2 s) for TV= 200, 500 and 1000 mL.	75
5.5	Typical distribution of strain. The color bar on the right shows the magnitude correspond to the color plot. (a) Uniform, (b) middle trough, (c) sinusoidal bumps.	76
5.6	Strain level alternation from location 1 to location 3 for different TVs.	77
5.7	Cell population dynamics corresponding to case study I ; numbers of dead epithelial cells on, (a) norm. strain=0.21, (b) norm. strain=0.52, (c) norm. strain=1, and (d) numbers of collagen deposits.	79

5.8	a. Epithelial cells damaged after 300 simulation times, yellow-colored grid denotes the portion of tissue with dead epithelial cells, b. Epithelial cells damaged after 550 simulation times, c. Fibroblasts (white dots) and collagen deposits (dark dots), d. Peak damage to epithelium.	80
5.9	Snapshots of case with norm strain=0.52, (a) Epithelial cells damages after 180 simulation time, yellow-colored grid denotes the portion of tissue with dead epithelial cells, (b) Epithelial cells damages after 900 simulation time. .	81
5.10	Cell population dynamics corresponding to case study <i>II</i> ; Numbers of dead epithelial cells on, (a) norm. strain=0.21, (b) norm. strain=0.52, (c) norm. strain=1, and (d) numbers of collagen deposits.	82
5.11	(a) Epithelial cells damaged after 67 simulation times, yellow-colored grid denotes the portion of tissue with dead epithelial cells, (b) Epithelial cells damaged after 444 simulation times, (c) Fibroblasts (white dots), (d) peak damage to epithelium.	83
5.12	Cell population dynamics corresponding to case study <i>III</i> ;Numbers of dead epithelial cells on, (a) norm. strain=0.21, (b) norm. strain=0.52, (c) norm. strain=1, and (d) Peak damage to epithelium.	84
A.1	(A) 50-year-old alveolar sac model, (B) 80-year-old alveolar sac model. . . .	115
A.2	Mesh size for fluid and solid domain for FSI analysis.	116
A.3	Volume increase from reference volume in 50 and 80-year-old alveolar sacs . .	117

LIST OF TABLES

2.1	Alveolar Sacs' dimensions for current study	13
2.2	Inlet velocity waveform for MV	14
3.1	MV mode effects on 80-year-old alveolar sacs mechanics	40
4.1	Alveolar Sacs' dimensions for current study	50
5.1	Alveolar Sac Model dimensions from the current study compared to morphom- etry reported in the literature	62
5.2	Inlet velocity waveform for MV	63
5.3	Beta Function Parameters	69
5.4	CA parameters for simulation in this paper	70
5.5	Three schemes for CA simulation of cell population dynamics	78
5.6	Qualitative behavior of the alveolar tissue CA model when being subjected to strain at different level	87
A.1	50 and 80-year-old Alveolar sacs dimensions.	111
A.2	Flow rate waveform	112
A.3	Morphological and tissue properties of constructed case studies.	113
A.4	z test for compliance and WOB values for considered case studies and mea- sured confidence intervals for alveolar sacs function in elderly.	114

CHAPTER 1

INTRODUCTION AND LITERATURE REVIEW

The human respiratory system is a series of organs responsible for taking in oxygen and expelling carbon dioxide. The human lung is main organ for gas exchange in human respiratory system and start from trachea to alveoli. Life-threatening respiratory disease like chronic obstructive respiratory disease (COPD), asthma, acute respiratory distress syndrome (ARDS) and aging influence human lung microenvironment and breathing mechanics. COPD is a chronic inflammatory lung disease that causes obstructed airflow from the lungs. Emphysema is one of the main types of COPD and is considered as fourth leading cause of death according to the statistics from the American Lung Association [1]. Gradual loss of air sacs wall surface area for gas exchange in emphysematous alveolar sacs causes difficulty for expelling carbon dioxide during exhalation. Asthma is a common long-term inflammatory disease of the airways of the lungs, where airways narrow and swell and produce extra mucus. This can make breathing difficult and trigger coughing, wheezing and shortness of breath. According World Health Organization (WHO) estimation, about 235 million people currently suffer from asthma and it is the most common chronic disease among children. ARDS is specified as condition where capillary blood and liquid leak into the air sacs. Fluid accumulation in the alveoli and collapse of many alveoli lead to decrease in oxygen level in the blood capillaries. ARDS typically occurs in people who are already critically ill or who have significant injuries. Many people who develop ARDS don't survive. The risk of death increases with age and severity of illness.

In general, human lungs mature around age 20-25 years and will start to lose functionality at approximately 35 years old. Aging causes changes in the human body, which leads to lung

function decline. The diaphragm is the main muscle involved in breathing and moves air in and out of the human lung. This muscle becomes weaker, and its ability to inhale oxygen and exhale carbon dioxide decreases with age. Lung tissues, which keep airways open, also lose their elasticity with age and may cause collapse in airways. Alveoli, small sacs where gas exchange happens, can lose their shape and become baggy. Consequently, breathing generally becomes more difficult over time. Generally, aging induces morphological and tissue property changes in human alveolar sacs.

These changes could lead to lung failure where mechanical ventilation (MV) devices are used to assist or replace spontaneous breathing. Age-related changes pose a higher risk for mortality under MV, and many important decisions have to be made once it is determined that a patient needs MV, including MV mode and parameter settings. Classically, MV modes are divided into pressure and volume controlled modes. Volume-controlled mode has been recently identified as the preferred ventilatory mode. Breathing frequency, Tidal Volume (TV) and I/E (inhalation/exhalation) ratio are the main parameters set for the volume-controlled mode. Although MV saves tens of thousands of lives each year, it can also be harmful and lead to irreversible structural and functional damage in lung, which is known as ventilator-induced lung injury (VILI) [2]. Ventilator settings do impact respiratory system function, and it is therefore important that the settings for MV devices minimize lung injury.

Complex morphology of the bronchial tree causes difficulty in diagnosis and visual interpretation of age-related changes and respiratory disease [3]. In addition, pulmonary function tests are not very sensitive measures of lung disease specifically in early stages of respiratory diseases [4] and we can not repeat the tests to confirm decisive assumption. In addition, specialists can not find proper MV protocols by trial and error to reduce the risk of injuries while implementing MV devices. Hence it would be very useful to develop a mathematical model of these phenomena instead.

Many studies employed computational models to investigate influence of respiratory disease and aging on mechanics of breathing and lung tissue microenvironment at different

scales. 3D printed models of normal and diseased alveolar sacs were employed to visualize fluid flow within alveolar cavities [5]. It was detected that respiratory disease causes radial-like airflows in the alveolar cavities [6]. It was observed that emphysematous alveolar model sustained higher stress level and surface tension compare to normal conditions, which can result in collapse in breathing condition [7]. Computational methods were also used to monitor changes of alveolar recruitment over time for patients with ARDS [8, 9]. Some other studies tried to employ computational techniques to optimize TV settings for patients with emphysema and ARDS. They presented that lower TVs can reduce VILI for patients with ARDS [10] and COPD [11] and limiting repetitive alveolar collapse and expansion introduced as potential parameter to reduce VILI for patients with ARDS [12]. High tidal volume ventilation introduces as main reason for acute lung injury [13, 14]. Strong positive correlation was found between mean stress and cell density in each airway bifurcation [15].

Other studies employed fractal properties of bronchial trees to estimate geometrical complexity, and shapes irregularity in respiratory disease [16, 17]. Some studies employed box counting dimension to estimate fractal dimension (FD) of bronchial tree [16, 18–21]. Uahabi et al used modeling techniques based on variants of the Von Koch curve to estimate fractal dimension of bronchial tree [17]. In addition, equivalent electrical models were employed to estimate changes in normal and diseased airways’ resistance, inertance, and compliance [22, 23].

Many studies have focused on age-related changes and their influences on respiratory system mechanics. It has been shown that while lung static compliance increases with aging, chest wall compliance decreases due to stiffening and there is an increased outward recoil of the thoracic cage [24–28]. Despite the anticipation that an older person sustains ventilation by smaller applied forces on the thoracic cage, an increase in the rigidity of chest wall offsets this advantage [29–31]. It has also been determined that airspace enlargement leads to a decrease in recoil pressure in older alveolar sacs [26, 32, 33].

In addition, computational and multiscale models were used to investigate influence of

inflammatory mediators [34, 35] and variables such as resolution speed, degree and location of stimuli, post coinfections on remodeling [36–40], severity [41] and development [34, 42] of airways disease and aging process [43–47]. Despite all conducted computational and experimental studies on lung inflammation mechanism, there is lack of detail on molecular mechanisms and pathways that contribute to activation of low-grade inflammation and onset of chronic inflammation in lung. There is need for models that link the interactions at the molecular, cellular and tissue-level to provide a systems perspective to the pathology of inflammatory mechanism in lung diseases.

In this dissertation computational models are developed at different level to investigate influence of respiratory disease and aging on mechanics of breathing and structural properties of human lung. Fluid-solid interaction (FSI), fractal geometries and mechanical-electrical analogies are employed to investigate influence of respiratory disease, aging and ventilator protocols on mechanics of breathing at organ level. Results from organ level are transferred to the cellular level to explore influence of ventilator protocols on lung tissue microenvironment and inflammation mechanism in cellular level. Cellular automata (CA) is employed to monitor accompanied changes in cells population dynamics with changes in TV values and strain levels in alveolar sacs region at cellular level. Hence, a comprehensive model for human alveolar sacs which could bridge between cellular and organ level of alveolar sacs is presented and Optimized ventilator protocols specifically for older patients are highlighted to reduce VILI.

Chapter 1 provides background and literature review of influence of respiratory disease and aging on lung tissue microenvironment and breathing condition at different scales and importance of MV protocols to reduce VILI.

Chapter 2 develops three-dimensional (3D) models for healthy and emphysematous alveolar sacs with and without ARDS. Computational fluid dynamic (CFD) analysis and FSI approach are employed to study the influence of alveolar sacs wall motion, TV setting and discussed disease on alveolar sacs mechanics.

Chapter 3 develops 3D models of young and old human alveolar sacs and FSI is employed to investigate the contribution of age-related changes to decline in alveolar sacs function under MV. Ventilator devices setting has been identified as a potential parameter for compromising respiratory function in the elderly. Sensitivity of alveolar sacs mechanics to ventilator setting are illustrated.

Chapter 4, investigates the changes in complexity of normal and diseased bronchial tree with age using FD measures and estimated the respiratory airways structural properties such as resistance, compliance and air inertia within airways using their equivalent electrical models.

Chapter 5 investigates the strain-induced inflammation in pulmonary alveolar tissue under high TV. A realistic 3D organ model for alveolar sacs is built and FSI is employed to evaluate strain distribution in alveolar tissue for different TV values under the MV condition. Interplay between strain magnitude and distribution appears to influence healing capability.

CHAPTER 2

INFLUENCE OF TIDAL-VOLUME SETTING, EMPHYSEMA AND ARDS ON HUMAN ALVEOLAR SACS ¹

¹P. Aghasafari and R. Pidaparti. “Influence of Tidal-Volume Setting, Emphysema and ARDS on Human Alveolar Sacs Mechanics.” Accepted by Computers & Acta Mechanica Sinica (2018): Reprinted here with permission of publisher. *First coauthor.

ABSTRACT

Mechanical ventilation (MV) devices help patients with lung disorders to breath. Improper setting for MV devices would lead to further lung injuries. Therefore, investigating influence of ventilator devices setting on healthy and diseased alveolar sacs mechanics could prevent possible injuries while implementing ventilator devices. For this aim, three-dimensional (3D) models for healthy and emphysematous alveolar sacs with and without acute respiratory distress syndrome (ARDS) were developed and computational fluid dynamic (CFD) analysis and fluid solid interaction (FSI) approach were employed to study the influence of alveolar sacs wall motion, tidal volume (TV) setting and discussed disease on alveolar sacs mechanics. Recirculation region was only monitored in alveolar sacs with rigid wall. Observations demonstrated an increase in compliance during inhaling the air into the emphysematous alveolar sacs. Induced air penetrated deeper into healthy alveolar sacs compare to the emphysematous model and recommended TV for chronic obstructive pulmonary disease (COPD) increased applied strain, stress and wall shear stress (WSS) on emphysematous alveolar sacs walls. In addition, recommended TVs for patients with ARDS decreased strain and stress but did not influence applied WSS significantly. In general, increasing TV raised stress and strain level and led to deeper air penetration into the alveolar sacs. Afterwards, lower TV decreased strain, stress and WSS for patients who could suffer from both ARDS and emphysema. This study would provide invaluable insights about diseased alveolar sacs mechanics and evaluate importance of ventilator devices setting in different disease conditions.

2.1 INTRODUCTION

Alveolar sacs are the main unit for gas exchange in pulmonary system and they would be affected by life-threatening lung disease like asthma, COPD and cystic fibrosis [1, 48]. Emphysema is one of the main types of COPD and is considered as fourth leading cause of death according to the statistics from the American Lung Association. Gradual loss of

air sacs wall surface area for gas exchange in emphysematous alveolar sacs causes difficulty for expelling carbon dioxide during exhalation. Apart from emphysema, ARDS influences alveolar sacs performance. ARDS is specified as condition where capillaries blood and liquid leak into the air sacs. Fluid accumulation in the alveoli and collapse of many alveoli lead to decrease in oxygen level in the blood capillaries and cause serious problem for patients under MV conditions. Lung disease could lead to respiratory failure where lung would not be able to inhale ample oxygen into the pulmonary system and exhale carbon dioxide out and MV devices should be employed to help patients to breathe normally. Improper ventilator devices settings could endanger patients life. TV is one of the most important parameters in MV devices setting. For healthy human, TV is set approximately 500 mL per inspiration [49]. Specialists should consider appropriate TV to ensure adequate ventilation without causing trauma to the lungs. For patients with COPD, it is recommended to set TV about 714 mL and there is strong evidence that limiting TV to range of 428-571 mL may be beneficial in the management of ARDS [50–52].

Flow behavior and alveolar sacs mechanics were evaluated experimentally and computationally. Since alveolar sacs are tiny, most of experimental models scaled up their models and employed dynamic similarities to study airflow pattern in a single alveolar sac. First, Cinkotai [53] made a model for alveolar sacs and observed that despite homogeneous motion, reversibility condition did not occur and recirculation region did not form in alveolar sacs during breathing cycle. Another investigation reflected flow separation and recirculation region in healthy alveolar cavities and detected radial-like airflows in the diseased conditions. Coupling between radial acinar flows and recirculating was experimentally demonstrated in a scaled-up silicone model of a single alveolus [6]. 3D printed models were employed to visualize fluid flow within alveolar sacs [5]. Experimental investigations provided an alternative to clinical test on human to visualize flow pattern in alveolar sacs [54]. It was disclosed that induced air into emphysematous alveoli did not penetrate as deep as healthy alveoli during a single breath, which was related to destruction of alveolar sacs wall and volume increase

in emphysematous condition [55–57]. Extended 3D model from scaled-up rigid-walled alveolar ducts to bifurcations level was built and appearance of a large recirculation zone was captured in alveolus region [58,59]. Alveolar wall motion was detected as main factor which boosts convective mixing between the bronchiole and the alveolar fluid [60,61], Researchers used microfluidic device to mimic alveolar sacs flow pattern and liquid plug formation in pulmonary airways. They observed gradual transition from recirculating to radial streamlines in alveolar flow patterns [62] and concluded that surfactant has protective role against liquid plug formation [63].

In addition, alveolar sacs mechanic was studied numerically. Computational models were considered as tools to help to understand the pathophysiology of healthy and diseased alveolar sacs and design novel medical devices [64,65]. The first numerical model of alveolar ducts presented that rigid wall conditions led to flow separation and appearance of recirculation zone in alveolar sacs [66,67]. CFD analysis techniques were employed to explore flow pattern in alveolar sacs [68]. In addition to CFD analysis, FSI approach was employed to capture realistic physiological breathing conditions in alveolar sacs with moving wall. Due to the computational challenges and costs, FSI has been limited to two-dimensional (2D) alveolar sacs models [69]. Another computational model focused on compression and re-expansion of alveolar sacs during breathing. It was monitored that progress in alveolar collapse increased hysteresis of pressure-volume loop and destroy surface area for gas exchange [70]. Numerical analysis was further used to compare the stress distribution in normal and emphysematous acinar models [71]. It was observed that emphysematous alveolar model sustained higher stress level compare to normal conditions. Human alveolar recruitment in normal and diseased lungs was evaluated and it was observed that diseased alveoli had higher surface tension which resulted in collapse in normal breathing condition [7]. Computational methods were used to monitor changes of alveolar recruitment over time for patients with ARDS [8,9]. Some studies focused on MV-associated damage on diseased lung’s tissue to minimize the injurious effects of MV [72].Computational models presented that lower TVs can reduce

injuries under MV conditions for patients with ARDS [10] and COPD [11]. Limiting repetitive alveolar collapse and expansion introduced as potential parameter to reduce MV's injuries for patients with ARDS [12]. This study focused on healthy and diseased alveolar sacs mechanics under MV condition. Firstly, 3D models for healthy and emphysematous alveolar sacs with and without ARDS were constructed and influence of rigid wall on recirculation formation in the healthy alveolar region was investigated. Applied pressure, strain, stress and WSS in rigid alveolar sacs wall were compared to corresponding values in moving alveolar sacs wall. Secondly, comparison was made between alveolar sacs mechanics in healthy and diseased conditions. Thirdly, influence of recommended TVs for discussed respiratory disease on alveolar sacs was explored and results were compared. Improper ventilator devices settings would endanger patients life and lead to irreversible consequences. Therefore, investigating healthy and diseased alveolar sacs mechanics under MV condition with different ventilator devices settings would provide essential information for respiratory specialists to reduce the risk of adverse events [73].

2.2 METHODS

Numerical analysis was employed to study flow behavior and mechanics of healthy and diseased alveolar sacs in this study. Healthy and emphysematous alveolar models were constructed based on presented dimensions in experimental studies in CAD software and imported into the ANSYS workbench platform. Two case studies were considered to study flow behavior of induced air into healthy alveolar sacs and differences between applied pressure, strain, stress and WSS for the rigid and moving alveolar sacs wall. CFD analysis and FSI were respectively employed for case (1) and case (2) Figure 2.1. For CFD analysis, governing equations for fluid domain were solved and velocity streamlines were plotted to explore influence of the rigid wall on recirculation region. Recorded pressure was applied on the alveolar sacs tissue Fig. 2.1a and applied strain, stress and WSS on alveolar sacs tissue were measured to compare with FSI results.

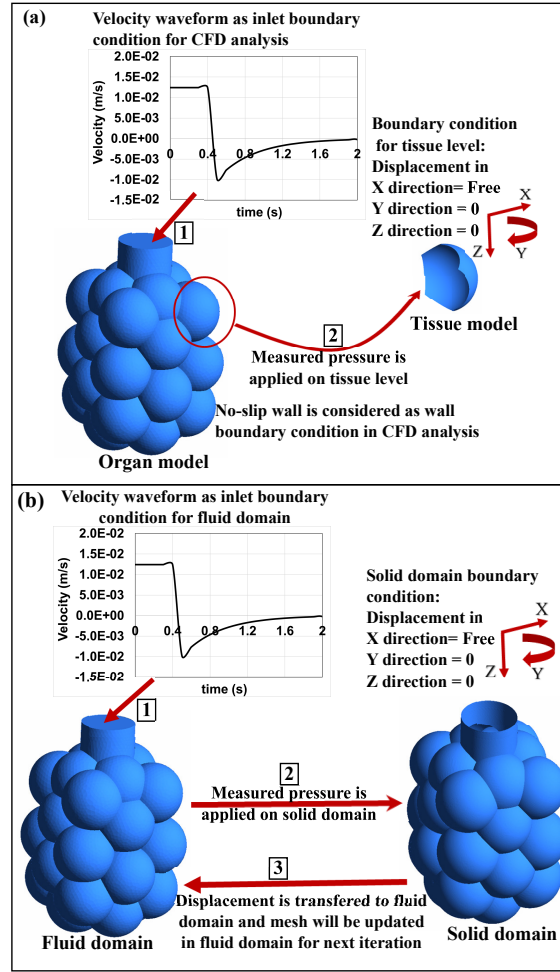


Figure 2.1: a) Case (1) methodology b) Case (2) methodology.

FSI was employed to explore mechanics of emphysematous and healthy alveolar sacs with and without ARDS at recommended TVs under MV condition [74]. Governing equations for structure and fluid were integrated interactively in the time-domain for FSI approach. Fluid pressure was calculated and imported to transient structural solver and corresponding displacement from the structural analysis was returned to the Fluent solver for next iteration. These steps continued until all field equations converged Figure 2.1b [75]. Results from CFD analysis were compared with FSI results for healthy alveolar sacs and influence of emphysema, ARDS and recommended TVs on alveolar sacs mechanics were explored.

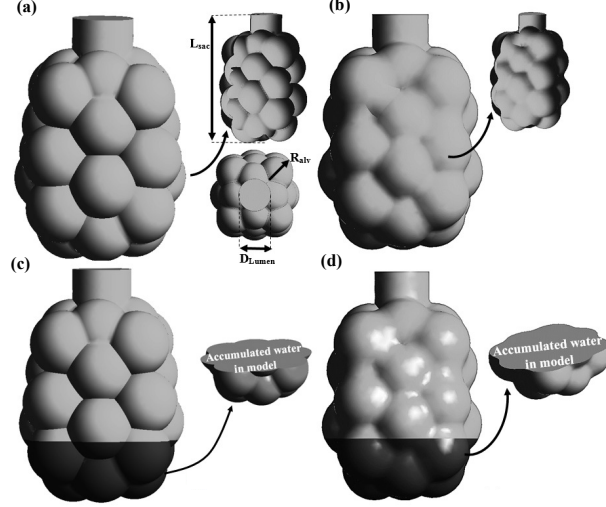


Figure 2.2: Case studies a) Healthy alveolar sac model without ARDS , b) Emphysematous alveolar sac model without ARDS, c) Healthy alveolar sac model with ARDS and d) Emphysematous alveolar sac model with ARDS.

2.2.1 COMPUTATIONAL DOMAIN AND BOUNDARY CONDITIONS

The shapes of alveoli were captured by a range of geometries; including honeycomb [76], polyhedral [5, 77], spheroids, ellipsoids and cylindroids [78]. Variations in shape, size, and location of the alveoli led to significant uneven alveolar ventilation [5]. Also, it was discussed that alveolar geometry was dynamic during breathing cycle [79]. In this study, the 3D model of alveolar sac was built appropriate to realistic dimensions [80–83] and the 3D emphysematous alveolar model was constructed according to surface contact loss for gas exchange and volume increase [57] in SolidWork. To evaluate influence of ARDS on alveolar sacs mechanics, 25% of healthy and emphysematous alveolar sacs models were filled with water. Constructed models and dimensions are presented in Figure 2.2 and Table 2.1.

Table 2.1: Alveolar Sacs' dimensions for current study

Parameters	D_{Lumen}	R_{alv}	L_{sac}	$V_{Healthy}$	$V_{Emphysematous}$
Dimensions	0.2 mm	0.1 mm	0.6 mm	0.09 mm^3	0.11 mm^3

Alveolar sacs were constructed by shell element for the solid domain and inner space within the solid domain was devoted to the fluid domain. Incompressible air and Neo-Hookean hyperelastic material properties were set for FSI analysis. 141488 and 89398 tetrahedrons and triangle mesh types were generated for fluid and solid domains, correspondingly. Generated mesh for fluid and solid domain of healthy and emphysematous alveolar sacs are presented in Figure 2.3.

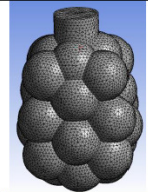
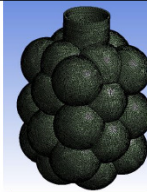
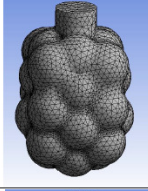
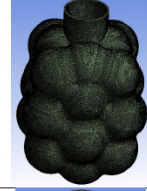
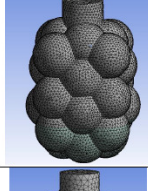

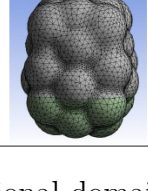
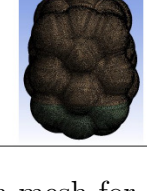
Case studies	Fluid domain mesh	Solid domain mesh
Healthy alveolar sacs without ARDS		
Emphysematous alveolar sacs without ARDS		
Healthy alveolar sacs with ARDS		
Emphysematous alveolar sacs with ARDS		

Figure 2.3: Computational domain mesh for Considered cases.

In addition, solving governing equations for both solid and fluid domains needs appropriate boundary conditions. Existent collagen and elastic fibers in alveolar sacs tissue support alveoli expansion during inhalation process. Then, they would shrink to expel the carbon dioxide during exhalation process. Therefore, displacement in radial direction was set free and longitudinal and rotational displacement were fixed for the solid domain for both case studies Fig. 2.1. Constant and exponentially decreasing velocity waveform for inhalation and exhalation were considered as inlet velocity boundary condition for fluid domain in CFD analysis and FSI approach Table 2.2.

Table 2.2: Inlet velocity waveform for MV

Inhalation/Exhalation	MV
$t \leq \text{Inhalation time } (t_{in})$ $(0 < t_{in} \leq 0.4s)$	$\frac{flowrate}{S*2^{g-1}}$
$t > \text{Exhalation time } (t_{ex})$ $(0.4s < t_{in} \leq 2s)$	$\frac{-flowrate \times \exp(-\frac{t_{in}+t_{ex}}{t_{in}})}{S*2^{g-1}}$

where S and g are the alveolar duct cross section and generation number equal to 23 in this case study. Recommended TVs for healthy and diseased conditions (TV= 428, 500 and 714 mL) were considered in inlet velocity relationship to investigate their effects on fluid flow and healthy and diseased alveolar sacs mechanics under MV condition and interior boundary condition was set for interfaces between induced air and accumulated liquid for ARDS case studies.

2.2.2 GOVERNING EQUATIONS

3D incompressible laminar Navier-Stokes and continuity equations were considered as governing equations for fluid domain [84]. The continuity equation Eq. 2.1 and the Navier-Stokes

equations Eq. 2.2 were solved numerically using a finite-volume method under isothermal conditions in ANSYS fluent solver [85].

$$\nabla \cdot u_f = 0 \quad (2.1)$$

$$\rho_f \left(\frac{\partial u_f}{\partial t} + u_f \cdot \nabla u_f \right) = -\nabla p + \mu \nabla^2 u \quad (2.2)$$

where u_f , ρ_f , p , μ are the fluid velocity field, density equal to $1.225 \left(\frac{kg}{m^3} \right)$ for air and $1000 \left(\frac{kg}{m^3} \right)$ for accumulated water in ARDS case studies, pressure and dynamic viscosity, respectively. Governing equations for the displacement of the alveolar sac walls during inhalation and exhalation were considered as follow:

$$\frac{\partial \sigma_{jk}}{\partial x_k} + \mathbf{F}_j = \rho_s \frac{\partial^2 u_j}{\partial t^2} \sigma_{jk} = \mathbf{E}_{jklm} \epsilon_{lm} \quad (2.3)$$

$$\sigma_{jk} = \mathbf{E}_{jklm} \epsilon_{lm} \quad (2.4)$$

where σ , F , ρ , x , E and ϵ are the stress in each direction, body force, density, displacement, elasticity tensor, and strain in each direction. Hyperelastic Neo-Hookean material properties were adopted to alveolar tissue for FSI simulation. For Compressible Neo-Hookean material, the strain energy density function was given by:

$$W = \frac{G}{2} (\bar{I}_1 - 3) + K_m (J - 1)^2 \quad (2.5)$$

where J is equal to the determinant of deformation gradient and \bar{I}_1 is equal to $J^{-2/3} I_1$ where I_1 is the first invariant of the left Cauchy-Green Tensor. G , K_m and ρ_s are the shear, bulk moduli and alveolar tissue density which set equal to 309 (Pa) , 2.5 (kPa) and $1000 \left(\frac{kg}{m^3} \right)$, respectively [86, 87].

2.2.3 COUPLING ITERATIONS

For each iteration of FSI approach, initially Eqs. 2.1 and 2.2 were solved and applied pressure on the alveolar wall were transferred to the transient structural solver and constitutive

equations for the solid domain Eqs. 2.3 and 2.4 were solved to obtain the alveolar wall displacement. According to the response of the structure, generated mesh was updated by diffusion-based smoothing method in Fluent solver and this continued until all field governing equations converged.

2.2.4 DIFFUSION-BASED SMOOTHING METHOD

Regarding to complexity of motion of alveolar sacs during breathing cycle, moving cell zone were considered in Fluent solver where generated mesh was updated at each time step based on positions of each boundaries which was governed by the diffusion equation Eq. 2.6.

$$\nabla \cdot (\gamma \nabla \vec{u}_m) = 0 \quad (2.6)$$

where \vec{u}_m is the mesh displacement velocity and γ is diffusion coefficient which used to control effect of the boundary motion on the interior mesh motion Eq. 2.7 .

$$\gamma = \frac{1}{d^\theta} \quad (2.7)$$

where d is a normalized boundary distance. Diffusion parameter (θ) was set to two, to preserve larger regions of the mesh near the moving boundary, and let regions from the moving boundary to absorb more of the motion.

2.3 RESULTS

CFD analysis and FSI results for healthy alveolar sacs were compared to investigate influence of wall motion on alveolar sacs function. Applied pressure on rigid and moving alveolar sacs wall and corresponding strain, stress and WSS values were compared. In continue, FSI approach was employed to study influence of disease like emphysema and ARDS and recommended TVs for discussed disease on alveolar sacs mechanics under MV conditions. Velocity streamlines and fluid velocity were compared for healthy and diseased alveolar sacs

and impact of recommended TVs on fluid flow was evaluated. In addition, influence of disease conditions and recommended TVs are contrasted qualitatively.

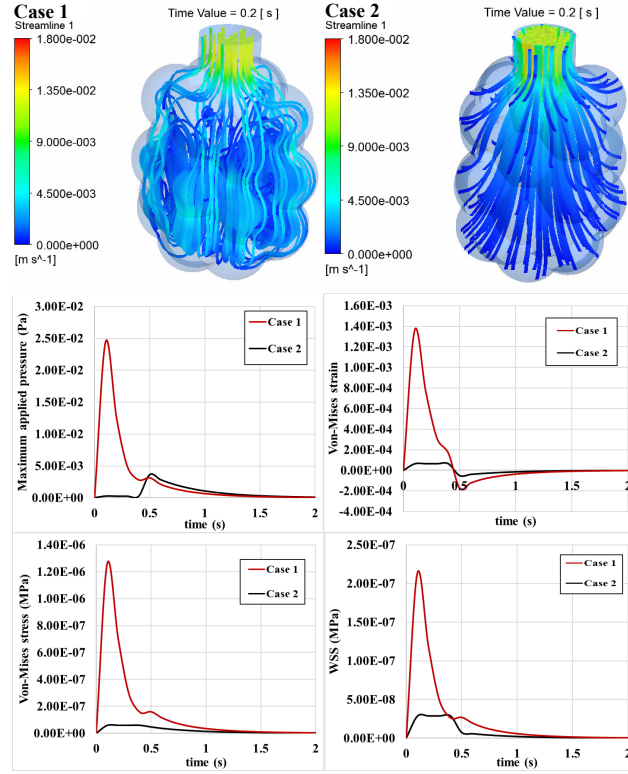


Figure 2.4: Influence of alveolar sacs' wall motion on recirculation region and alveolar sacs' mechanics.

2.3.1 RECIRCULATION REGION AND FLOW VELOCITY

Since acinar airflow has significant role in aerosol deposition, many studies focused on existing flow pattern in alveolar region. They presented that despite low-Reynolds-number flows, irreversibility exists in the acinus [54] and recirculation occurs in the proximal alveoli only during the transition between inspiration and expiration [82]. Streamlines show the direction which fluid elements travel at any point in breathing cycle and provide insights about particles penetration into the alveolar region and recirculation region formation. According to previous studies, alveolar sacs wall motion is main factor for recirculation region formation [60,61,66,67] and wall destruction and increase in alveolar volume when several alveoli merge into a single sac were introduced as main factors which led to less air penetration into

diseased alveoli compare to healthy alveoli [55, 56]. Hence, streamlines are plotted for the fluid domain in CFD analysis and FSI approach and recirculation region was monitored in alveolar sacs with rigid wall while no recirculation region was detected in alveolar sacs with moving wall Fig .2.4. Streamlines were also plotted for healthy and emphysematous alveolar sacs at transition time between inspiration and expiration for single breathing cycle and it was presented that induced air into emphysematous model would not penetrate into the alveoli as deep as healthy model Fig. 2.5 and increasing TV to the recommended value for patients with COPD could push more air into the alveoli for gas exchange. In addition, it was illustrated that the recirculation zone did not form even in transition time from inhalation to exhalation. Furthermore, ARDS considerably affected airflow in both healthy and emphysematous alveolar models during the exhalation time. Fluid flow had more complex pattern in case studies with ARDS and increasing TV resonated this condition for both models.

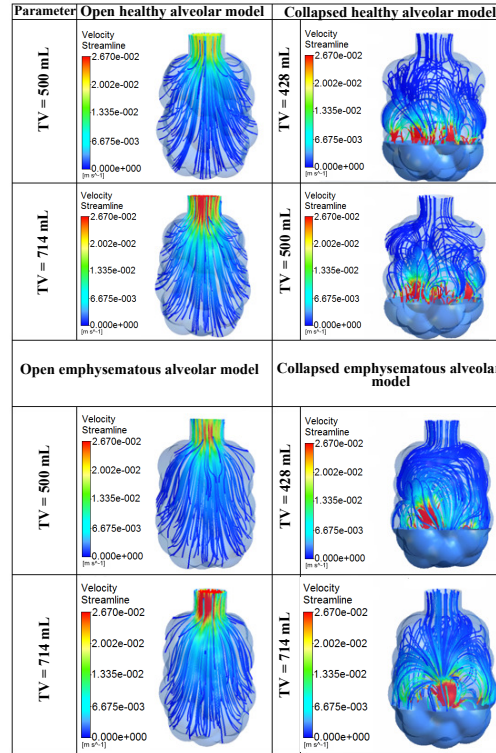


Figure 2.5: Velocity streamlines for healthy and emphysematous alveolar sacs with and without ARDS for TV = 500 and 714 mL at $t = 0.5$ s (transition from inhalation to exhalation) and $t = 2$ s (End of breathing cycle).

In addition, fluid velocity within healthy alveolar sacs versus time plots demonstrated that the velocity increased from alveolar ducts (plane1) to alveolar sacs entry (plane2) where fluid velocity reached its highest value within alveolar sacs. Then it decreased toward the bottom of the model and followed this trend for entire breathing cycle Fig. 2.6. These results are in good agreement with previous studies [58]

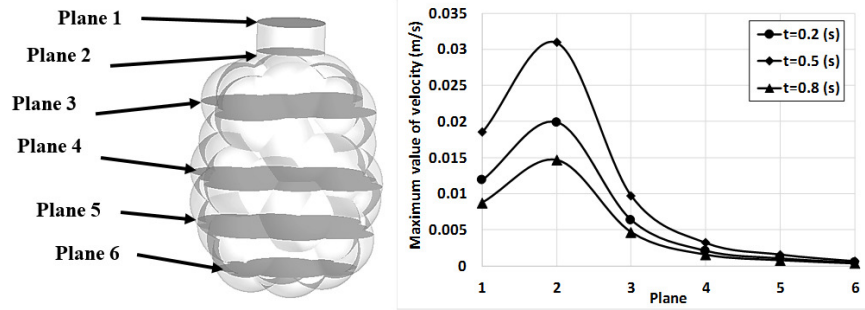


Figure 2.6: Velocity changes through healthy alveolar sacs model at TV = 500 mL during inhalation $t = 0.2$ s, inhalation to exhalation $t = 0.5$ s and exhalation $t = 0.8$ s.

2.3.2 LUNG COMPLIANCE

Lung compliance measures lungs ability to expand and is proportionate to volume change per unit pressure change [88]. Compliance could change in various disease conditions. For instance, emphysema increases lung compliance and small pressure difference is necessary to maintain a large volume in emphysematous alveolar sacs [88]. Pressure-volume for healthy and emphysematous alveolar models were plotted and it was illustrated that emphysematous alveolar models had higher compliance during inhalation whereas the healthy alveolar model had higher compliance in continue during exhalation time Fig. 2.7 which caused problem to exhale carbon dioxide out for emphysematous case studies. Also, it was observed that increasing TV increased applied pressure on the alveolar wall at same volume changes specifically in emphysematous case studies.

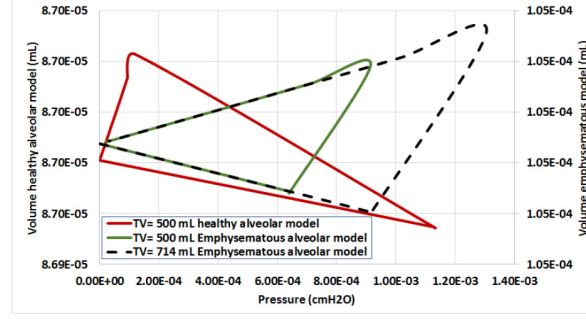


Figure 2.7: Pressure-Volume loop for healthy and emphysematous alveolar sacs at $TV = 500$ and 714 mL.

2.3.3 WORK OF BREATHING

WOB is the required energy to inhale air into the model and exhale carbon dioxide. Pressure-volume loops can provide information about changes in the patient's lung compliance, air leaks and work of breathing. The area under of the pressure-volume loop presents the WOB. Accordingly, the area under pressure-volume loop for healthy and emphysematous alveolar sacs for TV equal to 500 and 714 mL were calculated and it was presented that required energy for breathing in emphysematous state approximately increased by 10 times and increasing TV increased WOB for emphysematous alveolar sacs Fig. 2.8.

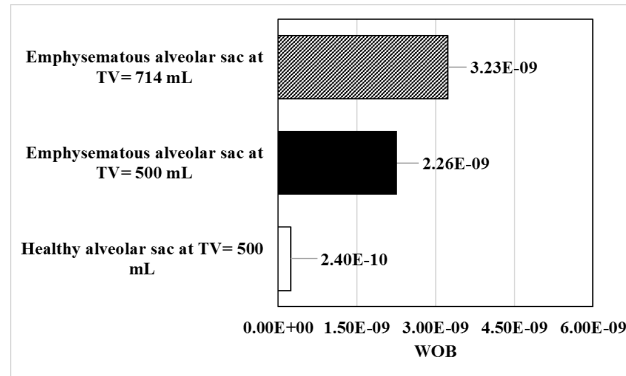


Figure 2.8: Work of breathing for a) healthy alveolar sacs at $TV=500$ mL, b) Emphysematous alveolar sacs at $TV=500$ mL and c) Emphysematous alveolar sacs at $TV=714$ mL.

2.3.4 STRAIN AND STRESS LEVEL

Maximum von-Mises strain, stress and WSS were compared for all case studies to investigate influence of emphysema, ARDS and recommended TVs on alveolar sacs mechanics Fig. 2.9. Upper triangle of each cell in the figure 2.9 illustrates comparison between considered case study and healthy alveolar sacs with TV equal to 500 mL, and lower triangle represents comparison between considered case studies and same condition at TV equal to 500 mL. Alveolar sacs generally had smaller strain values in the emphysematous condition and ARDS led to higher strain values within alveolar sacs models compared to healthy alveolar sacs. Recommended TVs for COPD increased expansion of the model compared to emphysematous alveolar sacs with normal TV (TV=500 mL) and recommended TVs for ARDS decreased strain level compared to case studies with same condition at TV equal to 500 mL. In addition, TV equal to 714 mL increased emphysematous alveolar sacs with ARDS expansion at upper and lower part of the model compare to TV amount to 500 mL.

Von-Mises stress was evaluated and observed that the emphysematous model tolerated higher stress level compare to the healthy alveolar sacs. These results were in good agreement with Ryk study [71]. Although, recommended TV for emphysematous alveolar sacs models increased strain within the model, it also increased maximum von-Mises stress level. Likewise, decreasing TVs for ARDS case studies increased maximum applied stress on alveolar sacs wall Fig. 2.9. For both healthy and emphysematous alveolar sacs with ARDS, reducing TV to 428 mL reduced maximum applied stress on the models wall significantly.

WSS is related to existing friction between the induced air and the alveolar wall. WSS magnitude depends on how fast the fluid velocity rises when flowing from the alveolar wall toward the center of the alveolar. Recommended TVs for COPD and ARDS delivered higher WSS compare to 500 mL and recommended TV for ARDS could reduce WSS for emphysematous alveolar sacs with ARDS but could not reduce applied WSS on the models wall Fig. 2.9.

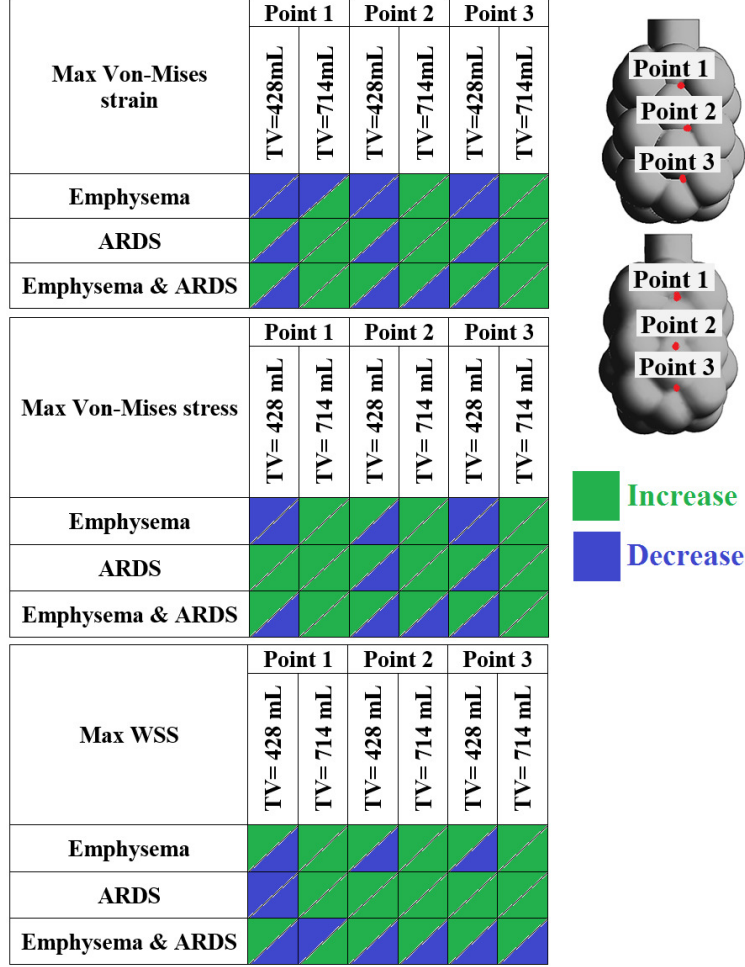


Figure 2.9: Influence of emphysema, ARDS and recommended TVs for COPD (TV = 714 mL) and ARDS (TV = 428 mL) on maximum strain, stress and WSS within alveolar sac models.

2.4 CONCLUSION

The developed geometric acinar model accompanied with CFD and FSI techniques, are served as investigative tools in the study of the influence of TV setting and diseases like emphysema and ARDS on alveolar mechanics under MV condition. Recirculation region was not observed in the FSI approach for both healthy and emphysematous alveolar models and alveolar sacs wall motion was introduced as the main reason for observed recirculation

region in healthy alveolar sacs. Strain, stress and WSS were recorded higher in the case study whose applied pressure was measured from rigid alveolar sacs wall in comparison to measured values from the FSI approach. Alveolar sacs mechanics was substantially affected by pulmonary disease. Emphysema led to less air penetration into the acinar region. Lung compliance increased in the emphysematous condition where alveolar sacs tended to distend easily but empties slowly. Emphysema increased the required energy for breathing cycle and higher TVs value resulted in higher WOB. On the contrary to stress, strain values diminished in the emphysematous state which could instigate problem for breathing under MV condition. Comparison between results for different TVs for both healthy and emphysematous alveolar models displayed that recommended TVs for patients with COPD increased strain and increased applied stress and WSS compare to emphysematous model with TV equal to 500 mL. Decreasing TV for ARDS would decrease applied strain and stress on the model but increased applied WSS, specifically towards the bottom part of the model. It was demonstrated that higher TVs for emphysematous alveolar sacs with ARDS decreased maximum WSS while it increased applied stress and strain on the model. In conclusion, this study would provide invaluable insights for specialists about alveolar sacs mechanics under influence of respiratory disease to set appropriate TVs for patients under MV conditions.

CHAPTER 3

AGING EFFECTS ON ALVEOLAR SACS UNDER MECHANICAL VENTILATION ¹

¹P. Aghasafari, R. L. Heise, A. Reynolds and R. Pidaparti. “Aging Effects on Alveolar Sacs under Mechanical Ventilation.” Accepted by The Journals of Gerontology: Series A (2018): Reprinted here with permission of publisher. *First coauthor.

ABSTRACT

Alveolar sacs are primarily responsible for gas exchange in the human respiratory system and lose their functionality with aging. Three-dimensional (3D) models of young and old human alveolar sacs were constructed and fluid-solid interaction (FSI) was employed to investigate the contribution of age-related changes to decline in alveolar sacs function under mechanical ventilation (MV). Simulations results illustrated that compliance and pressure reduced in the alveolar sacs of the elderly, and they have to work harder to breathe. Morphological changes were found to be mainly responsible for the decline in alveolar sacs function. Influence of individual differences on the alveolar sacs function was negligible and 95% confidence intervals for compliance and work of breathing (WOB) using measures from different individuals also support this finding. Moreover, higher mortality risk was recorded for elderly who undergo MV. Specifically, ventilator devices setting has been identified as a potential parameter for compromising respiratory function in the elderly. Volume-controlled ventilation applied less pressure, whereas, pressure-controlled ventilation resulted in higher compliance in the alveolar sacs and decreased WOB. Sensitivity of alveolar sacs to ventilator setting under the volume-controlled mode illustrated that increasing breathing frequency and decreasing the ratio of inhalation to exhalation times (I/E) and tidal volume (TV) caused an increase in alveolar sacs expansion and compliance in older patients. Results from this study can help clinicians to develop individualized and effective ventilator protocols and improve respiratory function in the elderly.

3.1 INTRODUCTION

Human lungs mature around age 20-25 years and will start to lose functionality after approximately 35 years [31]. Aging causes changes in the human body, which leads to lung function decline [89]. The diaphragm is the main muscle involved in breathing and moves air in and out of the human lung. This muscle becomes weaker, and its ability to inhale oxygen and

exhale carbon dioxide decreases with age [90]. Lung tissues, which keep airways open, also lose their elasticity with age and may cause collapse in airways [86, 87, 91]. Alveoli, small sacs where gas exchange happens, can lose their shape and become baggy [91]. Consequently, breathing generally becomes more difficult over time.

Generally, aging induces morphological and tissue property changes in human alveolar sacs. These changes influence alveolar sacs mechanics and gas exchange [27, 31, 92–94]. Quirk et al [91], used MRI with hyperpolarized ^3He and detected age-dependent morphological changes in the acinar region. They monitored decline in alveolar depth, alveolar density, surface area, and surface to volume ratio and increases in lumen radius, volume, mean chord length, and acinar airway radius. Moreover, an increase in alveolar wall thickness has been observed in older subjects in previous experimental studies [87, 91, 95, 96]. In addition to the structural changes, aging imposes material properties changes on alveolar sacs [86, 87, 91] and this leads to an increase in tissue bulk and shear modulus [86, 87, 94].

In the case of lung failure, patients often need Mechanical Ventilation (MV) devices to assist them in inhaling oxygen to the respiratory system. Age-related changes pose a higher risk for mortality under MV, and many important decisions have to be made once it is determined that a patient needs MV, including MV mode and parameter settings. Classically, MV modes are divided into pressure and volume controlled modes. Volume-controlled mode has been recently identified as the preferred ventilatory mode [97]. Breathing frequency, Tidal Volume (TV) and I/E (inhalation/exhalation) ratio are the main parameters set for the volume-controlled mode. Ventilator settings do impact respiratory system function, and it is therefore important that the settings for MV devices minimize lung injury.

Many studies have focused on age-related changes and their influences on respiratory system mechanics. It has been shown that while lung static compliance increases with aging, chest wall compliance decreases due to stiffening and there is an increased outward recoil of the thoracic cage [24–28]. In addition to compliance, WOB has been identified as a major parameter that would be affected by age-related changes. Although, it is anticipated that an

older person sustains ventilation by smaller applied forces on the thoracic cage accompanied with a corresponding reduction in the elastic WOB, an increase in the rigidity of chest wall offsets this advantage [29–31]. It has also been determined that airspace enlargement leads to a decrease in recoil pressure in older alveolar sacs [26, 32, 33]. Age-related changes have been accepted as main factors that lead to a decline in lung function, but it is unclear if these changes are due to structural changes or tissue property changes in alveolar sacs. Alveolar mechanics have been investigated under normal conditions while their functionality under MV conditions has only recently been studied. It is important that age-related changes in alveolar sacs mechanics under MV be investigated as there is a possibility that the MV device settings would also affect alveolar sacs mechanics.

In this study, the contributions of morphological and tissue property changes as well as differences in ventilator device settings were investigated to assess their impact on decline in alveolar sacs function. This paper is organized into four sections. In the first section, the impact of age-related morphological and tissue property changes on alveolar sacs function is investigated, and the results are discussed. In the second section, influence of individual difference on alveolar sacs function is explored and confidence intervals for measured values for different case studies at older ages are presented that reflect the applicability of results from this study to the elderly. In the third section, normalized results for volume-controlled and pressure-controlled MV modes are compared to investigate the effect of MV mode on alveolar sacs mechanics in the elderly. The fourth section is devoted to sensitivity analysis of alveolar sacs mechanics to ventilator device settings. Influence of TV, breathing frequency and I/E ratio in volume-controlled mode on the alveolar sacs function in the elderly is evaluated. Efforts were made to identify the best settings for MV devices to improve breathing conditions specifically for older patients.

3.2 FSI APPROACH

Quirk et al [91] performed MRI with hyperpolarized ^3He gas on 24 healthy nonsmokers ages 19 to 71 years. They presented a linear correlation between adults acinar morphometric parameters and age with 95% confidence intervals (Table A.1). As discussed in their study, alveolar depth decreases and lumen diameter and mean chord length increase in older cases [86, 91]. Moreover, previous experimental studies presented that older alveolar sacs have thicker walls compared to younger models [87, 95]. To investigate changes in alveolar sacs function with age, 3D models of 50 (young) and 80-year-old (old) human alveolar sacs were built in CAD software based on anatomical dimensions presented for alveolar sacs in previous experimental studies [86, 87, 91, 95]. Additional details regarding the constructed models for 50 and 80-year-old alveolar sacs in this study are presented in Figure A.1 and Table A.1.

Next, constructed geometries for 50 and 80-year-old alveolar sacs were imported to ANSYS transient structural and Fluent solver. Four different case studies were considered to explore the influence of morphological and tissue property changes on alveolar sacs mechanics. Case 1 included morphological and tissue properties of the 50-year-old model. Case 2 had the geometry of the 50-year-old and the tissue properties of 80-year-old alveolar sacs. Case 3 contained the structural properties of 80-year-old alveolar sacs and tissue properties of the 50-year-old alveolar sacs, while case 4 had the morphological and tissue properties of 80-year-old alveolar sacs. FSI was employed for all case studies to investigate the interaction of alveolar sacs structure and induced air into the model [83]. Based on the number of iterations required for convergence, the time step was set to 0.1 (s). All geometries were meshed using tetrahedral elements, and dynamic mesh was activated for the fluid domain. Mesh convergence was performed, and a 2 million mesh size was set for the fluid domain, and a 1.8 million mesh size was fixed for the solid domain. Figure A.2 includes a magnified FE mesh and mesh elements for the 50 and 80-year-old alveolar sacs.

Boundary conditions were set for young and elderly patients according to the MV mode.

Alveoli contain some collagen and elastic fibers, which allow the alveoli to stretch as they are filled with air during inhalation. Then they spring back during exhalation to expel the carbon dioxide-rich air. Since alveolar sacs were considered separate from the whole lung in the simulations, free displacement in radial direction and fixed longitudinal and rotational displacement were established as boundary conditions for the solid domain as shown in Figures 3.1 and 3.2.

3.3 VOLUME-CONTROLLED VENTILATION MODE

For the volume-controlled MV mode, flowrate waveform during MV was defined as the boundary condition for the fluid domain in the form of constant and exponentially decreasing flowrate profiles for inhalation and exhalation and imported as UDF files. Total breathing time (t_t) for each cycle was determined from breathing frequency (t_t is equal to $\frac{60}{frequency}$) and the ratio of inspiratory time (t_{in}) to expiratory time (t_{ex}) was set to 1:3 [98]. Flowrate is equal to the volume change per unit time and is defined according to alveolar sacs volume change from collapsed to expanded condition during inhalation ($\frac{Volumechanges}{t_{in}}$). Since the area under the flowrate waveform is equal to TV [98], TV was set to $8.3e^{-5}$ mL (volume changes of 50-year-old alveolar sacs from collapsed to expanded condition). The integral of exponential exhalation flowrate waveform was set to TV [31, 98, 99] and exponential function was correspondingly estimated. Flowrate waveform was generated for four breathing cycles. Since the 3D geometrical model was constructed based on expanded dimensions, flowrate was assumed to be equal to zero during inhalation time in the first breathing cycle. The air filled the alveolar sacs model during the first inhalation time then the breathing followed the whole breathing flowrate waveform for the remaining breathing cycles. The generated flowrate waveform function and the four breathing cycle patterns are presented in Table A.2.

Two-way FSI was conducted for the volume-controlled mode where governing equations for fluid and solid domain were solved iteratively as shown in Figure 3.1. The velocity field within the alveolar region was numerically calculated by solving 3D incompressible laminar

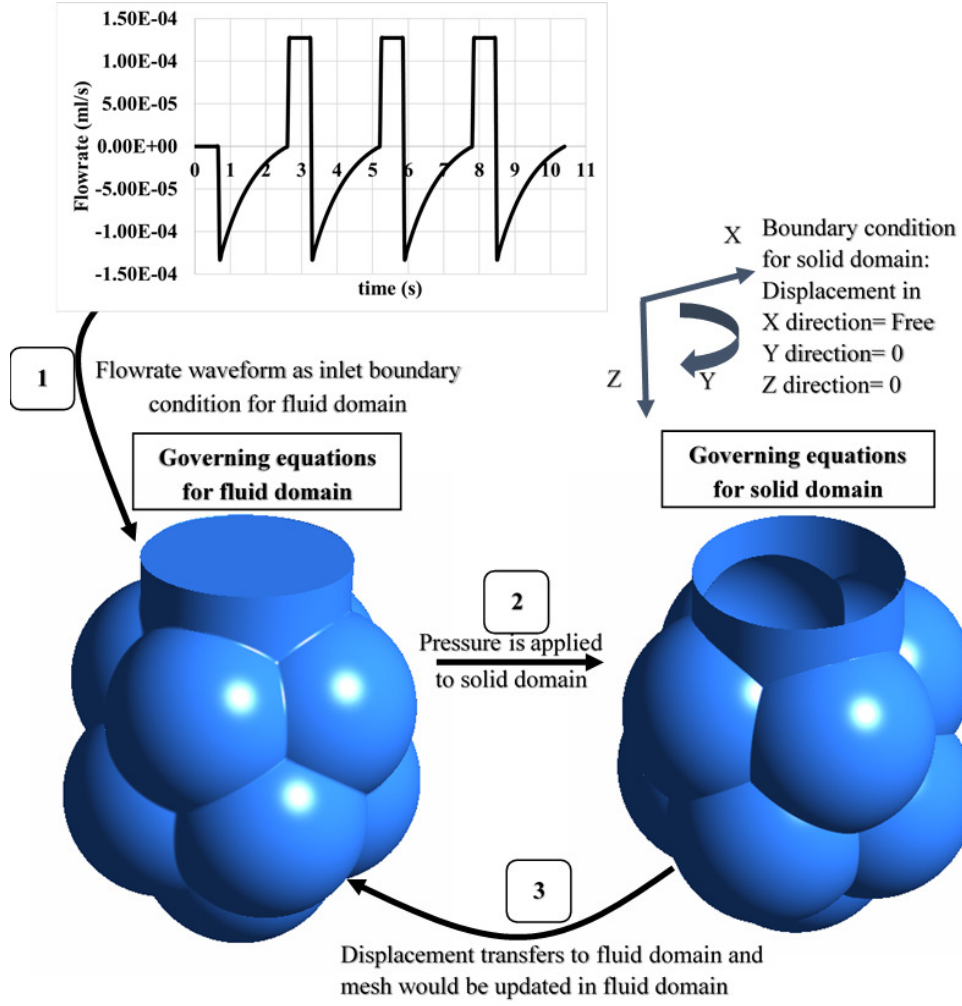


Figure 3.1: Methodology for volume-controlled analysis

Navier-Stokes and continuity equations in a 3D mesh domain with a control volume approximation [84]. The continuity equation Eq. 3.1 and the Navier-Stokes equations Eq. 3.2 were solved numerically on a moving grid using a commercial finite-volume based program with fully implicit time marching techniques under isothermal conditions in ANSYS fluent solver [100].

$$\nabla \cdot u = 0 \quad (3.1)$$

$$\rho_f \left(\frac{\partial u}{\partial t} + u \cdot \nabla \cdot u \right) = -\nabla p + \mu \nabla^2 u \quad (3.2)$$

where u , ρ_f , p , μ are the velocity field, air density, pressure and dynamic viscosity, respectively. Calculated pressure from the fluid domain was transferred to the solid domain, and governing equations for the solid domain were solved corresponding to the output of the fluid domain.

The time-dependent structural equations were used as governing equations for the movement of the alveolar sac solid domain during inhalation and exhalation as shown in Eqs. (3.3,3.4):

$$\frac{\partial \sigma_{ij}}{\partial x_j} + \mathbf{F}_i = \rho_s \frac{\partial^2 x_i}{\partial t^2} \quad (3.3)$$

$$\sigma_{ij} = \mathbf{E}_{ijmn} \epsilon_{mn} \quad (3.4)$$

where σ , F , ρ , x , E and ϵ are the stress in each direction, body force, density, displacement, elasticity tensor, and strain in each direction. Hyperelastic Neo-Hookean material parameters were adopted for the alveolar wall tissue materials for the FSI simulation. For Compressible Neo-Hookean material, Eq. 3.5 gives the strain energy density function:

$$W = \frac{G}{2} (\bar{I}_1 - 3) + K_m (J - 1)^2 \quad (3.5)$$

where J is equal to the determinant of deformation gradient, $\bar{I}_1 = J^{-\frac{2}{3}} I_1$ is the first invariant of the isochoric part of right Cauchy-Green deformation tensor, and I_1 is the first invariant of the right Cauchy-Green deformation tensor. G and K_m are the shear and bulk modulus, respectively. Both shear and bulk modulus increased with age. An increase in elastin content with aging has been shown to lead to an increase in alveolar diameter and tissue forces [86, 87]. The shear and bulk modulus values considered for the 50 and 80-year-old alveolar sacs tissues are presented in Table A.1. The displacement response from the solid domain was imported to fluid domain. These iterations were continued until convergence was reached for all data transferred and field equations [101] as shown in Figure 3.1.

3.4 PRESSURE-CONTROLLED VENTILATION MODE

For the pressure-controlled mode, one-way FSI was employed as shown in Figure 3.2. For this case, instead of flowrate waveform for the fluid domain, pressure was applied on the solid domain, and governing equations for the solid domain were solved until the convergence criteria were reached [102]. As shown in Table 3.1, pressure equal to 10 cmH_2O was applied to the alveolar sacs wall and inhalation to exhalation time ratio was set equal to 1:2 [98]. The calculated displacements from the solid domain were then transferred to the fluid domain, and governing equations for the fluid were solved. Then, the structure displacement was calculated for the next time step. The solution is considered to be complete when the maximum number of time steps is reached. Next, the normalized results for the volume-controlled and pressure-controlled modes were compared to explore the influence of ventilatory mode change on breathing condition in older alveolar sacs.

3.5 STATISTICAL ANALYSIS

Alveolar sacs wall thickness, and bulk and shear modulus for 80-year-old were varied statistically to investigate influence of individual difference on alveolar sacs function. Dimensions of constructed 3D models are presented in Table A.3. FSI analysis was conducted for all case studies and results for alveolar sacs compliance and WOB were compared. Significance level of $p < 0.05$ was considered and two-tailed z test was employed to test the null hypothesis of no significant difference relevant to individual differences. In addition, percentage of change and the confidence interval, that reflects the applicability of presented results for the given samples in this study, were calculated to be able to generalize conclusions from this study to the elderly.

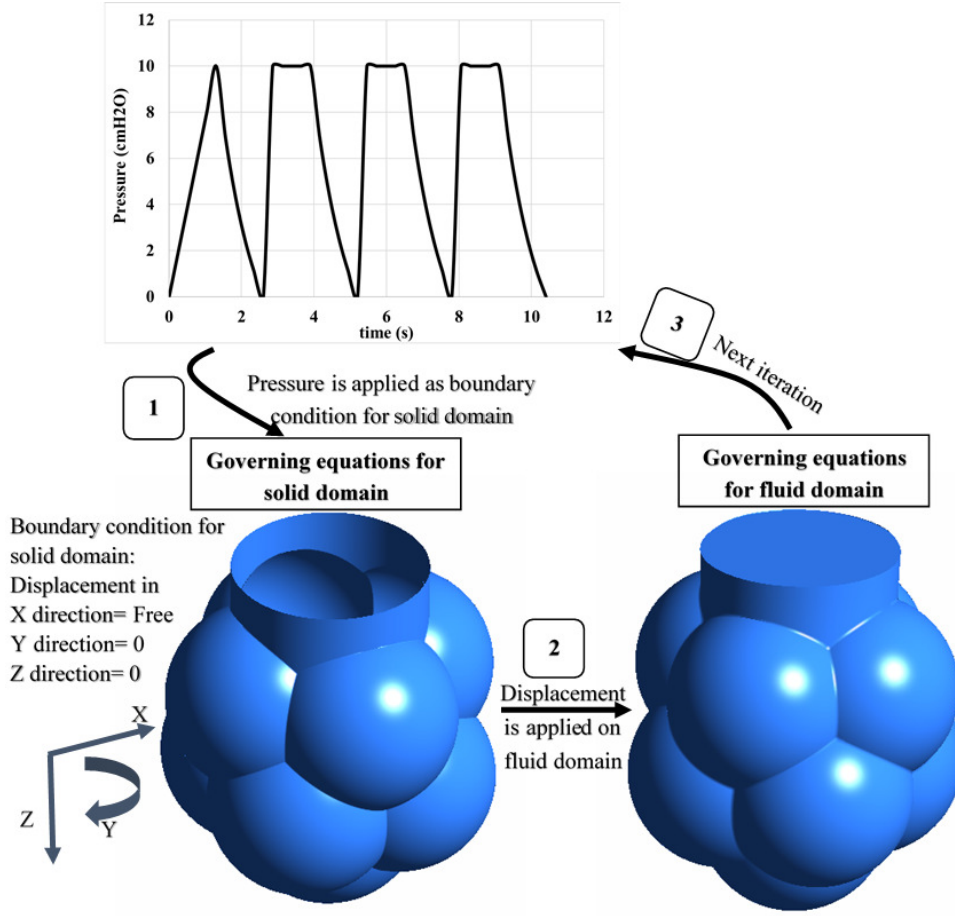


Figure 3.2: Methodology for pressure-controlled analysis.

3.6 SENSITIVITY ANALYSIS

The volume-controlled ventilation mode allows for an easier approach to monitoring respiratory mechanics. Therefore, the volume-controlled mode has been recently identified as the preferred ventilation mode [97]. Subsequently, the sensitivity of alveolar sacs functionality to parameter settings in the volume-controlled mode (breathing frequency, TV and ratio of inhalation to exhalation time) were investigated. In general, higher breathing frequency and lower TV are recommended for older patients [99]. Consistent with this practice, considered values of these parameters in this study were increased and decreased by 10%, and FSI was

conducted for all case studies. The results were compared to evaluate the influence of each parameter on older alveolar sacs mechanics.

3.7 RESULTS

3.7.1 APPLIED PRESSURE

Previous studies have indicated that elastic recoil pressure of the lung decreases with age. Janssens et al. [26] identified a rate of 2 cmH_2O and Niewoehner et al. [33] reported a rate of 1.2 cmH_2O per decade for 25 and 60-year-old lungs. In addition, Subramaniam et al. [94] suggested that alveoli expansion begins when pressure reaches 25 cmH_2O . They expanded the alveolar sac model by applying pressure to internal surfaces of the alveoli isotropically. Although applied pressure on alveolar sacs wall increases during inhalation, it will decrease during exhalation. Accordingly, applied pressure in a volume-controlled mode in this study was recorded as 10 cmH_2O for the 50-year-old and 2 cmH_2O for the 80-year-old cases during inhalation while this value was decreased while exhaling air. Subramaniam et al [94], presented volume increase from reference volume. Results for volume changes from reference volume for the same amount of applied pressure on the alveolar sacs wall were compared with results from Subramaniam et al study [94]. Lower pressure values resulted in lower volume changes for the same amount of applied pressure on the alveolar sacs wall. The volume changed about 0.06% and 0.2% at pressure equal to 2 cmH_2O for the 50 and 80-year-old alveolar sacs models considered in this study, while Subramaniam et al reported volume changes of 3.4% and 6.8% at pressure equal to 2 cmH_2O for 20 and 60-year-old alveolar sacs [94]. One reason for the discrepancy may be due to the fact that lower pressure was applied on the alveolar sacs wall in this study. In addition, larger volume changes at the same pressure values are recorded in older alveolar sacs model compared to younger alveolar sacs models (Figure A.1).

FSI was conducted for 50 and 80-year-old alveolar sacs for the volume-controlled mode

and post-processed results were compared to evaluate contribution of age-related tissue properties and morphological changes to a decline in alveolar sacs function. In general, age-related changes decreased applied pressure on the alveolar sacs [94]. Figure 3.3 illustrates the pressure distribution in four different case studies of 50 and 80-year-old alveolar sacs models. As can be seen, during inhalation at t equal to 8 (s), a high amount of pressure was applied on the duct area by inhaling air into the model. On the other hand, during exhalation at t equal to 9.2 (s), pressure was highly distributed in the sacs region and is almost equal to zero in the duct region. Also, significant pressure values were noted at the bottom of the 50-year-old alveolar sacs model during inhalation. Finally, age-related changes decreased applied pressure on older alveolar sacs.

3.7.2 ALVEOLAR SACS DYNAMIC COMPLIANCE WITH AGING

Alveolar sacs dynamic compliance is a measure of alveolar sacs ability to stretch and is equal to the volume change per unit pressure change. The slop of pressure-volume graph for specific pressure change illustrates the dynamic compliance. Pressure-volume loops were plotted for different breathing cycles for 50 (Figure 3.4B) and 80-year-old alveolar sacs (Figure 3.4C) under MV. It was hypothesized that cyclic breathing patterns would affect the pressure-volume loop. Figure 3.4 illustrates that compliance decreased in each breathing cycle and hardened the alveolar sacs expansion, and as a result, more energy would be required to inhale air into the model. Required energy for breathing, which is equal to the enclosed pressure-volume loop area, increased by 40% for the 50-year-old model and 30% for the 80-year-old model.

Pressure-volume loop testing was also employed to investigate the influence of aging on compliance. It was hypothesized that aging would decrease alveolar sacs compliance which means older alveolar sacs would have less tendency to expand compared to younger sacs. Hence, different case studies were considered to investigate the contributions of tissue properties and morphological changes on compliance decline in older alveolar sacs. Morphological

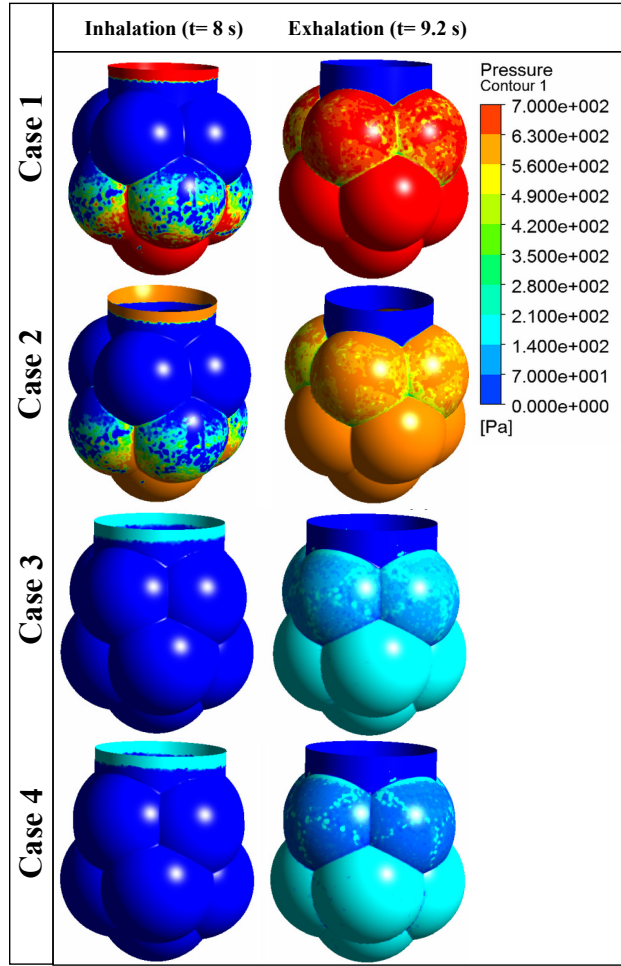


Figure 3.3: Pressure distribution during inhalation ($t=8$ s) and exhalation ($t=9.2$ s) for Case 1 (morphological and tissue properties of the 50-year-old alveolar sacs), Case 2 (morphological of 50-year-old alveolar sacs and tissue properties of 80-year-old alveolar sacs), Case 3 (morphological of 80-year-old alveolar sacs and tissue properties of 50-year-old alveolar sacs), and Case 4 (morphological and tissue properties of 80-year-old alveolar sacs).

changes in older alveolar sacs emerged as the main factor for compliance decline in older sacs (Figure 3.5). Compliance decreased by almost 40% for the 80-year-old as compared to the 50-year-old alveolar sacs as shown in (Figure 3.5B).

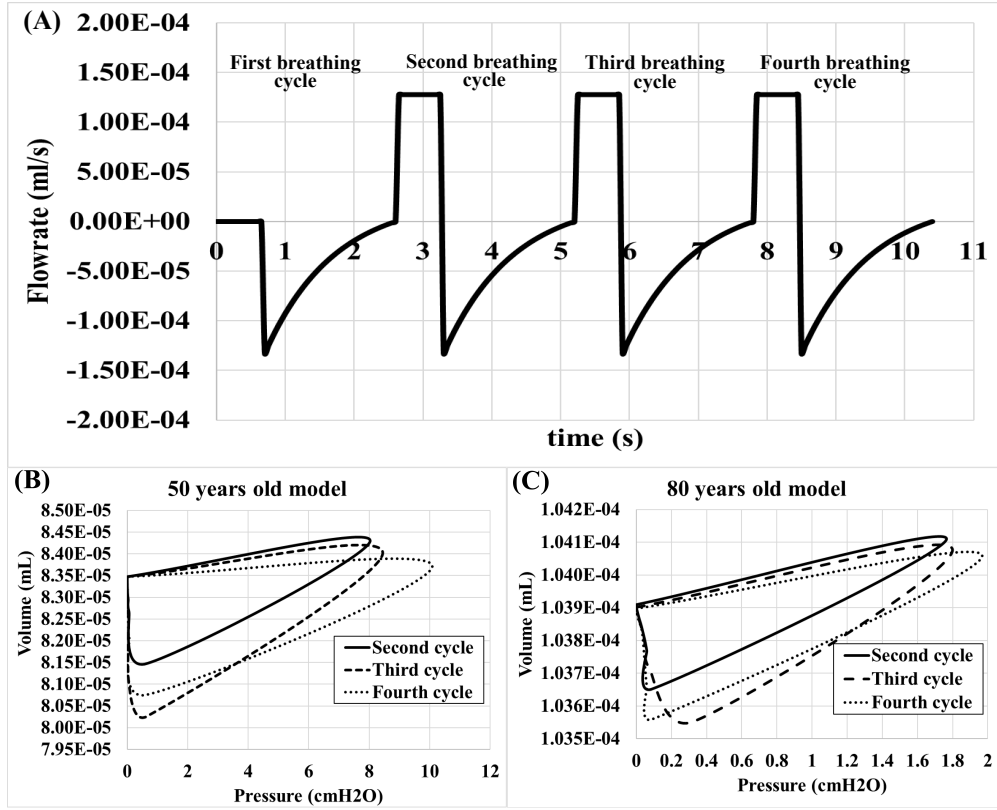


Figure 3.4: Flowrate waveforms for four breathing cycles and pressure-volume loop for different breathing cycles for (B) Model with morphological and tissue properties of the 50-year-old alveolar sacs (Case1) and (C) Model with morphological and tissue properties of the 80-year-old alveolar sacs (Case 4).

3.7.3 EFFECTS OF AGE-RELATED CHANGES ON WOB

WOB is defined as the energy required to inhale oxygen and exhale carbon dioxide. The area enclosed by the pressure-volume loop is a measure of the WOB. The magnitude of the WOB depends on the ventilation associated with a given effort and the mechanical efficiency of the chest wall. It is expected that an older person could sustain a given ventilation by applying smaller forces to the thoracic cage, with a corresponding reduction in the elastic WOB [30]. The area enclosed by pressure-volume loops for 50 and 80-year-old alveolar sacs were calculated. It was hypothesized that older alveolar sacs would have smaller WOB compared

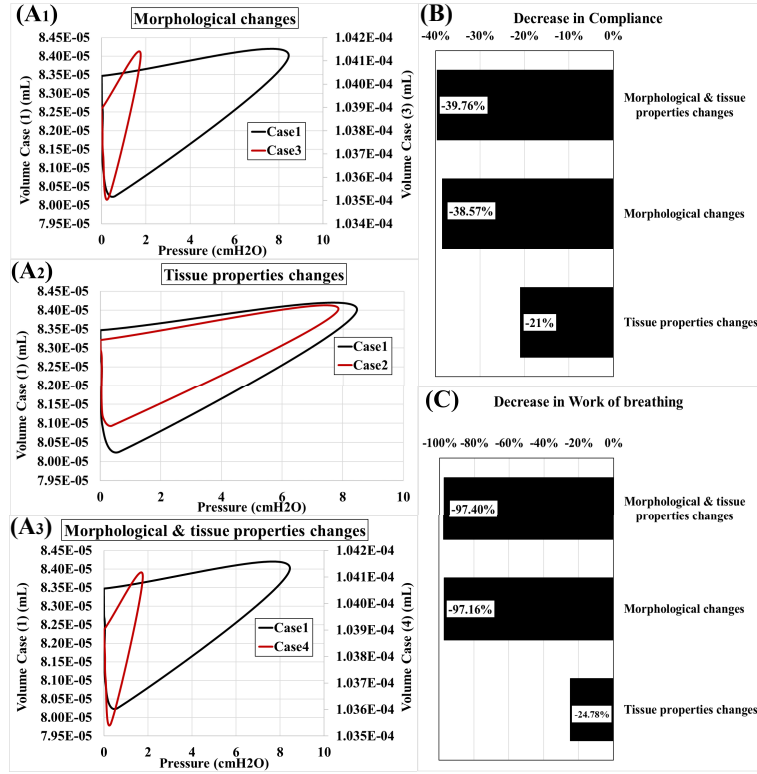


Figure 3.5: (A_1 - A_3) Pressure-volume plots for considered case studies (case 1 with morphological and tissue properties of the 50-year-old alveolar sacs, case 2 morphological of 50-year-old alveolar sacs and tissue properties of 80-year-old alveolar sacs, Case 3 with morphological of 80-year-old alveolar sacs and tissue properties of 50-year-old alveolar sacs, Case 4 with morphological and tissue properties of 80-year-old alveolar sacs) and contribution of tissue properties and morphological changes in older alveolar sacs compliance decline (B) and WOB decrease (C) .

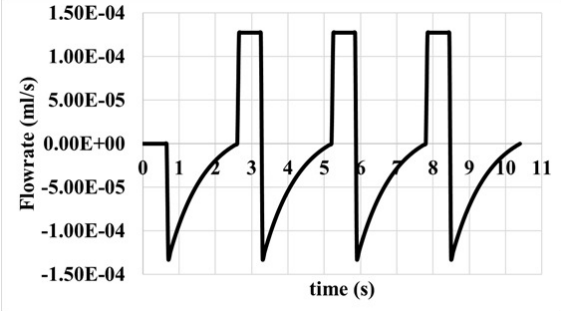
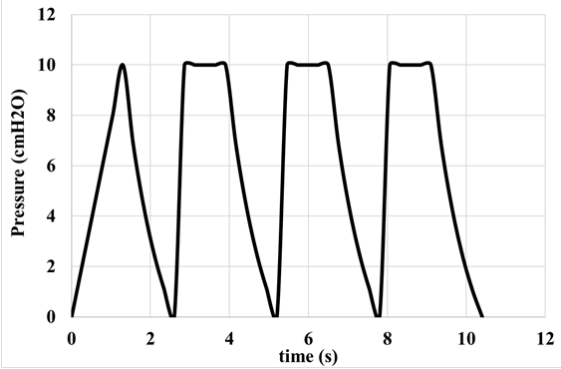
to younger models, and results confirmed that morphological changes are the main reason for the decrease in WOB magnitude (see Figure 3.5C).

However, increase in the rigidity of the chest wall and airway collapse both augment resistive work, so the total WOB is likely to be greater in an older person in comparison to a younger person. In order to capture the increase in WOB, applied pressure on the diaphragm has to be considered in future in the simulations.

3.7.4 INFLUENCE OF MV MODE ON ALVEOLAR SACS FUNCTION

MV mode influence on alveolar sacs mechanics was evaluated for the 80-year-old alveolar sacs model. According to previous studies, volume-controlled mode decreases distending pressure compared to pressure-controlled mode [97]. It was therefore hypothesized that applied pressure in volume-controlled mode would be smaller compared to applied pressure in pressure-controlled mode. Furthermore, measured pressure and volume for volume-controlled and pressure-controlled mode were normalized and corresponding WOB and compliance values for volume-controlled and pressure-controlled modes were calculated and compared. As shown in Table 3.1, WOB increased by 10 percent for volume-controlled mode while volume-controlled mode decreased compliance by almost 52 percent compared to pressure-controlled mode.

Table 3.1: MV mode effects on 80-year-old alveolar sacs mechanics

Waveforms		Maximum applied pressure (cmH_2O)	WOB for normalized pressure	Compliance for normalized pressure
Volume-controlled		1.77	0.56	0.46
Pressure-controlled		10	0.51	0.98
Remarks		80% decrease in volume-controlled	10% increase in volume-controlled	52% decrease in volume-controlled

3.7.5 INFLUENCE OF INDIVIDUAL DIFFERENCES ON ALVEOLAR SACS FUNCTION

A 0.05 significance level and two-tailed z test were employed in this study. Accordingly, upper and lower tail were set equal to 0.025. The z values that corresponds to upper and lower tail are -1.96 and 1.96. Thus, the null hypothesis of no difference will be rejected if the computed z statistic falls outside the range of -1.96 to 1.96. Computed z statistics for

alveolar sacs compliance and WOB were equal to -0.95 and -1.55, respectively. Therefore, the null hypothesis of no difference could not be rejected. Moreover, estimated range of values that include 95% of compliance and WOB values from considered case studies with morphological and tissue properties between 75 to 85-years-old alveolar sacs are presented in Table A.4. It was observed that individual differences resulted in less than 10% difference for both compliance and WOB values in the elderly (see Table A.4). This difference is considered negligible. Therefore, results from this study are applicable and can be generalized to the elderly.

3.7.6 SENSITIVITY OF ALVEOLAR SACS FUNCTION TO MV DEVICES SETTING

Since volume-controlled mode has been recently identified as the preferred mode for ventilator devices, sensitivity of alveolar sacs mechanics (WOB, strain and compliance) to ventilator devices settings in the volume-controlled mode (TV, breathing frequency and I/E) was measured. Changing MV parameters can improve breathing condition. For instance, previous studies have shown that the adoption of a slower expiration may reduce premature airway collapse occurrence. This will not only be helpful in its own right but will also reduce the WOB and ventilatory demand [30]. Therefore, the considered values for TV, breathing frequency and I/E in this study were increased and decreased by 10 percent and FSI was conducted for all case studies. Results indicated that decreasing I/E increases WOB, compliance and strain significantly. An increase in frequency also increased WOB and strain and compliance. Increasing frequency had the most influence on strain enhancement. Decreasing TV also decreased WOB and strain but increased alveolar sacs compliance as shown in Figure 3.6. Although, increasing frequency and decreasing I/E increases WOB, it also increases alveolar sacs and compliance. Therefore, increasing breathing frequency and decreasing I/E and TV would improve breathing conditions for older alveolar sacs under MV.

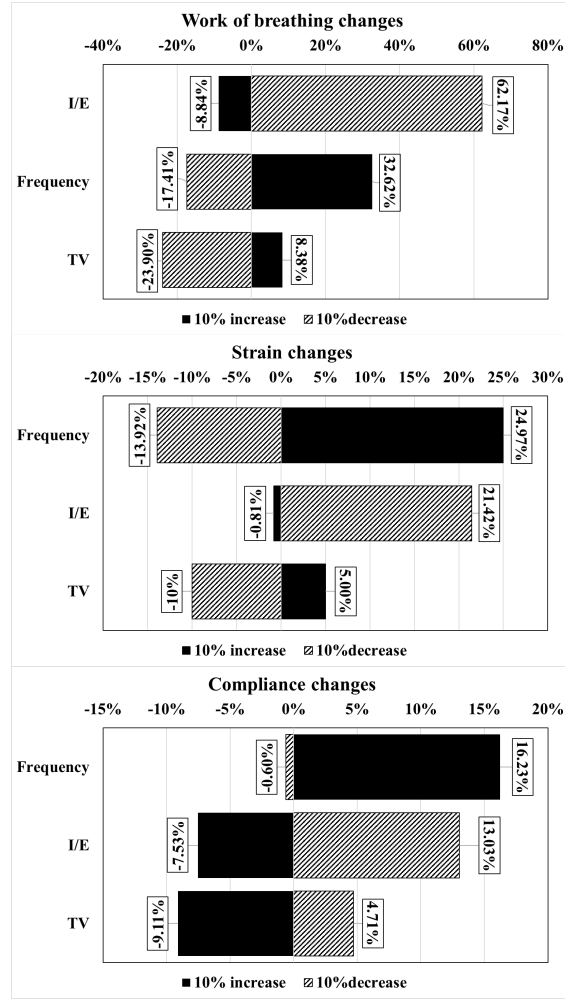


Figure 3.6: Sensitivity of WOB, strain and compliance to volume-controlled mode parameters (TV, breathing frequency and I/E).

3.8 LIMITATIONS

Fixed longitudinal displacement was considered as a boundary condition for the solid domain in the FSI analysis in this study. While elastic support could be considered in future studies, access to bronchiole tissue properties changes with age will be required. In addition, a decrease in WOB of older alveolar sacs was observed while an increase in the rigidity of the chest wall and airway collapse resulted in greater total WOB in an older person in

comparison to a younger person. Therefore, applied pressure on the diaphragm has to be considered in the simulations to capture the increase in WOB.

3.9 CONCLUSIONS

Aging is associated with morphological and tissue properties changes in alveolar sacs that would influence alveolar sacs functionality significantly. FSI was employed to study younger (50) and older (80) alveolar sacs models under MV. Older alveolar sacs had lower pressure compared to younger alveolar sacs models. Findings also indicated that morphological changes have a major impact on decline in alveolar sacs function. Alveolar sacs enlargement in older models led to a decrease in compliance of alveolar sacs and WOB. Although WOB is decreased in single alveolar sacs, an increase in the rigidity of the chest wall would neutralize this decrease in WOB. In reality, WOB would increase in older patients. Apart from morphological and tissue properties changes in alveolar sacs, ventilator device settings may also influence their functionality, specifically in older patients. MV mode was altered from volume-controlled mode to pressure-controlled mode and it was observed that applied pressure on alveolar sacs wall decreased in volume targeted mode and WOB increased in volume-controlled mode as compared to pressure-controlled mode while compliance decreased significantly in volume-controlled mode. Statistical analysis illustrated that influence of individual differences on alveolar sacs function is negligible and results are applicable to the elderly. The results of sensitivity of alveolar sacs under volume-controlled mode showed that their function is highly sensitive to I/E and breathing frequency. Therefore, increasing frequency and decreasing I/E would increase alveolar sacs expansion and compliance. Decreasing TV decreases WOB while increases in the other two parameters increases WOB. Consequently, increasing breathing frequency and decreasing I/E and TV would help improve breathing conditions for older patients under MV.

CHAPTER 4

FRACTAL GEOMETRICAL AND STRUCTURAL PROPERTIES OF NORMAL AND DISEASED BRONCHIAL TREE WITH AGE ¹

¹P. Aghasafari and R. Pidaparti. “Fractal Geometrical and Structural Properties of Normal and Diseased Bronchial Tree with Age.” To be submitted to IEEE Transactions on Biomedical Engineering. *First coauthor.

ABSTRACT

Fractals are mathematical constructs that provide information about self-similarity and the morphological complexity by non-integer fractal dimension (FD). Fractal dimension (FD) of bronchial tress can be employed to evaluate geometrical complexity, and the irregularity of shapes and patterns observed in respiratory disease. In addition, electrical analogy of elastic airways can be used to provide insights on changes in mechanical properties of airways. This study focused on changes in geometrical complexity of normal and diseased bronchial tree with age using FD measures and estimated the respiratory airways resistance, compliance and air inertia within airways using their equivalent electrical model. Observation from this study illustrated that lower airways sustain more significant changes compare to upper airways. Results from this study could provide invaluable insights about respiratory disease and changes in mechanics of breathing with age.

4.1 INTRODUCTION

Bronchial tree has a progressively branching structure, which consists of trachea, bronchi, bronchioles, alveolar ducts, alveolar sacs, and alveoli. It conducts air from the trachea into the lungs. Human bronchial tree develop up to 25-year-old and start to lose its functionality approximately at 35-year-old [31]. Different parameters influence breathing condition during our lifetime such as; age and respiratory disease. Complex morphology of the bronchial tree causes difficulty in diagnosis and visual interpretation of age-related changes and respiratory disease, such as Asthma and chronic obstructive pulmonary disease (COPD) [3]. In addition, pulmonary function tests are not very sensitive measures of lung disease specifically in early stages of respiratory diseases [4] and we can not repeat the tests to confirm decisive assumption. Hence, mathematical models provide alternative to repeating experimental tests.

Fractal geometry are the best existing mathematical descriptions of lots of natural forms, such as bronchial tree [17]. It can be used to estimate geometrical complexity, and shapes

irregularity in lung [16]. Mandelbrot presented the first fractal airways structure [103]. Fractals have three main properties. First, self-similarity, whereby any small piece of the fractals is an exact replica of the whole [104]. Second, scale-free properties which means that they appear the same over multiple scales [105]. Third, fractal have a non-integer FD that describes morphological complexity, and provides information on the self-similarity properties of the fractal geometry [106]. Since most of lung diseases affect the morphology of the bronchial tree, the FD of the bronchial tree as its morphological measures offer an alternative way for quantitative respiratory disease evaluation [16, 17].

The FD is an index of the space-filling properties of lung [107], which is related to existing asymmetry in healthy bronchial tree and the optimality of ventilation, whereas a diseased bronchial tree contains significant heterogeneities and the optimal ventilation conditions are not anymore fulfilled [22]. Therefore, we can employ the FD to evaluate the amount of progress, and type of respiratory disease. Several methods have been developed to estimate the FD of bronchial tree for optimizing computation time, or reaching better precision. Box counting dimension is a way of determining the FD of a fractal geometry and is equal to number of required boxes to cover the geometry in MRI images [16, 18–21]. Other study presented FD of the bronchial tree using a modeling technique based on one of the variants of the Von Koch curve [17]. More-complete descriptions of the other methods of calculating FD in fractal objects have been described in previous studies [108, 109]. Although, different algorithms are used in each method, but they all follow the same basic premise: they measure the specific characteristic of an object at different scales, then plot logarithm of these characteristic versus logarithm of scale, and fit a least-squares regression line to the plot. The slope of the resulting line is equivalent to the FD of the fractal object [108].

In addition, electrical analogy for elastic airways that combines tidal breathing conditions and bronchial trees morphology provides insight on changes in mechanical parameters of the respiratory airways such as resistance, inertance, and compliance of the respiratory airways. Previous studies developed equivalent electrical models and estimated changes in resistance,

inertance, and compliance parameters in healthy and diseased airways [22, 23] but none of them focused on the age-related changes in mechanical properties of bronchial tree. It would be interesting to use equivalent electrical model to investigate changes that might happen in mechanical parameters of normal and diseased airways with age.

This study estimated the FD dimension and mechanical parameters of normal and diseased bronchial tree with age and is divided into two main sections: the first section presents the fractal model of bronchial trees and investigate the influence of aging and respiratory disease (asthma and COPD) on FD and space filling of bronchial trees. The second section is devoted to derivation of resistance, inertance, and compliance airways at different bifurcation level at 20, 50 and 80-year-old case studies. Results are compared and the most sensitive bifurcation generations to the influence of aging and respiratory disease are highlighted.

4.2 METHODS

Since bronchial tree is a 3D fractal structure and most of lung diseases affect the morphology of the bronchial tree, we calculated FD of the bronchial tree for quantitative lung aging and disease (asthma and COPD) evaluation. We employed mathematical description for lung with COPD and asthma in previous studies. We altered airways radius and thickness to simulate disease condition in bronchial tree. Where airway wall inflammation and thickening with mucus in asthma are represented by altering the radius by $R - 0.5 \times h$ and wall thickness by $1.5 \times h$. Increased resistance and airway wall thickening in COPD have been represented by $R - 5 \times h$ and $6 \times h$ in small conducting airways (levels 11-13) and by $1.5 \times R$ in acinar airways (levels 13-24), combined with alveolar wall destruction of the emphysematous lung parenchyma with thickness equal to 0.00001 mm. We presented that airways diameter has a power-law distribution versus bifurcation generations which illustrate self-similarity properties of bronchial trees. We calculated the slope of the best linear segment of the log-log plot of airways diameter versus generation level for normal lung and lung with COPD and asthma at three different age (20, 50 and 80-year-old), by performing the least-square

method iteratively over all linear segments and equate it to the FD measure.

The history of the concept of botanical tress back to the Leonardo da Vinci statement; “the cross-sectional area of the trunk is equal to the sum of the cross-sectional areas of the branches within each generation” [110]. Therefore, the diameter of the daughter braches should be relevant to the diameter of the parent branch. Figure (4.1) depicts a schematic representation of an airway bifurcation from parent airways to two branching daughters.

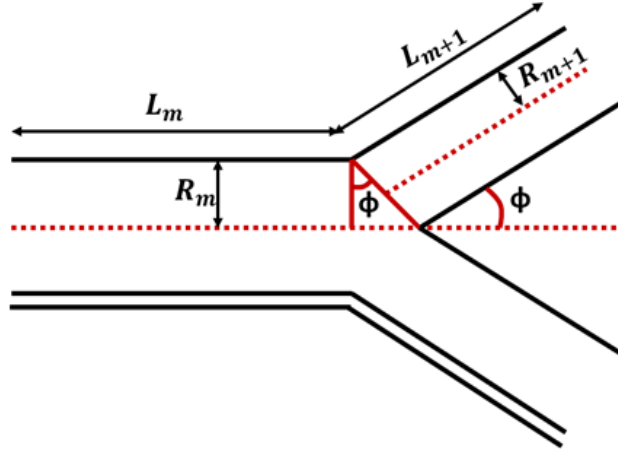


Figure 4.1: Schematic representation of an airway branch bifurcation in bronchial tree.

We constructed symmetrical bronchial tree models from generation level 11 to 24 at different age for normal and diseased lung using actual morphometric data for human airways radius (R), length (L) [111,112] and computed bifurcation angle within consecutive generation levels (m, m+1) by Eq. (4.1) and compared space filling trees for normal and diseased trees at different age.

$$\cos\phi = \frac{R_m}{2R_{m+1}} \quad (4.1)$$

4.3 EQUIVALENT ELECTRICAL MODEL FOR BRONCHIAL TREE

We also estimated the mechanical parameters of the respiratory airways (resistance, inductance, and compliance) utilizing morphological parameters to correlate pathologic changes with fractional-order models. For this aim we considered electrical equivalent for airways

resistance, inertance and compliance similar to the approach in Ionescu et al study [22]. The discussed mechanical parameters can serve as elements in a transmission line equivalent Fig. (4.2), whose structure preserves the geometry of the human respiratory tree.

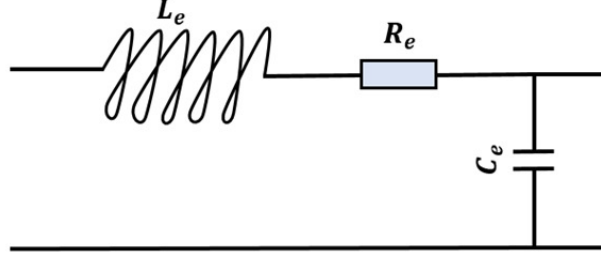


Figure 4.2: Schematic representation of an airway branch bifurcation in bronchial tree.

In this approach, electrical resistance R_e ($kPas/l$) is equivalent to airway resistance resulted from airflow dissipation. Electrical capacitors C_e (l/kPa) is equivalent to airways volume compliance, which is a measure of the airways ability to stretch, and expand and electrical inductors L_e ($kPas^2/l$) is equivalent to airways inertance which is relevant to inertia of air in the airways. As it has been shown in Ionescu study, airways resistance, inertance and compliance can be estimated in terms of morphological parameters of airways such as; airways wall thickness, inner radius, length, and tissue structure as follow:

$$R_e = l \frac{\mu \delta^2}{\pi R^4 \dot{M}_0} \sin(\varepsilon_0) \quad (4.2)$$

$$L_e = l \frac{\rho}{\pi R^2 \dot{M}_0} \cos(\varepsilon_0) \quad (4.3)$$

$$C_e = l \frac{2\pi R^3 (1 - \nu^2)}{Eh} \quad (4.4)$$

$$\delta = R \sqrt{\frac{\omega \rho}{\mu}} \quad (4.5)$$

$$\omega = 2\pi f \quad (4.6)$$

$$\dot{M}_0 e^{\varepsilon_0} = 1 - \frac{2J_1(\delta j^{\frac{3}{2}})}{J_0(\delta j^{\frac{3}{2}}) \delta j^{\frac{3}{2}}} \quad (4.7)$$

The parameters used in the above equations represent airway inner radius (R), airway length (l), tissue young modulus (E), tissue thickness (h), Dynamic viscosity of air (ρ) equal

to 1.075, Poisson ratio (ν) equal to 0.45, Phase angle of complex Bessel function of first kind and order zero (ε_0) (Eq. 4.7), Modulus of complex Bessel function of first kind and order zero (\dot{M}_0) (Eq. 4.7), Womersley parameter (δ), angular frequency (ω) and breathing frequency (f) equal to 0.2 (hertz) in this study. We used presented morphological parameters in previous studies Table (4.1) and calculated normal and diseased airways resistance, inertance, and compliance from generation 11 to 24 for 20,50 and 80-year-old case studies and compared the results and illustrated the influence of aging, COPD and asthma on mechanics of breathing.

Table 4.1: Alveolar Sacs' dimensions for current study

Generation		11	12	13	14	15	16	17	18	19	20	21	22	23	24
20	R (mm)	1.2	0.65	0.52	0.40	0.32	0.25	0.24	0.23	0.18	0.16	0.14	0.12	0.1	0.06
	l (mm)	9.50	6.95	6.42	4.37	3.59	2.29	2.02	1.5	1.39	1.25	1.09	0.98	0.85	0.59
	$h \times 10^{-3}$	6.91	6.91	6.38	5.85	5.85	5.31	5.31	4.78	4.78	5.59	5.12	4.20	4.28	3.57
	$E \times 10^4$	6.97	6.97	6.74	6.61	6.55	6.49	6.37	6.31	6.17	6.05	5.37	5.37	5.37	5.37
50	R (mm)	0.93	0.50	0.40	0.31	0.25	0.19	0.18	0.18	0.14	0.13	0.11	0.09	0.08	0.04
	l (mm)	7.31	5.35	4.94	3.36	2.76	1.76	1.55	1.15	1.07	0.96	0.84	0.75	0.64	0.45
	$h \times 10^{-3}$	11.52	11.52	10.63	9.74	9.74	8.86	8.86	7.97	7.97	7.26	6.64	6.00	5.56	4.63
	$E \times 10^4$	7.79	7.79	7.53	7.39	7.32	7.25	7.12	7.05	6.89	6.76	6.00	6.00	6.00	6.00
80	R (mm)	0.65	0.35	0.28	0.21	0.17	0.13	0.12	0.13	0.09	0.09	0.07	0.07	0.06	0.03
	l (mm)	5.12	3.75	3.46	2.35	1.93	1.23	1.09	0.81	0.75	0.67	0.59	0.53	0.42	0.32
	$h \times 10^{-3}$	14.97	14.97	13.81	12.66	12.66	11.51	11.51	10.36	10.36	9.43	8.62	7.80	7.22	6.02
	$E \times 10^4$	8.60	8.60	8.32	8.17	8.09	8.02	7.87	7.79	7.61	7.47	6.63	6.63	6.63	6.63

4.4 RESULTS

4.4.1 MORPHOLOGICAL CHANGES IN NORMAL AND DISEASED LUNG WITH AGE

In order to monitor morphological changes in human airways with disease, we plotted airways radius versus generation numbers for normal and diseased lungs. We observed that changes within airways dimensions could be represented by power law distribution, which means that

a relative change in airways generation results in a proportional relative change in airways radius. This presents self-similarity properties of lung as fractal geometries (Fig 4.3).

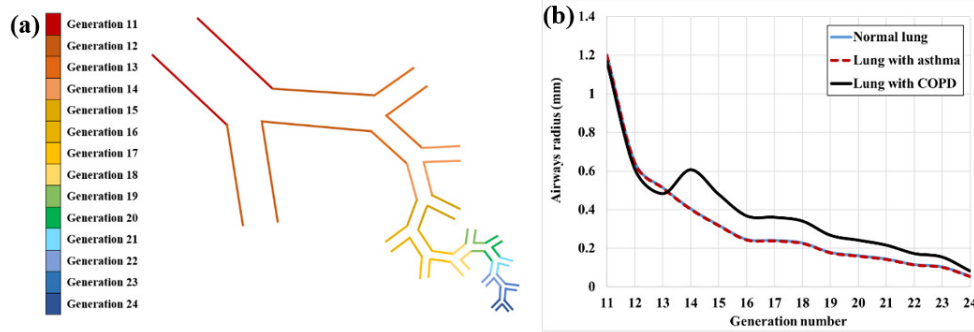


Figure 4.3: a) Bronchial tree and normal and b) diseased airways radius versus bifurcation generation.

To compute FD in normal and diseased lung at different age group, we plotted log-log graphs of the reciprocal of the airways diameter, against the airways generation number. The slope of the best linear segment of the graph, calculated by performing the least-square method iteratively over all linear segments represented the FD of the considered case studies. We observed that asthma increased FD and this increase has upward trend, as we get older. In contrast, COPD decreased FD significantly and as we get older decrease in FD became more significant in lungs with COPD. We also observed that FD decreased, as we get older in normal and COPD condition, while FD increased in older lungs with asthma (Fig 4.4).

We also plotted lung fractal trees based on airways diameter and length and existing relation between airways radius of consecutive levels. We observed shrinkage in lung fractal tress as we get older (Fig 4.5 a, c) and we declared that COPD led to increase in space feeling region compare to normal lung (Fig 4.5 b) and observed small decrease in lung space-filling with asthma (Fig 4.5 b).

4.4.2 AGING AND AIRWAYS DISEASE INFLUENCE ON MECHANICS OF BREATHING

We investigated the influence of Age and respiratory diseases on mechanics of breathing at different airways level. For this aim, we calculated the ratio of airways resistance, compli-

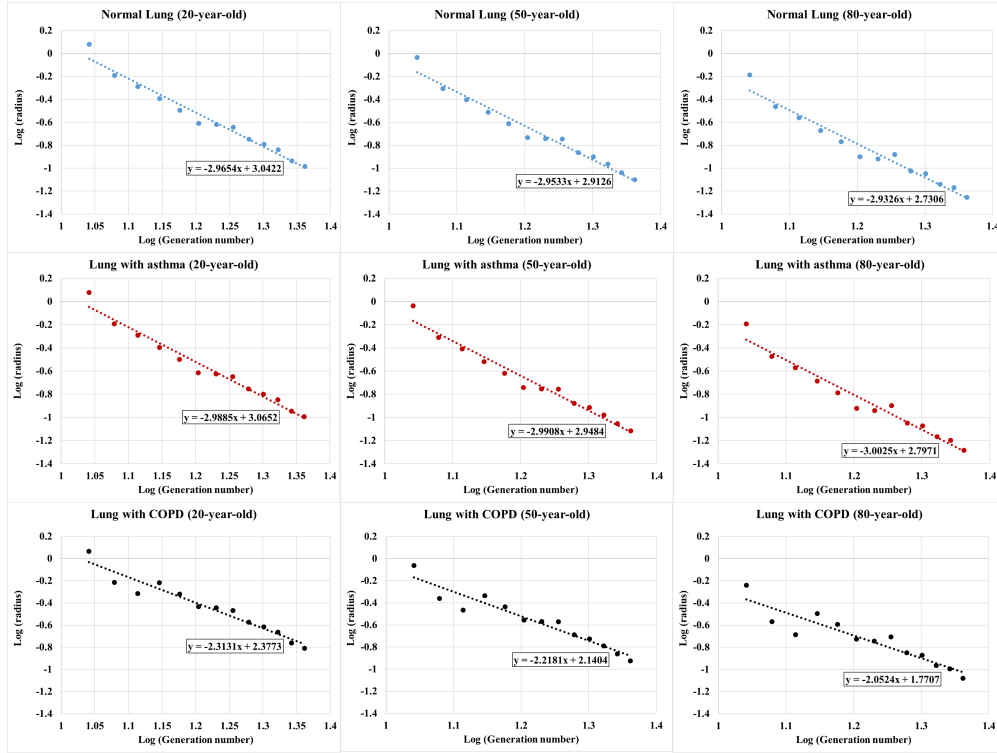


Figure 4.4: FD of normal and diseased bronchial tree at 20, 50 and 80-year-old case studies.

ance and air inertance from 20 to 50-year-old and from 50 to 80-year-old. We observed that changes from 50 to 80 are more significant than the changes from 20 to 50-year-old. Lower airways sustained larger changes compare to upper airways. For example, airways resistance increased by 2 times from 20 to 50 years old while from 50 to 80-year-old the resistance in upper airways increased by 6 times and level 24,21 and 17 respectively had the biggest changes by 12, 8.5 and 8.5 times compare to other airways level (Fig 4.6 a_1). We also observed that asthma increased airway resistance at lower airways level while COPD increased airways resistance at upper airways (generation 11, 12 and 13) and decreased airway resistance by 0.4 time at airways generation 14 to 24 (Fig 4.6 a_2, a_3).

Aging would not change air inertance significantly compare to airway resistance. For instance, air inertance almost increased by 1.5 times from 20 to 50-year-old while it increased

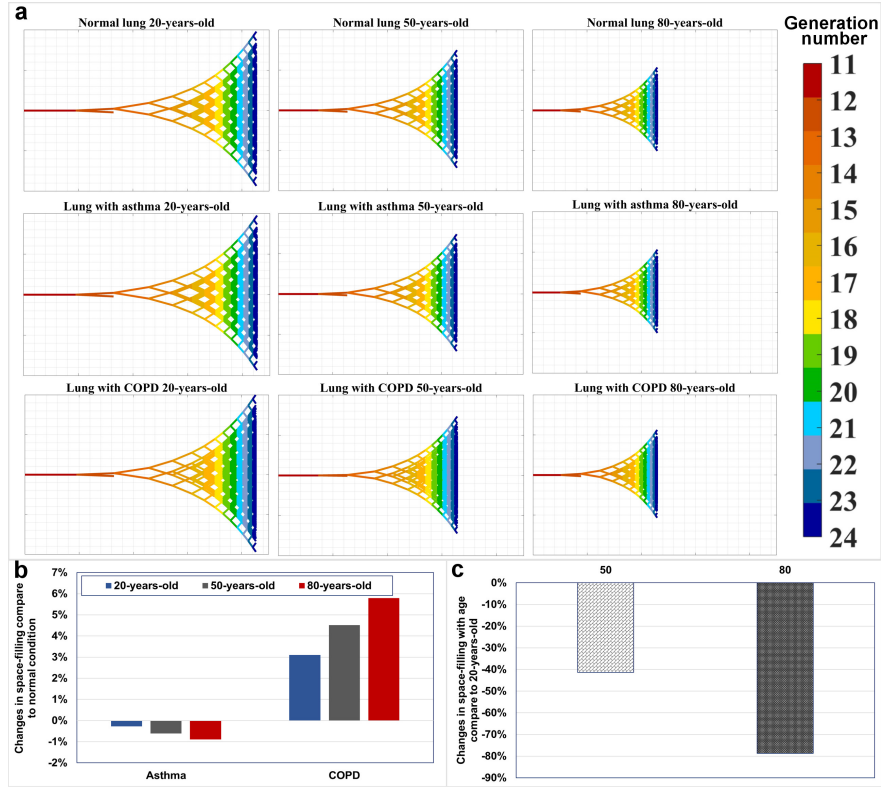


Figure 4.5: a) Normal and diseased lung fractal tree at 20, 50 and 80-year-old case studies. b) Changes in lung space-filling in diseased condition compare to normal condition at 20, 50 and 80-year-old. c) Changes in lung space-filling with age compare to lung space-filling at 20-year-old case study

by 2 times from 50 to 80-year-old. Similarly, generation 24, 21 and 17 had the highest inertance ratio from 50 to 80-year-old by 2.5 and 2.2 and 2.2 times (Fig 4.6 b_1). We discovered the changes for air inertance are similar to changes for airways resistance. Asthma increased air inertance at lower levels by 1.2 time and COPD increased it by 1.3, 1.6 and 1.8 times at airways level 11, 12 and 13 and decreased it by 0.4 times at all age ranges (Fig 4.6 b_2, b_3). In addition, we observed that aging decreased airways compliance at all generation levels. By getting older decrease in compliance became more significant where we calculated almost 0.05 times decrease in compliance from 20 to 50-year-old and 0.2 times decrease from 50 to 80-year-old and detected bigger changes at generation level 20 to 23 by 0.25 times decrease

in airways compliance (Fig 4.6 c_1). We demonstrated that asthma decreased the airways compliance compare to normal condition while COPD increased airways compliance specifically at lower airways level. We presented that asthma decreased compliance by almost 0.65, 0.6 and 0.55 at 20, 50 and 80-year-old respectively and the largest decrease happened at alveolar sacs (generation 24). COPD mostly influenced lower airways generation from 18 to 24 and increased airways compliance significantly. It significantly increased compliance at generation 18 compared to other generation (Fig 4.6 c_2, c_3).

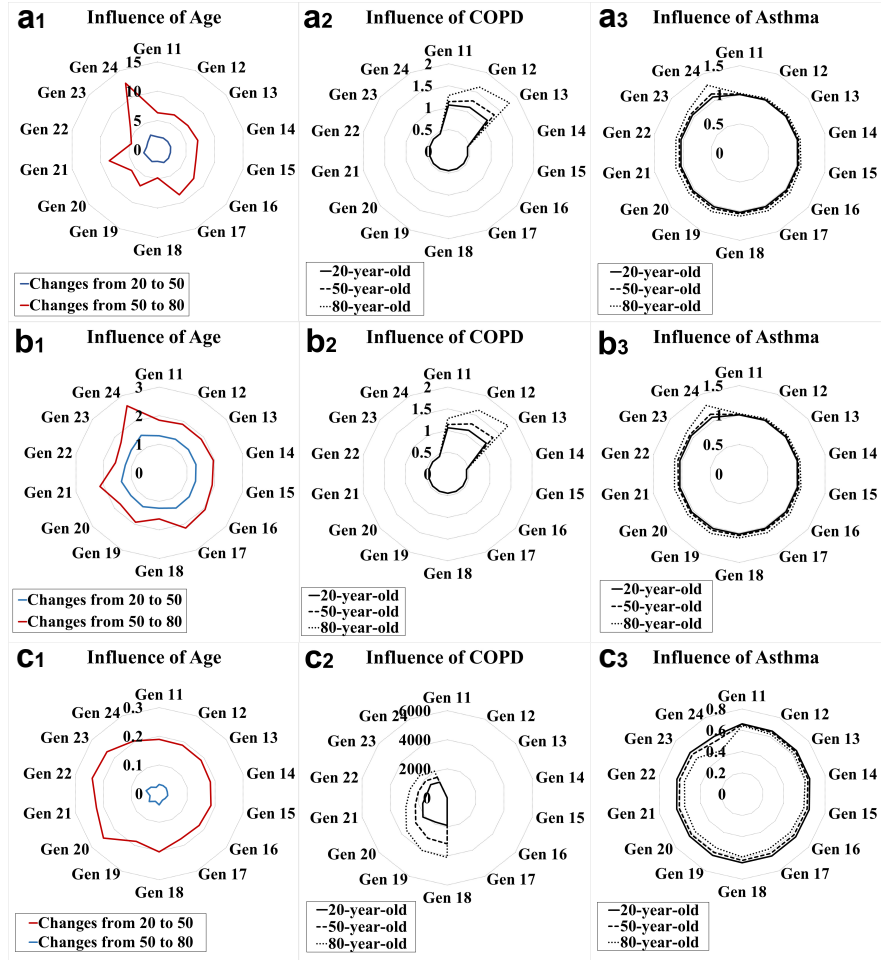


Figure 4.6: Ratio of changes in mechanical properties of airways from 20 to 50-year-old and 50 to 80-year-old (a_1, b_1, c_1) and mechanical properties of diseased airways at 20, 50 and 80-year-old (a_2, a_3 : Airways resistance, b_2, b_3 : Airways inertance, c_2, c_3 : Airways compliance)

4.5 CONCLUSION

Since most of respiratory disease influence morphology of bronchial trees, we employed FD of the bronchial tree as morphological measure to evaluate lung disease quantitatively. In addition, we employed equivalent electrical model to investigate the influence of age, asthma and COPD on airways resistance, inertance and compliance. We observed that airways radius versus bifurcation level can be represented by power-law distribution, which shows scale-free properties of bronchial trees. Log-log plot of airways radius versus bifurcation level shows linear trend, which illustrates self-similarity of bronchial tree. We observed that asthma increased FD while COPD decreased FD and FD declines as we get older in normal and COPD cases whereas it rose in lung with asthma. Changes in mechanical properties of airways at different bifurcation level from 50 to 80-year-old were more significant than changes from 20 to 50-year-old. Lower generations sustained bigger changes compare to upper airways. Asthma mostly increased airways resistance and air inertia at lower airways while COPD increased discussed parameters at upper airways. Changes in air inertance with age is not as big as changes in airways resistance with age. We also observed that asthma declined airways compliance compare to the normal condition and COPD significantly increased airways compliance at lower airways.

CHAPTER 5

STRAIN-INDUCED INFLAMMATION IN PULMONARY ALVEOLAR TISSUE DUE TO MECHANICAL VENTILATION ¹

¹P. Aghasafari, I.B. M.Ibrahim and R. Pidaparti. “Strain-induced Inflammation in Pulmonary Alveolar Tissue due to Mechanical Ventilation.” Accepted by Biomechanics and modeling in mechanobiology (2017): Reprinted here with permission of publisher. *First coauthor.

ABSTRACT

Inflammation is the body's attempt at self-protection to remove harmful stimuli, including damaged cells, irritants, or pathogens and begin the healing process. In this study, strain-induced inflammation in pulmonary alveolar tissue under high tidal volume is investigated through a combination of an inflammation model and FSI analysis. A realistic three-dimensional (3D) organ model for alveolar sacs is built and fluid structure interaction (FSI) is employed to evaluate strain distribution in alveolar tissue for different tidal volume (TV) values under the mechanical ventilation (MV) condition. The alveolar tissue is treated as a hyperelastic solid and provides the environment for the tissue constituents. The influence of different strain distributions resulting from different tidal volumes is investigated. It is observed that strain is highly distributed in the inlet area. In addition, strain versus time curves in different locations through the alveolar model reveals that middle layers in the alveolar region would undergo higher levels of strain during breathing under the MV condition. Three different types of strain distributions in the alveolar region from the FSI simulation are transferred to the CA model to study population dynamics of cell constituents under MV for different TVs; 200, 500 and 1000 ml respectively. The CA model results suggests that strain distribution plays a significant role in population dynamics. An interplay between strain magnitude and distribution appears to influence healing capability. Results suggest that increasing TV leads to an exponential rise in tissue damage by inflammation.

5.1 INTRODUCTION

Inflammation is an immune response to tissue stimulation and is a complex process that involves diverse tissue constituents. It can be triggered by foreign matter entering the tissue, or a mechanical signal. Inflammation that occurs when Mechanical Ventilation (MV) is applied to support breathing in an alveolus environment is known to be induced by applied strain on the tissue, which may be caused by over-inflating the airways. In the case of MV,

this leads to a dilemma—MV is necessary to maintain respiration, but it may also cause the lung to fail by inflammation related problems. In particular, the pressure needed to maintain respiration under MV is more than normal breathing pressure. This is necessary to open presumed collapsed alveoli. The mechano-sensitive nature of pulmonary tissue has been known for a long time. Foda et al [13], focused on identifying major factors in the development of ventilator-induced lung injury. They demonstrated that high volume ventilation caused acute lung injury. Copland et al [14], studied the influence of high lung tidal volume and gene activation induced by mechanical stretch that occurs in the absence of physiologic or structural impairments in rat lung. They concluded that the pattern of gene activation that precedes high lung tidal volume-induced injury plays a significant role in the pathogenesis of high tidal volume-induced lung injury. Carnell et al [15], developed a histology-based methodology to explore the relation between intramural stress and combined monocyte/macrophage density and arteries branch elevation. They also tested the correlation between elevated stresses in hypertensive bifurcations and inflammation increase. They observed that cell density peaks appeared in regions where surface curvature would cause stress concentrations. They also concluded that there is a strong positive correlation between mean stress and cell density in each bifurcation. Experimental studies [113–115] infer the mechanotransduction nature of lung tissue cells by statistical measurement of cytokines expression after they are subjected to stress. These results however, ignore factors such as strain level and distribution. There is also an issue of reproducibility where some cytokines are easily released in vitro but not in vivo. Several studies have shown that various cell signaling pathways were activated by subjecting pulmonary tissue to static or cyclic stretch. The cell signaling pathways during pulmonary tissue stretch may produce a number of proteins involved in inflammation, including p38 [114,116], MAPK [116], IL-8 [117], MMP-2 [118], ERK and NF-B [119], MMP-9 [120] and NOS [121], that are responsible for producing TNF, a well-known cytokine associated with inflammation. It is recognized that cytokines are redundant; hence these cytokines may be released by the same triggers. These various cytokines would play different roles in

inflammation; some would cause inflammation or dysfunction of other organs and are the precursor to biotrauma during MV. One way to study complex interactions between cells and cytokines in the pulmonary tissue environment is to treat the interaction as a discrete network. Insights might be gained from studying dynamics emerging from this interaction. In this study, two different models are employed to study the strain-induced inflammation in the pulmonary alveolar tissue environment. First, a realistic three-dimensional (3D) organ model for alveolar sacs is built and fluid structure interaction (FSI) is employed to evaluate strain distributions in alveolar tissue under the MV condition. Alveolar tissue is treated as a hyperelastic solid and provides the environment for the tissue constituents. The tissue constituents are mechano-sensitive cells that give rise to the dynamics at the cellular level by bio-chemical signaling. Second, a discrete network system modeled by Cellular Automata (CA) was used to represent the cellular model. Post processed strain distributions from FSI are applied to the CA model to study population dynamics of cell constituents of tissue under the MV condition. The results obtained from both the models regarding the mechanical environment in alveolar tissue are discussed.

5.2 MATERIALS AND METHODS

To investigate the strain-induced inflammation in a pulmonary alveolar tissue environment, both fluid-solid interaction (FSI) and cellular automata (CA) models are employed. A realistic 3D organ model for alveolar sacs is built and hyperelastic material properties are assigned to the alveolar tissue. FSI is conducted to obtain strain distributions in alveolar tissue under MV condition. Appropriate boundary conditions are defined for FSI analysis and governing equations for fluid and solid domain are solved iteratively to obtain the strain distributions in alveolar tissue. These strains from FSI are applied to the CA model to study cell population dynamics of the tissue. Figure 5.1 presents an overview of the strain-induced inflammation model considered in this study.

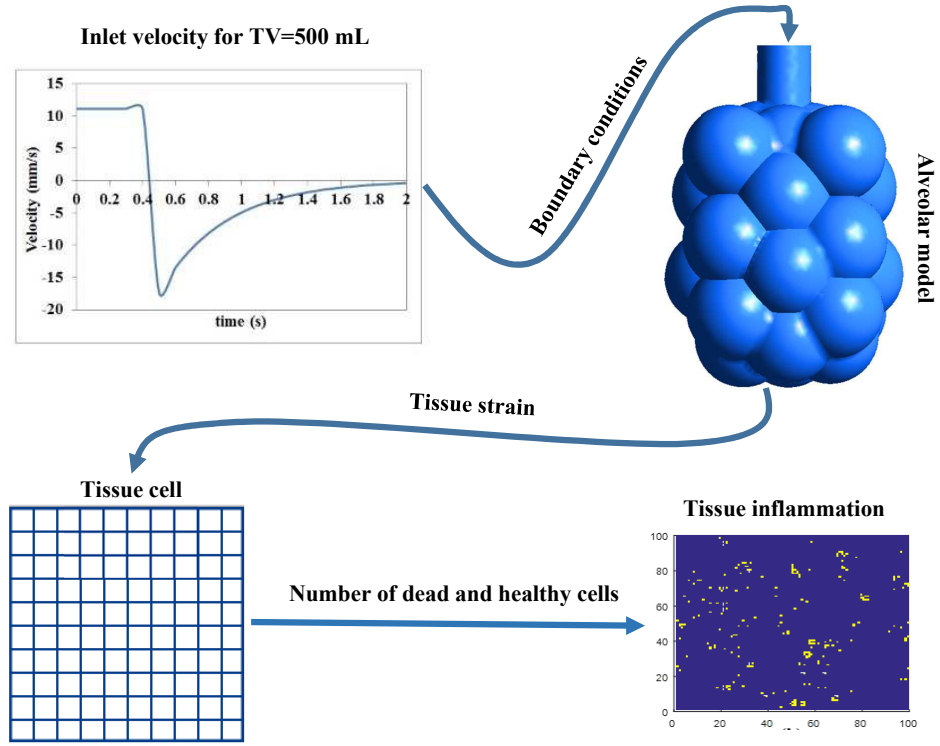


Figure 5.1: Overview of strain-induced inflammation in this study

5.2.1 FLUID SOLID INTERACTION (FSI)

FSI studies that include both solid and fluid domains were used to investigate strain distributions in the alveolar region [74]. A 3D realistic geometry of the alveolar region is created based on realistic dimensions [80, 81, 122] and it is imported as geometry into the ANSYS transient structural and Fluent solvers. Constitutive equations for structure and fluid are integrated interactively in the time-domain, and structure displacement and fluid velocity and pressure are obtained iteratively. In each iteration, fluent transfers the fluid dynamic loads data to the transient structural solver at each pre-defined synchronization point and a

transient structural solver transfers the structure response data to the FLUENT solver for the next iteration. These iterations are repeated until a maximum number of stagger iterations is reached or until the data transferred between solvers and all field equations have converged [101]. Strain distribution from FSI are post processed for three different TVs and results for strain are employed for CA model.

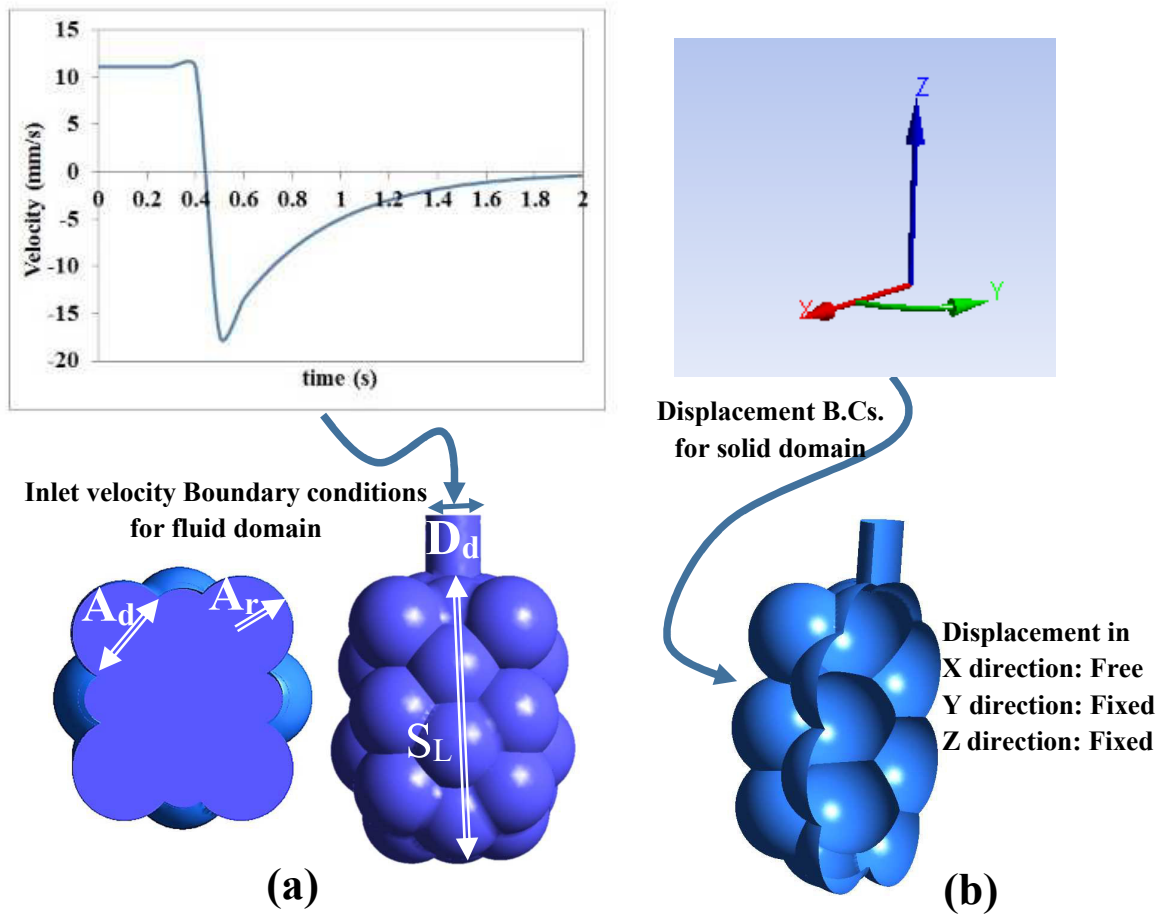


Figure 5.2: Alveolar sac model geometry and B.Cs in the current study. a) Fluid domain b) Cut view of solid domain with shell element.

Table 5.1: Alveolar Sac Model dimensions from the current study compared to morphometry reported in the literature

Parameters	Alveolar sac Model	Dimensions	References
	current study	Literature review	
Duct diameter Dd (mm)	0.19	0.25	Haefeli-Bleuer and Weibel [80]
Alveolus radius Ar (mm)	0.15	0.14	Weibel[81]
Alveolus depth D (mm)	0.2	0.23	Weibel [81]
Sac length SL (mm)	0.87	0.75	Haefeli-Bleuer and Weibel [80]
Number of alveoli	24	17	Weibel [81]

5.2.2 COMPUTATIONAL DOMAIN AND BOUNDARY CONDITIONS

A 3D model of alveolar sacs is built with realistic dimensions. Shell element is considered for the solid domain and space inside the alveolar region is devoted to the fluid domain. The finite element converged mesh consists of 91540 and 60195 tetrahedrons and triangles for the fluid and solid domains, respectively. Neo-Hookean hyperelastic material properties with incompressible air are assigned to the alveolar wall and flowing fluid. In addition, pulmonary alveoli are the terminal ends of the respiratory tree, which contain some collagen and elastic fibers. The elastic fibers allow the alveoli to undergoes strain as they are filled with air during inhalation. Then they spring back during exhalation in order to expel the carbon dioxide-rich

air. Therefore, boundary conditions for the solid domain are allocated as free displacements in the radial direction for the model and longitudinal and rotational displacement are fixed for the simulation (Figure 5.2-Table 5.1). Nonuniform inlet velocity boundary conditions for the fluid domain are defined in the form of constant and exponentially decreasing flow rate profiles for inhalation and exhalation during MV in the form of UDF files which are presented in Table 5.2.

Table 5.2: Inlet velocity waveform for MV

Inhalation/Exhalation	MV
$t \leq \text{Inhalation time } (t_{in})$ $(0 < t_{in} \leq 0.4s)$	$\frac{flowrate}{S*2^{g-1}}$
$t > \text{Exhalation time } (t_{ex})$ $(0.4s < t_{in} \leq 2s)$	$\frac{-flowrate \times \exp(-\frac{t_{in}+t_{ex}}{t_{in}})}{S*2^{g-1}}$

where S is equal to the alveolar duct cross section, g is equal to the generation number which is equal to 23 in this study and flow rate is equal to the proportion of TV (lung volume that represents the normal volume of air displaced between inhalation and exhalation when extra effort is not applied) to the inhalation time. Three different values for TV (200 mL, 500 mL and 1000 mL) are considered in the inlet velocity relationship to investigate their effects on increasing or reducing the damage in alveolar tissues under MV condition.

GOVERNING EQUATIONS FOR FLUID

Since Reynolds numbers in the pulmonary sacs are generally sufficiently small [123, 124], a 3D incompressible laminar Navier-Stokes and continuity equations in a 3D mesh domain with a control volume approximation [84] are solved numerically to give the velocity field within the alveolar region:

$$\nabla \cdot u = 0 \quad (5.1)$$

$$\rho_f \left(\frac{\partial u}{\partial t} + u \cdot \nabla \cdot u \right) = -\nabla p + \mu \nabla^2 u \quad (5.2)$$

where u is the velocity field, ρ_f is fluid density equal to $1.225 \frac{kg}{m^3}$, p is the pressure, and μ is the dynamic viscosity. The continuity equation represents the conservation of mass, Eq.5.1, and the Navier-Stokes equations represent the conservation of momentum, Eq. 5.2, that would be solved numerically on a moving grid using a commercial finite-volume based program with fully implicit time marching techniques under isothermal conditions in ANSYS fluent solver [100].

GOVERNING EQUATIONS FOR STRUCTURE

The governing equations for the movement of the alveolar sac walls during inhalation and exhalation are the time-dependent structural equations shown below:

$$\frac{\partial \sigma_{ij}}{\partial x_j} + F_i = \rho_s \frac{\partial^2 u_i}{\partial t^2} \quad (5.3)$$

$$\sigma_{ij} = E_{ijkl} \epsilon_{kl} \quad (5.4)$$

In the equations above σ is the stress in each direction, F is the body force, ρ_s is the density of tissue, u is the displacement, E is the elasticity tensor, and ϵ is the strain in each direction. Hyperelastic Neo-Hookean material parameters have been assigned to alveolar wall materials. Neo-Hookean hyperelastic materials have evolving nonlinear material properties and often used in large displacement applications [125,126]. Neo-Hookean model with free energy density are adopted for FSI simulation in this study:

$$W = \frac{G}{2} (\bar{I}_1 - 3) + K_m (J - 1)^2 \quad (5.5)$$

where $J = \det(\mathbf{F})$ and $\bar{I}_1 = J^{-\frac{2}{3}} I_1$. I_1 is the first invariant of the left Cauchy-Green Tensor $\mathbf{C} = \mathbf{F}^T \mathbf{F}$ is the deformation gradient. G and K_m are the shear and bulk moduli, respectively. For this study $G = 2000(Pa)$ and $K_m = 13.5(kPa)$ are considered for Neo-Hookean parameters [126,127]. Also alveolar density is appointed as $196(\frac{kg}{m^3})$ [128].

5.2.3 COUPLING FLUID-SOLID INTERACTIONS

For each time step during FSI, initially Equations. (5.1,5.2) are solved and applied forces on the alveolar wall are calculated. Next, constitutive equations for solid are employed to obtain alveolar wall displacement. Then, the generated mesh is updated with the diffusion-based smoothing method in dynamic mesh in Fluent, based on the response of the structure. Interactions between solid and fluid are restated iteratively for optimization. Next, post processed results from FSI are used to investigate population dynamics of cells constituent of tissue under MV with different TVs in the cellular level model.

5.3 CELLULAR AUTOMATA

CA is a discrete and rule-based model that has been used for both physics and biological modeling. A well-known compilation of CA-oriented physical model is a work by Chopard and Droz [129]. They covered common physical model such as fluid flow, elastic solid, diffusion and reaction-diffusion. Ermentrout et al [130], compiled various CA model in biology. This works covered CA model built to give pattern commonly found in biological system. The models built based on description of the components and interactions in associated biological system. Recent application of CA includes cancer spread modeling [131], disease infection [132] and inflammation [37, 133, 134]. These models consist of several agents that interacts to give rise to the dynamics of the environment. Reynolds et al [133], defined several agents in the model that represent epithelium and macrophages with finite states. These agents change states according to environmental interactions. Other studies would provide further information on possible agents definition on CA model [37, 134]. A CA model typically consists of a set of uniform cells (or agents), space represented by grids, and rules that define the cells behavior. The cells can be seen as mini-computer that computes the rules. Mathematically, a CA is defined in terms of set theory as a tuple:

$$A = \{G, E, U, f\} \tag{5.6}$$

where G, E, U and f are a grid of cells, set of finite states of cells, set of neighborhood and set of local rule, respectively. The grid is typically defined as d -dimensional square grid, that is $G = Z^d$. The state is typically defined as a finite set of numbers (e.g. binary, real). There is various definition of neighborhood, one of the most used is Moores neighborhood, defined as $U(x_i) = \{x | \|x_i - x\|_\infty \leq 1\}$. The local rule defines the evolution of state. The general form of rule is,

$$z^{t+1}(x) = f(z^t|_{U(x)}) \quad (5.7)$$

where $z^t(x)$ is state at x at time step t , and $z^t|_{U(x)}$ is state at the neighborhood of x . Finally, there needs to be a map from grid to states before applying the rules, that is $z : G \Rightarrow E$. One of the most common forms of local rules in CA is employing conditionals, which can also be represented as step function,

$$z^t = \begin{cases} 1 & \text{if } (A) \\ 0, & \text{else} \end{cases} \quad (5.8)$$

where A is conditional statement(s). The conditional statements typically involve the states of neighbors. Other recurring local rule is the summation of states,

$$z^{t+1}(x) = f(z^t|_{U(x)}) \quad (5.9)$$

Throughout this study, these two general forms of rule are used which are discussed in results and discussion section. The boundary of CA grid can be defined by two conditions: fixed or periodic. Fixed boundary condition imposes a constant value on the boundary. Periodic boundary lends itself from molecular modeling, and is used to approach large domain. It imposes continuum between two opposite facing boundaries. This condition can also be seen as a domain which satisfies torus topology.

5.3.1 INFLAMMATION MODEL

As it was discussed, inflammation is a complex process that involves the release and spread of cytokines and cells interaction with the environment. That is to say, inflammation is mainly the interplay between reaction-diffusion (R/D) of cytokines and cells response. To model this process, a discrete computational method based on cellular automata (CA) is employed [117]. The CA has been successfully applied to model behavior biological system [135], including reaction diffusion and cells response and arrangement to environment, inflammation [119, 136, 137] and cancer modeling [118]. The discrete model employed in this study is largely based on probability. As usual, the CA model is built upon a definition of the grid. In this study, a square two-dimensional grid is used. The grid consists of several layers, as can be found in R/D modeling. There are four layers of grid: epithelial cells, immune cells (cells with motility), cytokines, proteins and elastic field grid. As per CA modeling, the evolution of the grids is dictated by a set of rules. The rules and grids are explained below. Figure 5.3 illustrates the CA model with multiple grids, as well as a graph showing the causal path of the CA model.

5.3.2 EPITHELIAL CELLS GRID

The epithelial cells grid is a typical CA grid, with only two states: 1 and 0, representing dead and healthy, respectively. The rule that defines evolution of the CA cells in this grid is,

$$z_1^{t+1}(x) = \begin{cases} 1, \text{rand}(\alpha_1, \beta_1) < z_{3TNF}^t(x) \\ 0, \text{otherwise, or healing} \end{cases} \quad (5.10)$$

$$z_1^{t+1}(x) = \text{samp}(d, w) \quad (5.11)$$

where $z_1^t(x)$ is the epithelial cells state at time step t and location x , $z_{3TNF}^t(x)$ is concentration of pro-inflammatory cytokine (explained later) occupying the same grid coordinate, rand is random number generator based on beta function probability density, α_1 and β_1 are two beta function parameters, and $\text{samp}(w, d)$ is random sampling algorithm that samples data set d by weights w . Equation (5.10) describes the state transition by cytokine (TNF) and

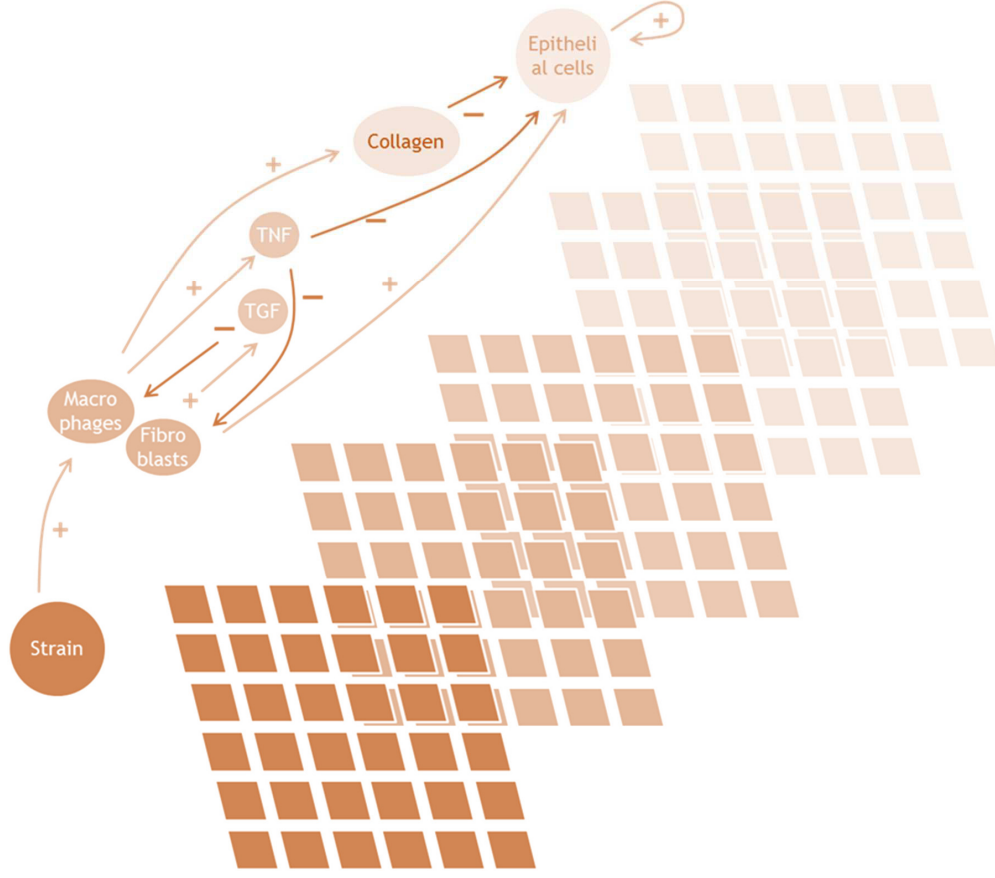


Figure 5.3: CA with multiple grids, each grid represents the event and dynamics in the tissue. The graph on the left shows the causal path of the events. Each edge associated with plus (+) sign represent positive feedback to the vertex it is pointing on (activation, release/adding concentration, healing), while the one associated with negative sign (-) carries negative feedback (inhibition, damage).

fibroblast (healing). The healing condition comes from cell mitosis and fibroblast, and is described by Equation (5.12) and (5.13) below.

$$unirand < P_{mt} \quad (5.12)$$

$$z_1^{t+t_h}(x) = 1 \quad \text{when} \quad z_{2f}^t(x) = 2 \quad (5.13)$$

where unirand is uniform random number generator between 0 and 1, P_{mt} is mitosis rate, and z_{2f}^t is the state of immune cells grid. The mitosis rate defines the probabilistic rate of

mitosis, as part of self-healing process of the cells. Equation (5.11) describes state transition influenced by scarring (explained in Section 5.3.6). Function `samp` randomly chooses the state of a cell, d , with some bias w . In this case, d is the possible state the grid can have (i.e. 0 and 1). The weight w skews `samp` to choose state 1 according to the numbers of collagen deposits) at vicinity. If Moore's neighborhood is used, then maximum number of collagen deposits is 9.

Table 5.3: Beta Function Parameters

Subscript number	Case	α	β
1	Epithelial cells grid (Eq. 5.6)	5	1
2	Macrophages activation (Eq. 5.11)	5	1
3	TNF Release (Eq. 5.13)	1	3
4	TGF Release (Eq. 5.14)	2	1

Table 5.4: CA parameters for simulation in this paper

Mitosis probability, P_{mt}	1/5
Healing time	5
Collagen time, K_c	10
Collagen dissolution	10 % /tick
TNF diffusivity, D_{TNF}	0.07
TGF diffusivity, D_{TGF}	0.1
TNF dissolution constant, K_{TNF}	1E-3
TGF dissolution constant, K_{TGF}	1E-5
Repopulation of immune cells, ϵ_{pop}	5 ticks
Immune cells life time	20 ticks
Immune cells speed	3 cells/ tick
Population of immune cells, n_{im}	25

5.3.3 IMMUNE CELLS

The immune cells move according to the concentration gradient (chemotaxis). The grids can contain three states: 0, 1, and 2, representing non-existence of cells, inactivated, activated and secondary state for the immune cells. A simple probabilistic model of cell motility is used here, i.e.

$$a_2 = \text{samp}(U(x), z_3^t(x)) \quad (5.14)$$

$$z_2^{t+1}(x) \big|_{U(x)} = \begin{cases} 1, & \text{at } z_2^t(a_2) \\ 0, & \text{otherwise} \end{cases} \quad (5.15)$$

where $\text{samp}(w,d)$ has been used once again, with different terms regarding w and d . In this case, samp randomly choose local grid site according to neighborhood $U(x)$, and the choice is biased according to z_3^t , which is the state of cytokine grid at current cell location, x . Variables in equation (5.14) is as follow: $U(x)$ is Moores neighborhood function, $z_2^t(x)$ is the state of immune cells grid at time step t . There are two type of immune cells, the macrophages (agent of inflammation) and fibroblasts (agent of healing). The state transition of the grid is applied toward grid with state $z_2^t(x) > 0$ (the grid occupied by immune cells), and governed by rule as follows,

$$z_{2m}^{t+1}(x) = \begin{cases} 1, & t_{top} > \epsilon_{pop} \\ 2, & z_1^t = 1(\text{fibroblast}), \text{rand}(\alpha_2, \beta_2) < z_4^t(x)(\text{macrophage}) \\ 0, & \text{otherwise or if } t_{im} > \epsilon_{im} \end{cases} \quad (5.16)$$

where ϵ_{im} is the age of immune cells, $z_4^t(x)$ is the state of elastic field grid (which will be explained later) and the random number generation using beta function probability density has been used once again. Equation (5.15) is applied to both type of immune cells, with minor differences in details (including the rule for activation) as shown in Equation (5.16). The macrophages are still mobile after activation, while fibroblast will stay at the last grid site after activation. The latter represent fibroblast differentiating at injured site. This means the rule in Equation (5.14) and (5.15) still applies to macrophages after activation, but not fibroblasts. In addition, the ϵ_{im} of fibroblast also reduced by 75% after activation.

When activated, the immune cells release cytokines. Each type of immune cell is associated with a specific cytokine (i.e. macrophage releases TNF, and fibroblast releases TGF). Macrophage tends to release TNF where the environment experiences more strain, while fibroblast tends to release TGF in the presence of TNF. However, TGF inhibits macrophage

in releasing TNF. Hence, the CA reflects the activator-inhibitor system. The cytokines release by immune cells can generally be expressed as,

$$z_{3TNF}^{t+1}(x) = \begin{cases} 1, \text{rand}(\alpha_3, \beta_3) \geq z_{3TGF}^t(x) & \text{when } z_{2m}^t(x) = 2 \\ 0, \text{otherwise} \end{cases} \quad (5.17)$$

$$z_{3TGF}^{t+1}(x) = \begin{cases} 1, \text{rand}(\alpha_4, \beta_4) \leq z_{3TNF}^t(x) & \text{when } z_{2f}^t(x) = 1 \\ 0, \text{otherwise} \end{cases} \quad (5.18)$$

where $z_3^t(x)$ is the state of cytokine grid at time t, the subscript denotes the type of cytokine, $z_2^t(x)$ is the state of immune cell grid at the same time step, and subscript m and f denote the type of immune cell (macrophage and fibroblast), consecutively, α and β are beta function parameters which are given in Table 5.3. The population of immune cells are also kept at averagely n_{im} numbers, with 0.25 variance. This means the first condition in equation (5.15) applies at random grid location to ensure the population is at n_{im} on average. As before, the beta function and rules parameters are given in Table 5.3 and 5.4.

5.3.4 CYTOKINE GRID

The cytokine grid contains an array of CA cells to simulate the spread of cytokines by diffusion, and its disintegration over time. One way to simulate spread is to employ an additive rule such as,

$$z_3^{t+1}(x) = \Sigma_{U(x)} k_i z_3^t(x) \quad (5.19)$$

where k_i is a set of constant corresponding to neighborhood function, $U(x)$. To determine k_i , one may gain insights from a system appearing as a numerical solution of diffusion equations with additional disintegration terms,

$$\dot{C} = D\nabla^2 C - K.C \quad (5.20)$$

where C is concentration, D is diffusivity, K is a constant determining the rate of disintegration. Numerical solution by Finite Difference Method gives,

$$z_3^{t+1}(x) = z_3^t(x) + D\Sigma_{U(x)} k_i z_3^t(x) - K z_3^t(x) \quad (5.21)$$

where Neumanns neighborhood is used, and cells have continuous state, and $k_i = 1 - 4D$ for $U(x) = 0$, and $k_i = D$ otherwise. As before, D and K are shown in Table 5.4.

5.3.5 ELASTIC FIELD GRID

It is theorized that mechanical strain on tissue activates ion channel(s) on the cells that leads to the release of an array of cytokines [138]. In this model, the mechanical strain is represented by another layer of CA grid as a discretized strain field. The FEM simulation in the study provides insights into the strain distribution. This is translated into the discretized distribution of strain fields in the CA grid. This strain field acts as an energy gradient in activating the immune cells. The model simplifies the activation process by ignoring the molecular mechanism of ion channels opening by strain and cell signaling pathways that lead to the release of specific cytokines. In addition, only the macrophage is activated by strain. The rule dictating macrophage activation is expressed in equation(5.16).

5.3.6 SCARRING

The healing by fibroblasts release TGF that contributes to production of collagen. Hence, there is a surge of collagen concentration as a result of healing by fibroblasts. This introduces scar to the tissue, and reduce tissue compliance. In the present study, we represent this phenomenology where collagen deposits after healing add risks to damage on epithelial cells. In CA, the site of these collagen deposits are the same as the location of fibroblast after activation. The effect of these collagen deposits will stay after specified time, as shown Table 5.2 as collagen time. The rule of collagen deposits is as follow,

$$z_5^{t+t_h}(x) = \begin{cases} 1, & \text{at } z_{2f}^t(x) = 2 \\ 0, & \text{otherwise} \end{cases} \quad (5.22)$$

CA rules were implemented in Matlab R2016. The statistical toolbox was used for random algorithms, rand and samp. The samp is basically a randomized data sampling algorithm, and Matlab R2016 uses the algorithm provided by Wong and Easton [139].The simulation

is run for a domain representing tissue experiencing mechanical strain, expressed in elastic field grid of CA. The grids contain 100 by 100 cells, where a biological epithelial cell size is around $1\mu m$. The boundary condition used is periodic boundary condition, where continuum between two opposite edge of the boundary is imposed as,

$$Z^t|_{\Gamma_1(x)} = Z^t|_{\Gamma_2(x)} \quad (5.23)$$

where Γ_1 and Γ_2 are set of two opposing boundaries.

5.4 RESULTS AND DISCUSSION

FSI is conducted on a 3D model of alveolar sac and three different values of TV (TV=200, 500 and 1000 mL). Strain distributions are post processed to investigate regions with highest concentration of strain. Next, strain versus time curves in different locations of the model are post processed to evaluate effect of tidal volume on strain level changes during the breathing cycle. Then, maximum strain values from FSI are employed in the CA model. The CA model is implemented using MATLAB R2016A and three commonly found strain distributions (uniform, middle trough and sinusoidal bumps strain distributions) are taken into consideration to explore the influence of different TVs in mechanical ventilation on cell population dynamics.

5.4.1 STRAIN DISTRIBUTION

Strain distributions are presented in Figure 5.4 for different tidal volume values. As can be seen, higher strain is observed at the inlet area and increasing tidal volume leads to higher strain levels in the alveolar model. Initially, the alveolar model shows a slight contraction but the alveolar duct shows an expansion to let air enter into the alveolar region. Then, at the end of inspiration time, the alveolar volume will be filled with air and this process would again happen in the reverse direction, inlet duct contracts while alveolar region is expanding until air leaves the alveolar region and then the alveolar would return back to

the non-deformed shape. This procedure is regarded as non-uniform deformation of alveolar wall [128].

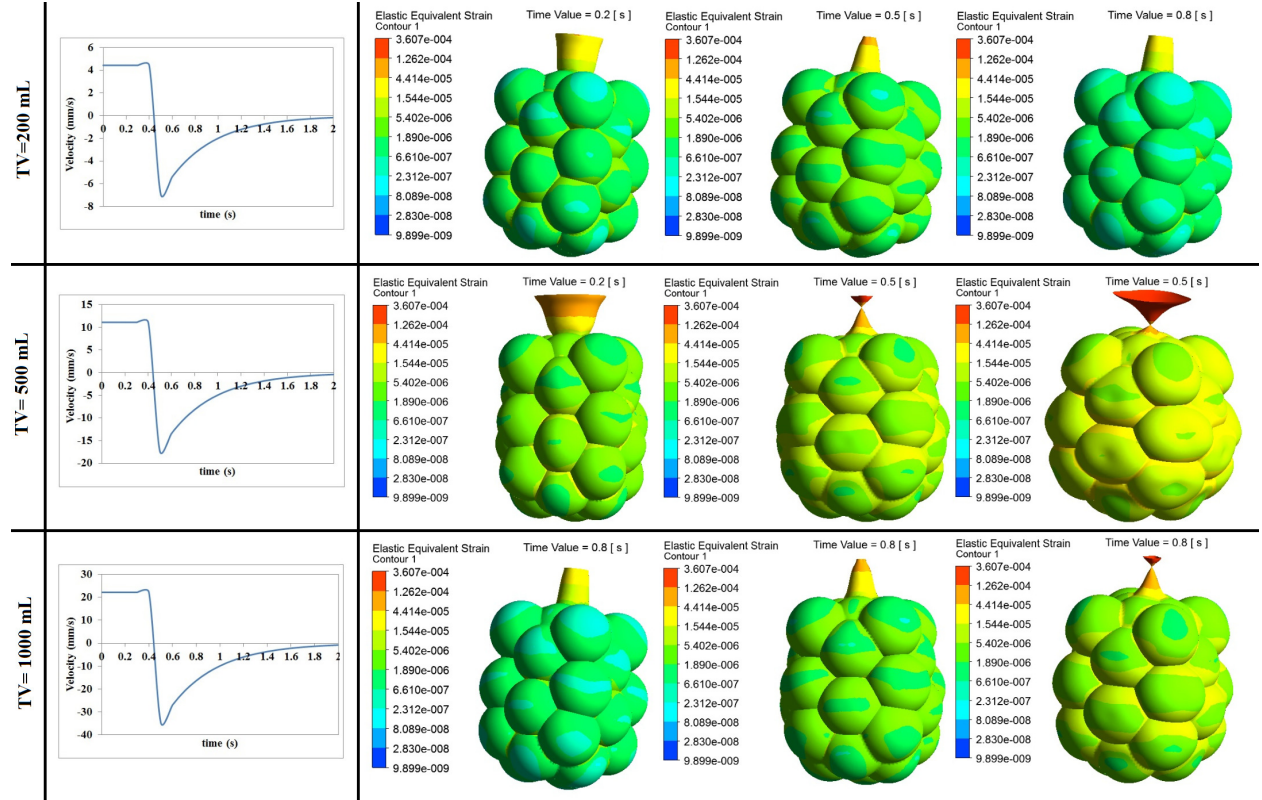


Figure 5.4: Strain distribution at inhalation ($t=0.2$ s) and exhalation time ($t=0.5, 0.8$ and 2 s) for $TV= 200, 500$ and 1000 mL.

Three different types of strain distribution in alveolar region. As can be observed, strain in the center of alveoli is distributed uniformly but in each alveolus, it is concentrated in the connection of the alveolus to the neighbor alveoli, as compared to the center of the alveolus itself which is termed middle through strain distribution in this study. In addition, another strain distribution, defined as sinusoidal bumps, is distinguished on the connection edge of the alveoli where it is approximately distributed in symmetric form with a higher strain distribution. These three types of strain distributions are presented in Figure 5.5.

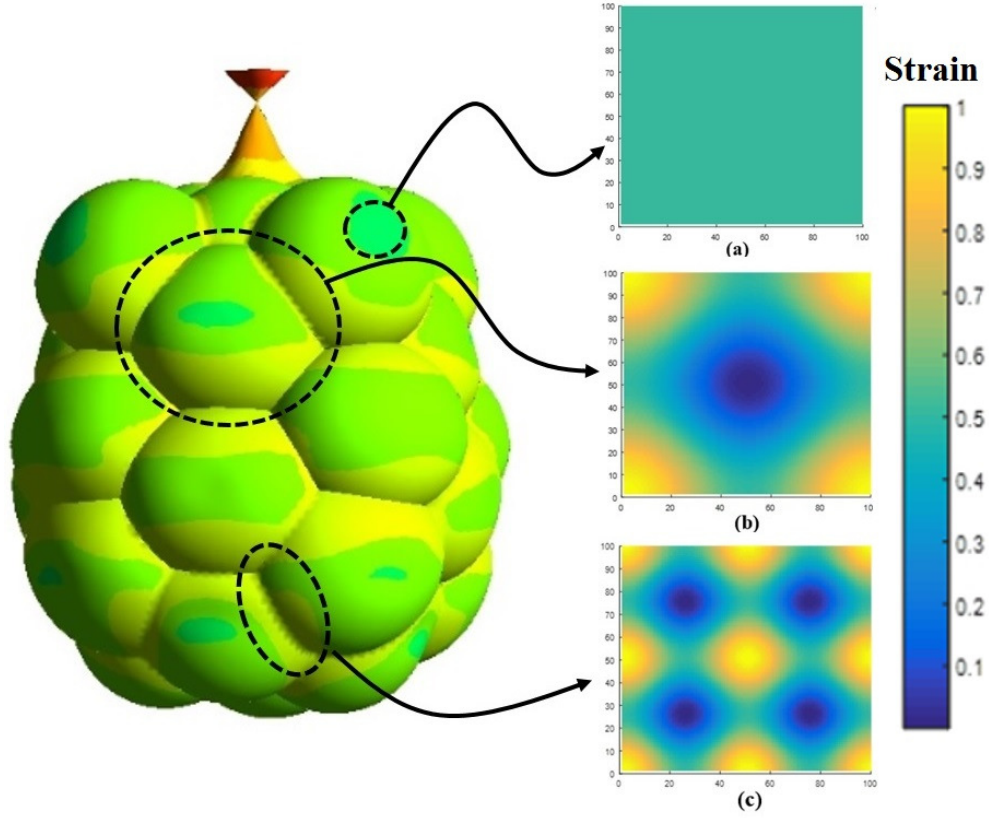


Figure 5.5: Typical distribution of strain. The color bar on the right shows the magnitude correspond to the color plot. (a) Uniform, (b) middle trough, (c) sinusoidal bumps.

5.4.2 STRAIN LEVEL AT VARIOUS REGIONS IN ALVEOLAR SACS

Strain versus time curves for different TVs are plotted at different locations in alveolar region and as it is illustrated in Figure 5.6, max equivalent elastic strain value for tidal volume equal 500 mL is approximately 2 times bigger than strain value for 200 mL and 2 times smaller than strain value for 1000 mL. Also, it can be seen that middle layers in alveolar region represent higher strain level in comparison to upper and lower layers.

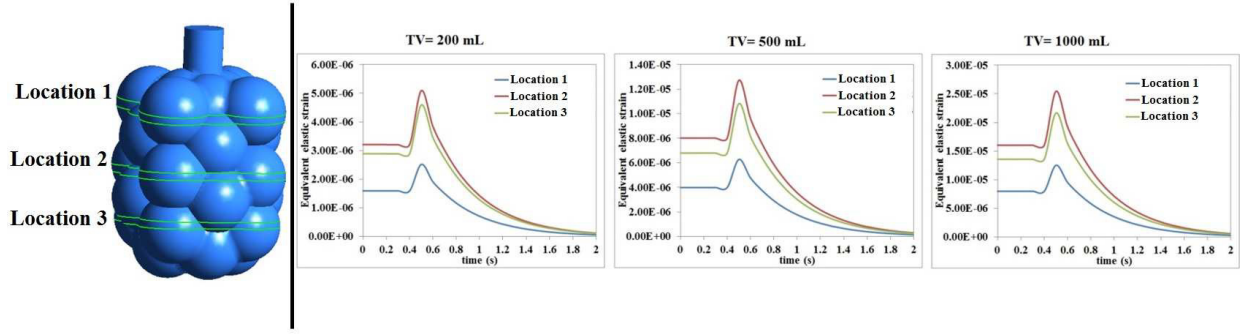


Figure 5.6: Strain level alternation from location 1 to location 3 for different TVs.

5.4.3 SENSITIVITY ANALYSIS

Sensitivity of strain level to changes in alveolar tissue's mechanical properties and wall thickness is examined. For this aim, shear and bulk modulus values are altered by 10% and 25% (reduction and increase compare to initial values). Sensitivity analyses is also conducted by reconstructing 10 times thicker and thinner alveolar wall thickness compare to initial model. As it was discussed earlier, middle layer would sustain higher strain level in alveolar model. Therefore, FSI results for different case studies for morphological changes with TV=500 are compared at middle layer within alveolar model. Results presented that decreasing shear and bulk modulus would lead to higher strain level within the alveolar model and in contrast, increasing discussed parameters reduce strain level in the model. It is observed that increasing and decreasing by 10% and 25% would correspondingly lead to 10 and 30 percent change in strain level and 10 times increased and decreased alveolar wall thickness would subsequently increase and reduce strain level by almost 10 times. Strain distributions, by contrast, are same for all case studies. In following results from FSI are imported in CA model.

5.4.4 STRAIN-INDUCED INFLAMMATION SIMULATION

The developed CA model was used to study the effect of different tidal volumes in mechanical ventilation on the cell population dynamics. Based on FSI analysis at the alveolar region, three commonly found strain distributions are taken into consideration for the cell population dynamics as shown in Figure 5.5. Since we are interested in the percentage of parametric change, the simulation is carried out with normalized variables. Hence, the magnitude of strain is normalized with respect to the highest value of the three schemes as shown in Table 5.5. In addition, the time scale of cell population dynamics is remarkably higher than typically found in breathing cycle. Hence the justification is made for taking the amplitude of strain during the breathing cycle for this CA model.

Table 5.5: Three schemes for CA simulation of cell population dynamics

TV (ml)	Real Value	Normalization
200	2.4E-05	0.21
500	5.99E-05	0.52
1000	1.15E-04	1.00

CASE STUDY I (UNIFORM STRAIN)

FSI results suggest the cell population in the tissue experience some uniform level of strain. The amplitudes of strain as shown in Table 5.5 were applied for the three strain distributions. Figure 5.7 shows numbers of dead epithelial cells and collagen deposited according to different level of strain. The numbers of dead epithelial cells can be seen as a measure of damage done in epithelium. Figure 5.7 also shows different trend of damage occurring on the tissue. Figure 5.7(a) shows a spike that last until approximately 600 simulation time, followed by smaller spike of damage. In Figure 5.7(b), the damage increased rapidly and the increasing trend stopped at approximately 100 simulation time. In Figure 5.7(c), the damage keeps increasing

until 1000 simulation time. Notice that the CA grid has 10,000 cells in total, but the damage in case of Figure 5.7(c) did not spread to the whole grid. The numbers of collagen deposits follow the trend of epithelium damage in Figure 5.7(a) and (b). However, in the case of Figure 5.7(c), the numbers of collagen deposits increase and tend to slow down at approximately 600 simulation time.

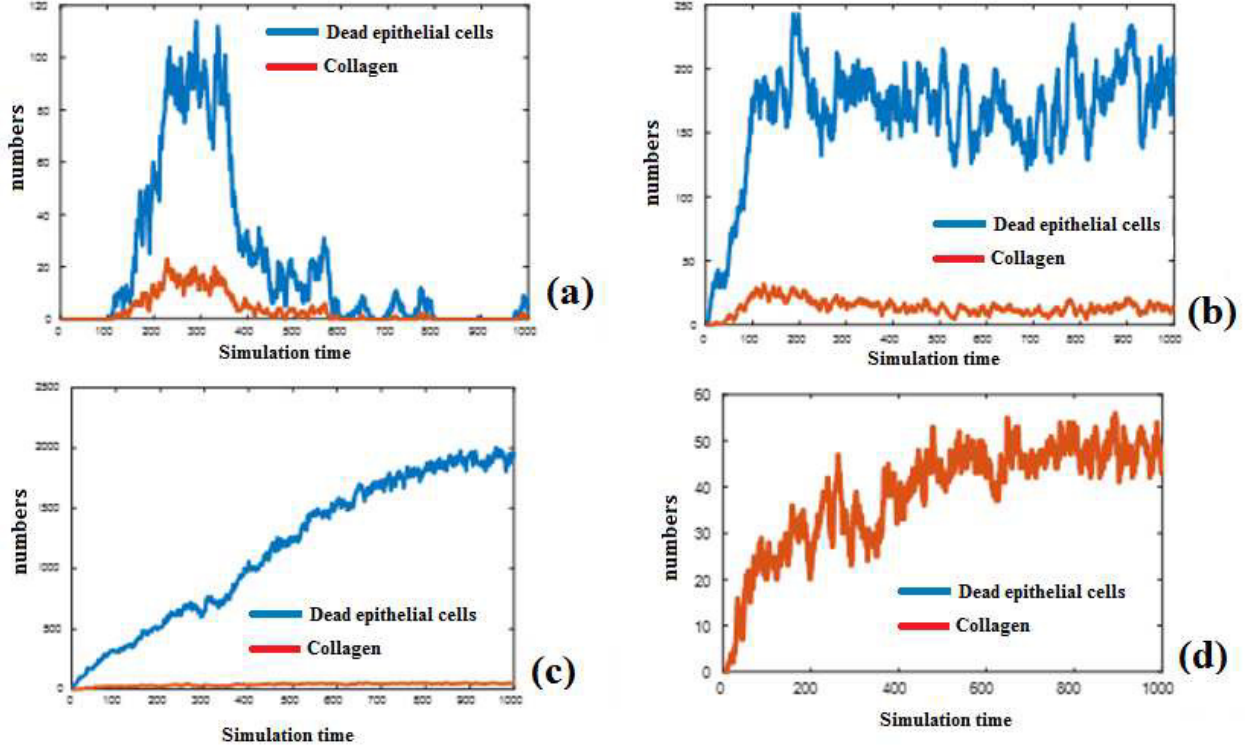


Figure 5.7: Cell population dynamics corresponding to case study *I*; numbers of dead epithelial cells on, (a) norm. strain=0.21, (b) norm. strain=0.52, (c) norm. strain=1, and (d) numbers of collagen deposits.

Figures 5.8(a) and (b) show the spatial distribution of epithelium damage for the case shown in Figure 5.7(a) at 300 and 550 simulation times, respectively. The damage in Figure 5.8(a) corresponds to the spike damage in Figure 5.7(a), and it shows that the damage appeared in random locations as three patches on the tissue represented by CA grid. After 550 simulation time, the patches of damage reduced into only one of the previous three patches. Figure 5.8(c) shows the distribution of fibroblasts (yellow dots) and collagen deposits (dark dots). The fibroblasts are clearly distributed around the damage patches. Figure 5.8(d) show

the comparison of the peak damage occurring for the three strain magnitudes considered in this study. The increase in the peaks shows the exponential rise in damaged cells as the strain was increased.

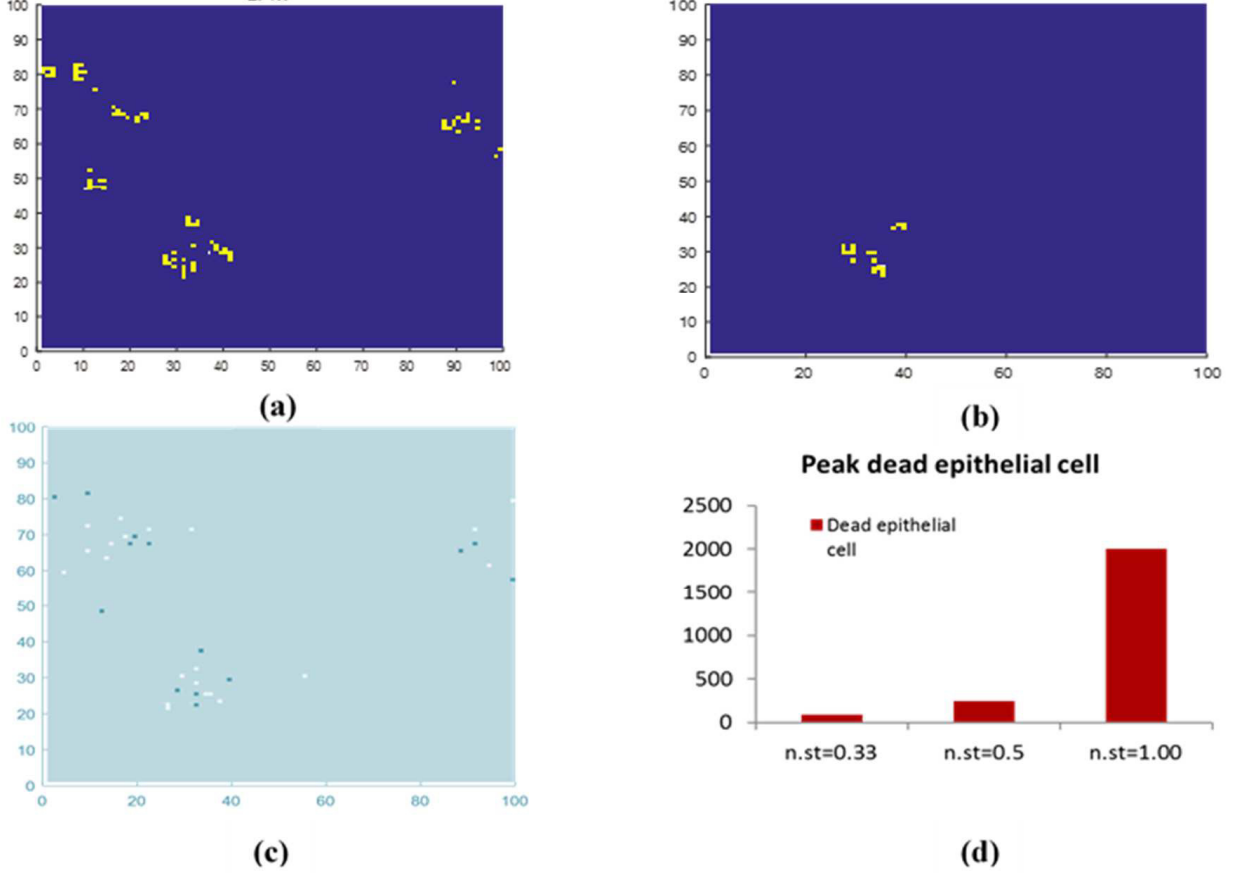


Figure 5.8: a. Epithelial cells damaged after 300 simulation times, yellow-colored grid denotes the portion of tissue with dead epithelial cells, b. Epithelial cells damaged after 550 simulation times, c. Fibroblasts (white dots) and collagen deposits (dark dots), d. Peak damage to epithelium.

Figure 5.9 shows the snapshots of damage distribution for the case illustrated in Figure 5.7(b). The damage in this case tended to be steady after approximately 100 simulation times. In Figure 5.8(a), the damage appeared at random locations as patches with an intact tissue after 180 simulation times. After 900 simulation times the patches shrank, but the damage was distributed more spatially with smaller patches. However, as can be seen in Figure 5.7(b), the damage seems to be steady.

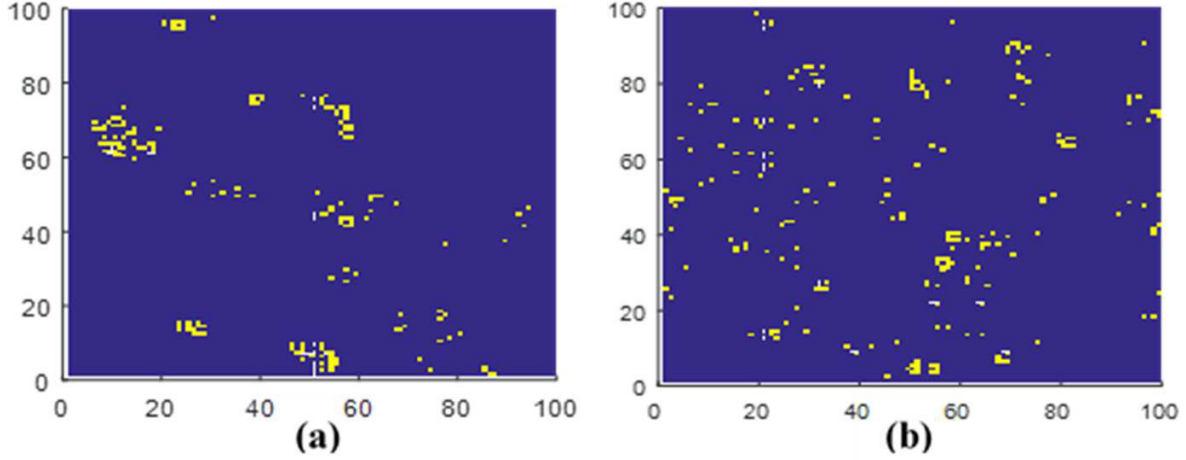


Figure 5.9: Snapshots of case with norm strain=0.52, (a) Epithelial cells damages after 180 simulation time, yellow-colored grid denotes the portion of tissue with dead epithelial cells, (b) Epithelial cells damages after 900 simulation time.

CASE STUDY II (MIDDLE TROUGH)

In this case, the peak strain surrounds an area of low strain. Figure 5.10 shows the dynamics of cell population under different strain amplitudes, which are the same as described in a previous section. Figure 5.10(a) shows two clear spikes of epithelium damage during the simulation time. Figure 5.10(b) shows peak damage that lasted longer than the previous one; this one is similar to the case in Figure 5.7(a). The case in Figure 5.10(c) shows the tendency of constant increase in damage over time. As before, the collagen deposits in Figure 5.10(b) showed a similar trend to epithelium damage. However, there is no collagen deposit in Figure 5.10(a), and collagen deposits in the last case as shown in Figure 5.10(c) decreased and showed a tendency to stabilize after approximately 600 simulation times, despite the increasing damage to the epithelium.

Figures 5.11(a) and (b) shows spatial distributions of epithelium damage of the case shown in Figure 5.10(a). Figure 5.11(a) corresponds to the first spike in Figure 5.10(a) at 67 simulation time, and Figure 5.11(b) corresponds to the second spike at 444 simulation

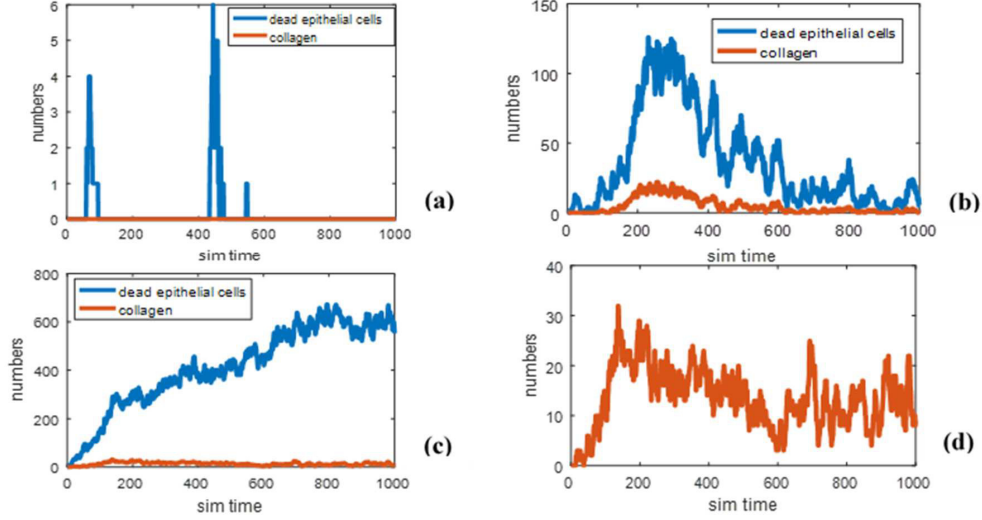


Figure 5.10: Cell population dynamics corresponding to case study *II* ; Numbers of dead epithelial cells on, (a) norm. strain=0.21, (b) norm. strain=0.52, (c) norm. strain=1, and (d) numbers of collagen deposits.

times. There is only one patch of damage with minimum numbers of dead cells. The spikes in Figure 5.10(a) apparently correspond to two different locations of patches of damage. The location of patches, as should be expected, tend to appear in regions close the amplitude of strain. Figure 5.11(c) shows fibroblasts distribution corresponding to the case shown in Figure 5.10(a) at 67 simulation times (coinciding with the first spike). As can be seen, the fibroblasts are not concentrated in one place, and are spread out on the whole CA grid. Figure 5.11(d) shows the peak damage in the epithelium, as well as the exponential rise in damage as strain increased, similar to the previous case of uniform strain.

CASE STUDY III (SINUSOIDAL BUMPS)

Figure 5.12 shows epithelium cells population dynamics under the strain distribution as shown in Figure 5.5(c). As shown in Figure 5.12(a), there is clearly no damage to the epithelium, despite some degree of damage that occurred in the previous case with the same strain amplitude. In Figure 5.12(b), we can see that the the damage increased rapidly after 200

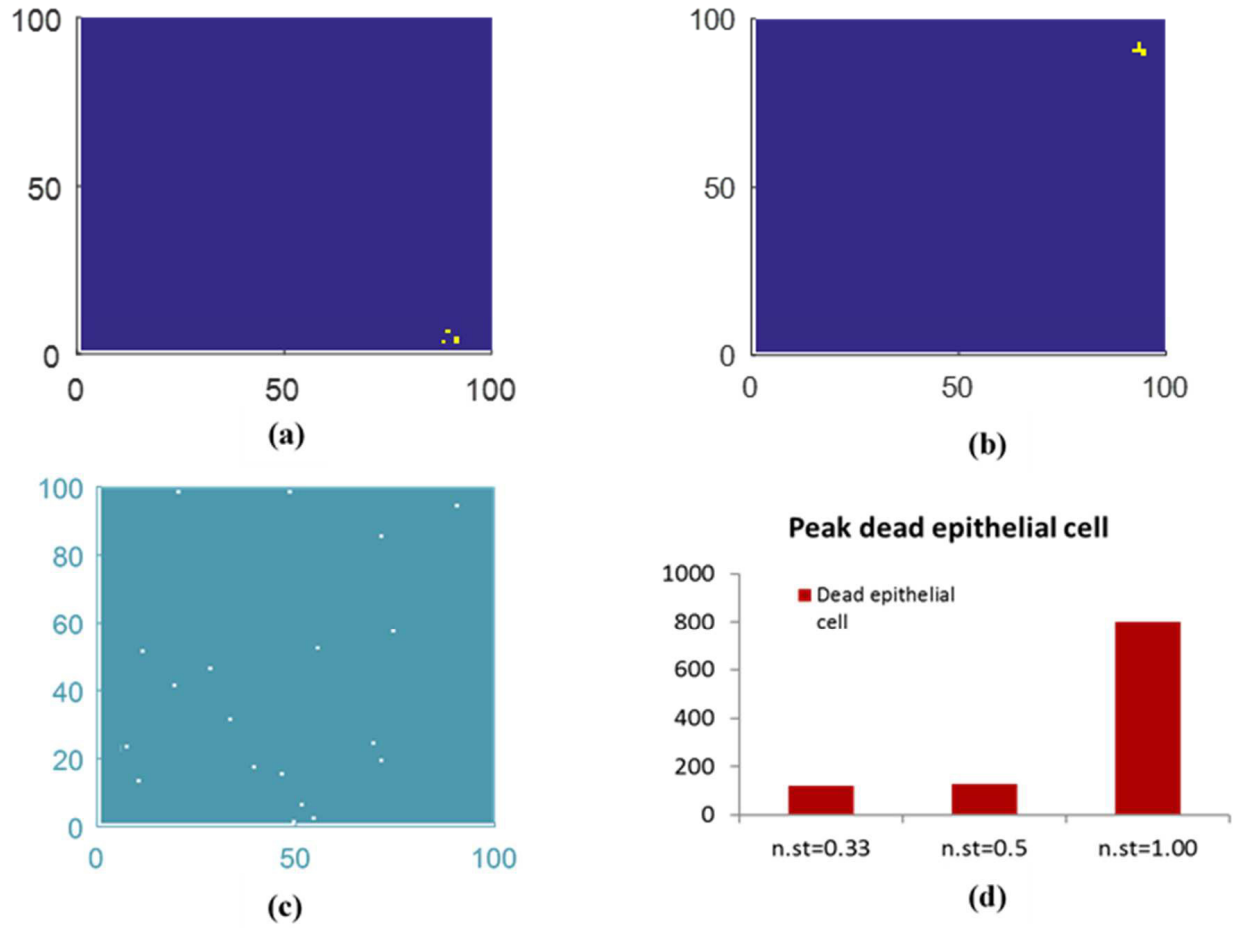


Figure 5.11: (a) Epithelial cells damaged after 67 simulation times, yellow-colored grid denotes the portion of tissue with dead epithelial cells, (b) Epithelial cells damaged after 444 simulation times, (c) Fibroblasts (white dots), (d) peak damage to epithelium.

simulation times, but decreased after a short period of time. However, the damage did not vanish completely and some level of damage remained until the end of simulation time. Figure 5.12(c) shows population dynamics under the highest strain amplitude. The damage increased since the epithelium is subjected to the strain, and stabilized after approximately 500 simulation times. Figure 5.12(d) shows peak damage for this case, and it showed a similar exponential tendency as discussed in the previous two cases.

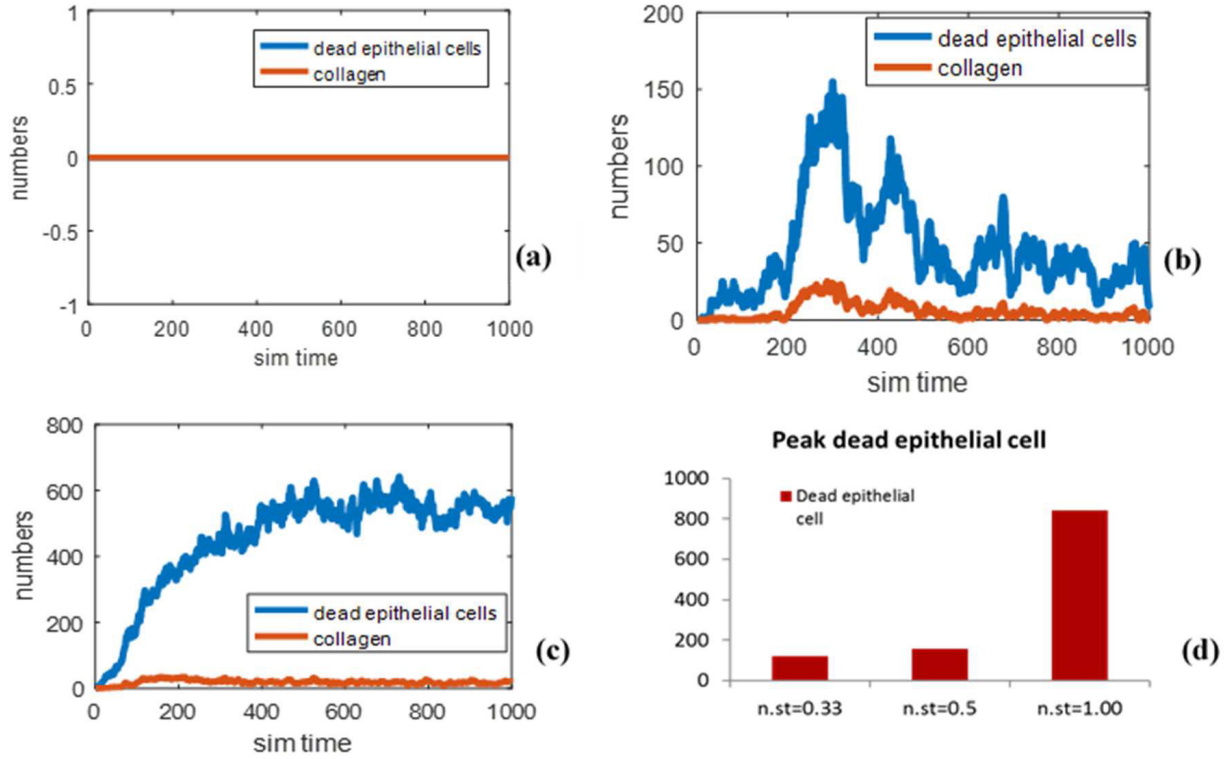


Figure 5.12: Cell population dynamics corresponding to case study *III* ;Numbers of dead epithelial cells on, (a) norm. strain=0.21, (b) norm. strain=0.52, (c) norm. strain=1, and (d) Peak damage to epithelium.

5.5 DISCUSSION

FSI analysis is conducted on a symmetrical alveolar sac model for three different tidal volume values. Strain distributions in the alveolar region were analyzed and it was observed that the connection points of the alveoli undergo higher strain during the breathing cycle. While non-symmetric model would generate more variations of strain distribution that may present non-uniform distribution similar to the considered symmetric alveolar sac model in this study. Additionally, strain-time curves plotted for different tidal volumes at three different locations through the model showed that the middle layers would tolerate a higher level of strain in comparison to the upper and lower layers considered in the model. Sensitivity analysis shows

that strain level in alveolar region is highly sensitive to alveolar sacs morphological changes in pulmonary acinar region ,but it would not considerably change strain distribution. Three different strain distributions derived from post processed FSI results were implemented in the CA model to investigate influence of tidal volume and strain level on cell population dynamics under the MV condition. The first case considered in the CA model clearly depicts that while the strain is low enough, the tissue is still able to sustain healing capacity by mitosis and fibroblasts eventually mitigate the damage. Increasing the TV (and hence, increasing strain), leads to reduction of healing capacity. Generally, the tissue is able to mitigate damage, but some amount of damage still persists. Furthermore, the simulations show that the strain distributions significantly impact the population dynamics of epithelial cells. It is interesting to note that the epithelium under the same amplitude of strain demonstrates specific population dynamics. This may be caused by the chances of macrophages exposed to strains of the tissue. The initial locations of macrophages are initially determined by uniform RNG. Although the macrophages are initially randomly distributed on the grid (and expectedly statistically uniform as the result of uniform RNG), it can be said that the strain distributions pose less risk of initially triggering inflammation by macrophages (that is, the release of TNF). Increasing the strain amplitude will affect the chances of macrophages releasing TNF. The interplay between strain amplitude and distribution also influences the healing capacity of the tissue. The tissue and its constituents will still able to reduce or withhold damage when the strain amplitude is low enough. However, when the strain distribution lowers the chance of the macrophages being exposed to strain, the tissue is still able to stop the rate of damage, although not reduce it. Snapshots of the spatial distribution of damage on the epithelium provide more insights into the inflammation. Generally, damage appears randomly as patches and these patches are reduced in number gradually by the healing effect which is influenced by fibroblasts (along with mitosis). As soon as one or a few fibroblasts are found in the location of a damage patch, the cell signaling by TNF will attract more fibroblasts that wander randomly on the grid. This prevents the damage from spreading and

localizing. However, in the case of steady damage withholds, the damage at first appears as patches. Next, the patches are reduced by healing. However, more damage appears on different locations, leading to smaller and more distributed damage. In this case, the tissue constituents are not able to localize damages. Hence, the quantitative charts would not reveal the whole dynamics of the damage. Since, fibroblasts are cells with motility, and may not arrive at the damage locations, in the case which damage patch appeared after 67 simulation times in a region with higher strain amplitude. This patch quickly healed by mitosis as the fibroblasts which can be seen did not surround the location. After 444 simulation times, another spike appeared, corresponding to another patch that appeared in a different location. From these snapshots, it can be inferred that as long as the damage patches can be healed quickly, the tissue and its constituents will still be able to revert back to intact tissue. Peak damage (assumed as the number of dead cells) in all the three cases in this study showed an exponential rise as strain amplitude increased, despite strain distribution. As expected, the uniform strain distribution had the highest damage. Results from the other two strain distributions suggested that they led to similar amounts of peak damage. It is well known that tissue integrity is influenced by the population of the cells. The quantitative comparison of the number of dead cells presented in this study can be used as a justification for analysis at the organ level. For instance, based on the results from this study, one could suggest an exponential function to find the changes in mechanical properties of tissue as a result of increasing TV in MV. It is to be noted that the collagen parameters only contribute to damaging airway tissue. It is also implied that collagen accumulation may contribute to increased airway impedance [140], which can be reflected by alteration of airway tissue elasticity in the organ model. This will be included in future works. It must be acknowledged that the CA model presented needs experimental tuning, since it has only been compared qualitatively. However, the CA model has also been shown to address a variety of dynamic behavior, based on the abstraction of interaction of cells in tissue. Thus, the model has provided a framework

for experimental tuning and parametric matching tools for studying the complex dynamics of inflammation.

Table 5.6: Qualitative behavior of the alveolar tissue CA model when being subjected to strain at different level

Cases	Inflammation		
	Strain: 0.21	Strain: 0.52	Strain: 1.00
1: Uniform	Suppressed	Steady	Rising
2: Middle Trough	Spikes	Suppressed	Steady
3: Sinusoidal	Non-existent	Suppressed	Steady

5.6 CONCLUSION

In this study, FSI analysis was employed to study strain levels in the alveolar region. This was followed by implementation of a CA model for strain-induced inflammation. It was observed that strain is highly concentrated in the inlet area. In addition, strain versus time curves in different locations through the alveolar model showed that middle layers in the alveolar region underwent higher level of strain during breathing in the MV condition. Three different types of strain distributions in the alveolar region were analyzed; uniform, middle through and sinusoidal bumps. Since the time scale of deformation for the alveolar model is largely different from the deformation at the tissue level, the results from the alveolar model were abstracted into the CA model. This information was used to study population dynamics of cell constituents of tissue under MV for different strain levels associated with different

TVs: 200 ml, 500 ml and 1000 ml. The CA model results suggest that strain distribution plays a significant role in population dynamics. They also implied that interplay between strain magnitude and distribution determines healing effectiveness. Lastly, results suggest that increasing TV leads to an exponential rise in damage on tissue by inflammation.

CHAPTER 6

CONCLUSION AND FUTURE WORK

Respiratory disease and aging influence functionality and structural properties of human lung. Due to limitation of experimental tests, many studies employed computational techniques to investigate the influence of respiratory disease and aging on lung's functionality. Despite the existence of a large number of studies in this field, there are still uncertain understanding of their real effects. In addition, setting proper ventilation protocols is the great concern of respiratory specialists. This dissertation aims to present an integrated approach of computational modeling at different scales to investigate the influence of respiratory disease and aging on bronchial tree and optimize ventilation parameters to improve breathing condition specially for elder people.

In Chapter 2, the influence of respiratory disease (emphysema and ARDS) on mechanics of alveolar sacs was investigated. It was concluded that respiratory disease substantially affect alveolar sacs mechanics. Emphysema led to less air penetration into the acinar region. Lung compliance increased in the emphysematous condition where alveolar sacs tended to distend easily but empties slowly. Emphysema increased the required energy for breathing cycle and higher TVs value resulted in higher WOB. On the contrary to stress, strain values diminished in the emphysematous state which could instigate problem for breathing under MV condition. Comparison between results for different TVs for both healthy and emphysematous alveolar models displayed that recommended TVs for patients with COPD increased strain and increased applied stress and WSS compare to emphysematous model with TV equal to 500 mL. Decreasing TV for ARDS would decrease applied strain and stress on the model but increased applied WSS, specifically towards the bottom part of the model. It

was demonstrated that higher TVs for emphysematous alveolar sacs with ARDS decreased maximum WSS while it increased applied stress and strain on the model. Results from this study provide invaluable insights for specialists to set appropriate TVs for patients under MV conditions.

In Chapter 3, influence of age-related changes on alveolar sacs functionality and sensitivity of alveolar sacs mechanics to MV devices protocols were investigated. It was concluded that older alveolar sacs sustain lower pressure compared to younger alveolar sacs models. Findings also indicated that morphological changes have a major impact on decline in alveolar sacs function. Alveolar sacs enlargement in older models led to a decrease in compliance of alveolar sacs and WOB. Although WOB is decreased in single alveolar sacs, an increase in the rigidity of the chest wall would neutralize this decrease in WOB. In reality, WOB would increase in older patients. It was observed that applied pressure on alveolar sacs wall decreased in volume targeted mode and WOB increased in volume-controlled mode as compared to pressure-controlled mode while compliance decreased significantly in volume-controlled mode. The results of sensitivity of alveolar sacs under volume-controlled mode showed that their function is highly sensitive to I/E and breathing frequency. Therefore, increasing frequency and decreasing I/E would increase alveolar sacs expansion and compliance. Decreasing TV decreases WOB while increases in the other two parameters increases WOB. Consequently, increasing breathing frequency and decreasing I/E and TV would help improve breathing conditions for older patients under MV.

In Chapter 4, FD of the bronchial tree was employed as morphological measure to evaluate lung disease quantitatively. In addition, equivalent electrical model was used to investigate the influence of age, asthma and COPD on airways resistance, inertance and compliance. It was observed that airways radius versus bifurcation level can be represented by power-law distribution, which shows scale-free properties of bronchial trees. It was concluded that asthma increased FD while COPD decreased FD significantly and FD declines as we get older in normal and COPD cases whereas it rises in lung with asthma. Changes in mechanical prop-

erties of airways at different bifurcation level from 50 to 80-year-old is more significant than changes from 20 to 50-year-old. Lower generations sustain bigger changes compare to upper airways. Asthma mostly increased airways resistance and air inertia at lower airways while COPD increased discussed parameters at upper airways. Changes in air inertance with age is not as big as changes in airways resistance with age. Asthma declined airways compliance compare to the normal condition and COPD significantly increased airways compliance at lower airways.

In Chapter 5, multiscale model was employed to investigate the population dynamics of cell constituents of alveolar sacs' tissue under MV for different strain levels associated with different TVs. It was observed that strain is highly concentrated in the inlet area and middle layers in the alveolar region underwent higher level of strain during breathing in the MV condition. It was concluded that strain distribution plays a significant role in cells population dynamics and the interplay between strain magnitude and distribution determines healing effectiveness. Results from this study suggest that increasing TV leads to an exponential rise in damage on tissue by inflammation.

According to the observations from this dissertation following hypotheses will be investigated:

- A comprehensive model has to be developed to investigate influence of the tissue microenvironment on strain-induced inflammation mechanism in young and old lungs. Onset and progress of chronic inflammation can be investigated by integrating the results from macroscopic level of young and old lung tissue into cellular level. In addition, multiscale models can be developed to explore the influence of resolution speed, degree of strain in young and old case studies.
- Influence of tissue heterogeneity and heterogeneous populations of cell types can be considered in evaluation of respiratory disease. This can provide better understanding of changes that might happen in mechanics of breathing in diseased condition specifically in ARDS condition.

- Human pulmonary sacs can be considered as linear-parameter-varying system with age as scheduling variable to monitor effects of ventilator parameters specially for diseased conditions. By employing this technique, ventilator protocols can be controlled according to the mechanics of breathing as outputs of this system.

BIBLIOGRAPHY

- [1] P. Aghasafari, I. B. Ibrahim, R. M. Pidaparti, Investigation of the effects of emphysema and influenza on alveolar sacs closure through cfd simulation, *Journal of Biomedical Science and Engineering* 9 (06) (2016) 287.
- [2] M. C. Kneyber, H. Zhang, A. S. Slutsky, Ventilator-induced lung injury. similarity and differences between children and adults, *American journal of respiratory and critical care medicine* 190 (3) (2014) 258–265.
- [3] Y. Iwao, T. Gotoh, S. Kagei, T. Iwasawa, M. d. S. G. Tsuzuki, Integrated lung field segmentation of injured region with anatomical structure analysis by failure–recovery algorithm from chest ct images, *Biomedical Signal Processing and Control* 12 (2014) 28–38.
- [4] T. Nelson, D. Manchester, Modeling of lung morphogenesis using fractal geometries, *IEEE transactions on medical imaging* 7 (4) (1988) 321–327.
- [5] E. J. Berg, J. L. Weisman, M. J. Oldham, R. J. Robinson, Flow field analysis in a compliant acinus replica model using particle image velocimetry (piv), *Journal of biomechanics* 43 (6) (2010) 1039–1047.
- [6] A. Tippe, A. Tsuda, Recirculating flow in an expanding alveolar model: experimental evidence of flow-induced mixing of aerosols in the pulmonary acinus, *Journal of Aerosol Science* 31 (8) (2000) 979–986.
- [7] K. Schirrmann, M. Mertens, U. Kertzscher, W. M. Kuebler, K. Affeld, Theoretical modeling of the interaction between alveoli during inflation and deflation in normal and diseased lungs, *Journal of biomechanics* 43 (6) (2010) 1202–1207.

- [8] J. H. Bates, C. G. Irvin, Time dependence of recruitment and derecruitment in the lung: a theoretical model, *Journal of Applied Physiology* 93 (2) (2002) 705–713.
- [9] C. Schranz, P. D. Docherty, Y. S. Chiew, J. G. Chase, K. Möller, Structural identifiability and practical applicability of an alveolar recruitment model for ards patients, *IEEE Transactions on Biomedical Engineering* 59 (12) (2012) 3396–3404.
- [10] C. H. Weiss, D. W. Baker, S. Weiner, M. Bechel, M. Ragland, A. Rademaker, B. B. Weitner, A. Agrawal, R. G. Wunderink, S. D. Persell, Low tidal volume ventilation use in acute respiratory distress syndrome, *Critical care medicine* 44 (8) (2016) 1515.
- [11] W. Wang, A. Das, T. Ali, O. Cole, M. Chikhani, M. Haque, J. G. Hardman, D. G. Bates, Can computer simulators accurately represent the pathophysiology of individual copd patients?, *Intensive care medicine experimental* 2 (1) (2014) 23.
- [12] S. Christley, B. Emr, A. Ghosh, J. Satalin, L. Gatto, Y. Vodovotz, G. F. Nieman, G. An, Bayesian inference of the lung alveolar spatial model for the identification of alveolar mechanics associated with acute respiratory distress syndrome, *Physical biology* 10 (3) (2013) 036008.
- [13] H. D. Foda, E. E. Rollo, M. Drews, C. Conner, K. Appelt, D. R. Shalinsky, S. Zucker, Ventilator-induced lung injury upregulates and activates gelatinases and emmprin: attenuation by the synthetic matrix metalloproteinase inhibitor, prinomastat (ag3340), *American Journal of Respiratory Cell and Molecular Biology* 25 (6) (2001) 717–724.
- [14] I. B. Copland, B. P. Kavanagh, D. Engelberts, C. McKerlie, J. Belik, M. Post, Early changes in lung gene expression due to high tidal volume, *American journal of respiratory and critical care medicine* 168 (9) (2003) 1051–1059.
- [15] P. H. Carnell, R. P. Vito, W. R. Taylor, Characterizing intramural stress and inflammation in hypertensive arterial bifurcations, *Biomechanics and modeling in mechanobiology* 6 (6) (2007) 409–421.

- [16] F. E. Lennon, G. C. Cianci, N. A. Cipriani, T. A. Hensing, H. J. Zhang, C.-T. Chen, S. D. Murgu, E. E. Vokes, M. W. Vannier, R. Salgia, Lung cancera fractal viewpoint, *Nature reviews Clinical oncology* 12 (11) (2015) 664.
- [17] L. K. Uahabi, M. Atounti, New approach to the calculation of fractal dimension of the lungs, *Annals of the University of Craiova-Mathematics and Computer Science Series* 44 (1) (2017) 78–86.
- [18] S. Kido, K. Kuriyama, M. Higashiyama, T. Kasugai, C. Kuroda, Fractal analysis of internal and peripheral textures of small peripheral bronchogenic carcinomas in thin-section computed tomography: comparison of bronchioloalveolar cell carcinomas with nonbronchioloalveolar cell carcinomas, *Journal of computer assisted tomography* 27 (1) (2003) 56–61.
- [19] S. Haitao, L. Ning, G. Lijun, G. Fei, L. Cheng, Fractal dimension analysis of mdct images for quantifying the morphological changes of the pulmonary artery tree in patients with pulmonary hypertension, *Korean journal of radiology* 12 (3) (2011) 289–296.
- [20] S. Moledina, A. de Bruyn, S. Schievano, C. M. Owens, C. Young, S. G. Haworth, A. M. Taylor, I. Schulze-Neick, V. Muthurangu, Fractal branching quantifies vascular changes and predicts survival in pulmonary hypertension: a proof of principle study, *Heart* (2011) hrt–2010.
- [21] M. Helmberger, M. Pienn, M. Urschler, P. Kullnig, R. Stollberger, G. Kovacs, A. Olschewski, H. Olschewski, Z. Bálint, Quantification of tortuosity and fractal dimension of the lung vessels in pulmonary hypertension patients, *PloS one* 9 (1) (2014) e87515.

- [22] C. M. Ionescu, P. Segers, R. De Keyser, Mechanical properties of the respiratory system derived from morphologic insight, *IEEE Transactions on Biomedical Engineering* 56 (4) (2009) 949–959.
- [23] D. Copot, R. De Keyser, E. Derom, C. Ionescu, Structural changes in the copd lung and related heterogeneity, *PloS one* 12 (5) (2017) e0177969.
- [24] C. Mittman, N. H. Edelman, A. H. Norris, N. W. Shock, Relationship between chest wall and pulmonary compliance and age, *Journal of Applied Physiology* 20 (6) (1965) 1211–1216.
- [25] M. Estenne, J. C. Yernault, A. De Troyer, Rib cage and diaphragm-abdomen compliance in humans: effects of age and posture, *Journal of Applied Physiology* 59 (6) (1985) 1842–1848.
- [26] J.-P. Janssens, J.-C. Pache, L. Nicod, Physiological changes in respiratory function associated with ageing, *European Respiratory Journal* 13 (1) (1999) 197–205.
- [27] P. M. Lalley, The aging respiratory systempulmonary structure, function and neural control, *Respiratory physiology & neurobiology* 187 (3) (2013) 199–210.
- [28] M. F. Lutfi, The physiological basis and clinical significance of lung volume measurements, *Multidisciplinary respiratory medicine* 12 (1) (2017) 3.
- [29] W. Wahba, Influence of aging on lung function-clinical significance of changes from age twenty., *Anesthesia & Analgesia* 62 (8) (1983) 764–776.
- [30] R. J. Shephard, Aging, respiratory function, and exercise, *Journal of Aging and physical Activity* 1 (1) (1993) 59–83.
- [31] G. Sharma, J. Goodwin, Effect of aging on respiratory system physiology and immunology, *Clinical interventions in aging* 1 (3) (2006) 253.

- [32] J. M. Turner, J. Mead, M. E. Wohl, Elasticity of human lungs in relation to age, *Journal of applied physiology* 25 (6) (1968) 664–671.
- [33] D. E. Niewoehner, J. Kleinerman, L. Liotta, Elastic behavior of postmortem human lungs: effects of aging and mild emphysema, *Journal of Applied Physiology* 39 (6) (1975) 943–949.
- [34] L. A. Cox Jr, A causal model of chronic obstructive pulmonary disease (copd) risk, *Risk Analysis: An International Journal* 31 (1) (2011) 38–62.
- [35] J. Lee, F. R. Adler, P. S. Kim, A mathematical model for the macrophage response to respiratory viral infection in normal and asthmatic conditions, *Bulletin of mathematical biology* 79 (9) (2017) 1979–1998.
- [36] B. Brook, S. Peel, I. Hall, A. Politi, J. Sneyd, Y. Bai, M. Sanderson, O. Jensen, A biomechanical model of agonist-initiated contraction in the asthmatic airway, *Respiratory physiology & neurobiology* 170 (1) (2010) 44–58.
- [37] B. N. Brown, I. M. Price, F. R. Toapanta, D. R. DeAlmeida, C. A. Wiley, T. M. Ross, T. D. Oury, Y. Vodovotz, An agent-based model of inflammation and fibrosis following particulate exposure in the lung, *Mathematical biosciences* 231 (2) (2011) 186–196.
- [38] D. E. Moulton, A. Goriely, Possible role of differential growth in airway wall remodeling in asthma, *Journal of applied physiology* 110 (4) (2011) 1003–1012.
- [39] I. L. Chernyavsky, H. Croisier, L. A. Chapman, L. S. Kimpton, J. E. Hiorns, B. S. Brook, O. E. Jensen, C. K. Billington, I. P. Hall, S. R. Johnson, The role of inflammation resolution speed in airway smooth muscle mass accumulation in asthma: insight from a theoretical model, *PloS one* 9 (3) (2014) e90162.
- [40] Y.-H. Cheng, S.-H. You, Y.-J. Lin, S.-C. Chen, W.-Y. Chen, W.-C. Chou, N.-H. Hsieh, C.-M. Liao, Mathematical modeling of postcoinfection with influenza a virus

- and streptococcus pneumoniae, with implications for pneumonia and copd-risk assessment, *International journal of chronic obstructive pulmonary disease* 12 (2017) 1973.
- [41] A. Schlender, P. E. Alperin, H. L. Grossman, E. R. Sutherland, Modeling the impact of increased adherence to asthma therapy, *PLoS One* 7 (12) (2012) e51139.
 - [42] Y. Kim, S. Lee, Y.-S. Kim, S. Lawler, Y. S. Gho, Y.-K. Kim, H. J. Hwang, Regulation of th1/th2 cells in asthma development: a mathematical model, *Mathematical Biosciences & Engineering* 10 (4) (2013) 1095–1133.
 - [43] E. J. Weinberg, F. J. Schoen, M. R. Mofrad, A computational model of aging and calcification in the aortic heart valve, *PLoS One* 4 (6) (2009) e5960.
 - [44] M. T. Mc Auley, K. M. Mooney, Computational systems biology for aging research, in: *Aging and Health-A Systems Biology Perspective*, Vol. 40, Karger Publishers, 2015, pp. 35–48.
 - [45] M. T. Mc Auley, K. M. Mooney, Computationally modeling lipid metabolism and aging: a mini-review, *Computational and structural biotechnology journal* 13 (2015) 38–46.
 - [46] K. M. Mooney, A. E. Morgan, M. T. Mc Auley, Aging and computational systems biology, *Wiley Interdisciplinary Reviews: Systems Biology and Medicine* 8 (2) (2016) 123–139.
 - [47] T. M. Witten, Modeling cellular aging: An introduction–mathematical and computational approaches, in: *Cellular Ageing and Replicative Senescence*, Springer, 2016, pp. 117–141.
 - [48] R. Athanazio, Airway disease: similarities and differences between asthma, copd and bronchiectasis, *Clinics* 67 (11) (2012) 1335–1343.

- [49] M. Shorofsky, D. Jayaraman, F. Lellouche, R. Husa, J. Lipes, Mechanical ventilation with high tidal volume and associated mortality in the cardiac intensive care unit, *Acute cardiac care* 16 (1) (2014) 9–14.
- [50] R. M. Reddy, K. K. Guntupalli, Review of ventilatory techniques to optimize mechanical ventilation in acute exacerbation of chronic obstructive pulmonary disease, *International journal of chronic obstructive pulmonary disease* 2 (4) (2007) 441.
- [51] D. M. Needham, T. Yang, V. D. Dinglas, P. A. Mendez-Tellez, C. Shanholtz, J. E. Sevransky, R. G. Brower, P. J. Pronovost, E. Colantuoni, Timing of low tidal volume ventilation and intensive care unit mortality in acute respiratory distress syndrome. a prospective cohort study, *American journal of respiratory and critical care medicine* 191 (2) (2015) 177–185.
- [52] S. Perinel-Ragey, L. Baboi, C. Guérin, Variability of tidal volume in patient-triggered mechanical ventilation in ards, *Respiratory care* 62 (11) (2017) 1437–1446.
- [53] F. Cinkotai, Fluid flow in a model alveolar sac., *Journal of applied physiology* 37 (2) (1974) 249–251.
- [54] J. Sznitman, Respiratory microflows in the pulmonary acinus, *Journal of biomechanics* 46 (2) (2013) 284–298.
- [55] E. J. Berg, R. J. Robinson, Stereoscopic particle image velocimetry analysis of healthy and emphysemic alveolar sac models, *Journal of Biomechanical Engineering* 133 (6) (2011) 061004.
- [56] J. M. Oakes, S. Day, S. J. Weinstein, R. J. Robinson, Flow field analysis in expanding healthy and emphysematous alveolar models using particle image velocimetry, *Journal of Biomechanical Engineering* 132 (2) (2010) 021008.

- [57] J. M. Oakes, P. Hofemeier, I. E. Vignon-Clementel, J. Sznitman, Aerosols in healthy and emphysematous in silico pulmonary acinar rat models, *Journal of biomechanics* 49 (11) (2016) 2213–2220.
- [58] C. Van Ertbruggen, P. Corieri, R. Theunissen, M. Riethmuller, C. Darquenne, Validation of cfd predictions of flow in a 3d alveolated bend with experimental data, *Journal of biomechanics* 41 (2) (2008) 399–405.
- [59] B. Ma, V. Ruwet, P. Corieri, R. Theunissen, M. Riethmuller, C. Darquenne, Cfd simulation and experimental validation of fluid flow and particle transport in a model of alveolated airways, *Journal of aerosol science* 40 (5) (2009) 403–414.
- [60] S. Chhabra, A. K. Prasad, Flow and particle dispersion in a pulmonary alveoluspart i: Velocity measurements and convective particle transport, *Journal of biomechanical engineering* 132 (5) (2010) 051009.
- [61] S. Chhabra, A. K. Prasad, Flow and particle dispersion in a pulmonary alveoluspart ii: Effect of gravity on particle transport, *Journal of biomechanical engineering* 132 (5) (2010) 051010.
- [62] R. Fishler, M. K. Mulligan, J. Sznitman, Acinus-on-a-chip: a microfluidic platform for pulmonary acinar flows, *Journal of biomechanics* 46 (16) (2013) 2817–2823.
- [63] H. Tavana, C.-H. Kuo, Q. Y. Lee, B. Mosadegh, D. Huh, P. J. Christensen, J. B. Grotberg, S. Takayama, Dynamics of liquid plugs of buffer and surfactant solutions in a micro-engineered pulmonary airway model, *Langmuir* 26 (5) (2009) 3744–3752.
- [64] B. Huo, R.-R. Fu, Recent advances in theoretical models of respiratory mechanics, *Acta Mechanica Sinica* 28 (1) (2012) 1–7.
- [65] S. Casarin, F. Aletti, G. Baselli, M. Garbey, Optimal flow conditions of a tracheo-bronchial model to reengineer lung structures, *Acta Mechanica Sinica* 33 (2) (2017) 284–294.

- [66] W. J. Federspiel, J. J. Fredberg, Axial dispersion in respiratory bronchioles and alveolar ducts, *Journal of Applied Physiology* 64 (6) (1988) 2614–2621.
- [67] A. Tsuda, W. J. Federspiel, P. A. Grant Jr, J. J. Fredberg, Axial dispersion of inert species in alveolated channels, *Chemical Engineering Science* 46 (5-6) (1991) 1419–1426.
- [68] M. H. Tawhai, C.-L. Lin, Image-based modeling of lung structure and function, *Journal of Magnetic Resonance Imaging* 32 (6) (2010) 1421–1431.
- [69] H. L. Dailey, S. Ghadiali, Fluid-structure analysis of microparticle transport in deformable pulmonary alveoli, *Journal of Aerosol Science* 38 (3) (2007) 269–288.
- [70] J. R. Fitz-Clarke, Mechanics of airway and alveolar collapse in human breath-hold diving, *Respiratory physiology & neurobiology* 159 (2) (2007) 202–210.
- [71] J. de Ryk, J. Thiesse, E. Namati, G. McLennan, Stress distribution in a three dimensional, geometric alveolar sac under normal and emphysematous conditions, *International journal of chronic obstructive pulmonary disease* 2 (1) (2007) 81.
- [72] J. H. Bates, B. J. Smith, G. B. Allen, Computational models of ventilator induced lung injury and surfactant dysfunction, *Drug Discovery Today: Disease Models* 15 (2015) 17–22.
- [73] I. Grossbach, L. Chlan, M. F. Tracy, Overview of mechanical ventilatory support and management of patient-and ventilator-related responses, *Critical care nurse* 31 (3) (2011) 30–44.
- [74] H.-J. Bungartz, M. Schäfer, Fluid-structure interaction: modelling, simulation, optimisation, Vol. 53, Springer Science & Business Media, 2006.
- [75] S. Lin, X. Han, Y. Bi, S. Ju, L. Gu, Fluid-structure interaction in abdominal aortic aneurysm: Effect of modeling techniques, *BioMed research international* 2017.

- [76] H. Kumar, M. H. Tawhai, E. A. Hoffman, C.-L. Lin, The effects of geometry on airflow in the acinar region of the human lung, *Journal of biomechanics* 42 (11) (2009) 1635–1642.
- [77] P. Gehr, M. Bachofen, E. R. Weibel, The normal human lung: ultrastructure and morphometric estimation of diffusion capacity, *Respiration physiology* 32 (2) (1978) 121–140.
- [78] J. E. Hansen, E. P. Ampaya, Human air space shapes, sizes, areas, and volumes, *Journal of Applied Physiology* 38 (6) (1975) 990–995.
- [79] T. G. Klingele, N. C. Staub, Alveolar shape changes with volume in isolated, air-filled lobes of cat lung, *Journal of Applied Physiology* 28 (4) (1970) 411–414.
- [80] B. Haefeli-Bleuer, E. R. Weibel, Morphometry of the human pulmonary acinus, *The Anatomical Record* 220 (4) (1988) 401–414.
- [81] E. R. Weibel, Morphometrics of the lung, *Handbook of physiology. Respiration* 1 (1964) 285–307.
- [82] B. Ma, C. Darquenne, Aerosol deposition characteristics in distal acinar airways under cyclic breathing conditions, *Journal of Applied physiology* 110 (5) (2011) 1271–1282.
- [83] P. Aghasafari, I. B. M. Ibrahim, R. Pidaparti, Strain-induced inflammation in pulmonary alveolar tissue due to mechanical ventilation, *Biomechanics and modeling in mechanobiology* 16 (4) (2017) 1103–1118.
- [84] Y. Liu, R. So, C. Zhang, Modeling the bifurcating flow in a human lung airway, *Journal of biomechanics* 35 (4) (2002) 465–473.
- [85] D. Wu, X. Jiang, S. Li, L. Wang, A new transient cfd method for determining the dynamic coefficients of liquid annular seals, *Journal of Mechanical Science and Technology* 30 (8) (2016) 3477–3486.

- [86] S. J. Lai-Fook, R. E. Hyatt, Effects of age on elastic moduli of human lungs, *Journal of applied physiology* 89 (1) (2000) 163–168.
- [87] B. Suki, E. Bartolák-Suki, Biomechanics of the aging lung parenchyma, in: *Mechanical Properties of Aging Soft Tissues*, Springer, 2015, pp. 95–133.
- [88] D. Papandrinopoulou, V. Tzouda, G. Tsoukalas, Lung compliance and chronic obstructive pulmonary disease, *Pulmonary medicine* 2012.
- [89] C. A. Vaz Fragoso, T. M. Gill, Respiratory impairment and the aging lung: a novel paradigm for assessing pulmonary function, *Journals of Gerontology Series A: Biomedical Sciences and Medical Sciences* 67 (3) (2011) 264–275.
- [90] J. Tallis, R. S. James, A. G. Little, V. M. Cox, M. J. Duncan, F. Seebacher, Early effects of ageing on the mechanical performance of isolated locomotory (edl) and respiratory (diaphragm) skeletal muscle using the work-loop technique, *American Journal of Physiology-Regulatory, Integrative and Comparative Physiology* 307 (6) (2014) R670–R684.
- [91] J. D. Quirk, A. L. Sukstanskii, J. C. Woods, B. A. Lutey, M. S. Conradi, D. S. Gierada, R. D. Yusen, M. Castro, D. A. Yablonskiy, Experimental evidence of age-related adaptive changes in human acinar airways, *Journal of Applied Physiology* 120 (2) (2015) 159–165.
- [92] C. Brandenberger, C. Mühlfeld, Mechanisms of lung aging, *Cell and tissue research* 367 (3) (2017) 469–480.
- [93] K. Kvell, J. E. Pongracz, Immunosenescence and the ageing lung, in: *The Ageing Immune System and Health*, Springer, 2017, pp. 87–104.
- [94] K. Subramaniam, H. Kumar, M. H. Tawhai, Evidence for age-dependent air-space enlargement contributing to loss of lung tissue elastic recoil pressure and increased shear modulus in older age, *Journal of Applied Physiology* 123 (1) (2017) 79–87.

- [95] E. K. Verbeken, M. Cauberghs, I. Mertens, J. Clement, J. M. Lauweryns, K. P. Van de Woestijne, The senile lung: comparison with normal and emphysematous lungs 1. structural aspects, *Chest* 101 (3) (1992) 793–799.
- [96] G. S. Budinger, R. A. Kohanski, W. Gan, M. S. Kobor, L. A. Amaral, M. Armanios, K. T. Kelsey, A. Pardo, R. Tudor, F. Macian, et al., The intersection of aging biology and the pathobiology of lung diseases: A joint nhlbi/nia workshop, *Journals of Gerontology Series A: Biomedical Sciences and Medical Sciences* 72 (11) (2017) 1492–1500.
- [97] L. Chen, G.-Q. Chen, K. Shore, O. Shklar, C. Martins, B. Devenyi, P. Lindsay, H. McPhail, A. Lanys, I. Soliman, et al., Implementing a bedside assessment of respiratory mechanics in patients with acute respiratory distress syndrome, *Critical Care* 21 (1) (2017) 84.
- [98] D. W. Chang, *Clinical application of mechanical ventilation*, Cengage Learning, 2013.
- [99] C. Corbellini, C. B. E. Trevisan, J. H. Villafañe, A. D. Da Costa, S. R. R. Vieira, Weaning from mechanical ventilation: a cross-sectional study of reference values and the discriminative validity of aging, *Journal of physical therapy science* 27 (6) (2015) 1945–1950.
- [100] A. Fluent, 14.0 tutorial guide ansys inc, Canonsburg, PA 2.
- [101] K. L. Lawrence, *ANSYS workbench tutorial release 14*, SDC publications, 2012.
- [102] F.-K. Benra, H. J. Dohmen, J. Pei, S. Schuster, B. Wan, A comparison of one-way and two-way coupling methods for numerical analysis of fluid-structure interactions, *Journal of applied mathematics* 2011.
- [103] B. B. Mandelbrot, *The fractal geometry of nature*, Vol. 173, WH freeman New York, 1983.

- [104] D. Ristanović, N. T. Milošević, Fractal analysis: methodologies for biomedical researchers., in: Theoretical biology forum, Vol. 105, Fabrizio Serra, 2012, pp. 99–118.
- [105] B. J. He, Scale-free brain activity: past, present, and future, Trends in cognitive sciences 18 (9) (2014) 480–487.
- [106] B. B. Mandelbrot, The fractal geometry of nature/revised and enlarged edition, New York, WH Freeman and Co., 1983, 495 p.
- [107] A. Di Ieva, F. Grizzi, G. Ceva-Grimaldi, C. Russo, P. Gaetani, E. Aimar, D. Levi, P. Pisano, F. Tancioni, G. Nicola, et al., Fractal dimension as a quantitator of the microvasculature of normal and adenomatous pituitary tissue, Journal of anatomy 211 (5) (2007) 673–680.
- [108] R. Lopes, N. Betrouni, Fractal and multifractal analysis: a review, Medical image analysis 13 (4) (2009) 634–649.
- [109] A. Karperien, H. Ahammer, H. Jelinek, Quantitating the subtleties of microglial morphology with fractal analysis, Frontiers in cellular neuroscience 7 (2013) 3.
- [110] V. D. Varner, C. M. Nelson, Computational models of airway branching morphogenesis, in: Seminars in cell & developmental biology, Vol. 67, Elsevier, 2017, pp. 170–176.
- [111] J. Kim, R. L. Heise, A. M. Reynolds, R. M. Pidaparti, Quantification of age-related lung tissue mechanics under mechanical ventilation, Medical Sciences 5 (4) (2017) 21.
- [112] P. Aghasafari, R. L. Heise, A. Reynolds, R. Pidaparti, Aging effects on alveolar sacs under mechanical ventilation., The Journals of Gerontology: Series A (2018) gly097.
- [113] L.-F. Li, B. Ouyang, G. Choukroun, R. Matyal, M. Mascarenhas, B. Jafari, J. V. Bonventre, T. Force, D. A. Quinn, Stretch-induced il-8 depends on c-jun nh2-terminal and nuclear factor- κ b-inducing kinases, American Journal of Physiology-Lung Cellular and Molecular Physiology 285 (2) (2003) L464–L475.

- [114] L.-F. Li, L. Yu, D. A. Quinn, Ventilation-induced neutrophil infiltration depends on c-jun n-terminal kinase, *American journal of respiratory and critical care medicine* 169 (4) (2004) 518–524.
- [115] S. Oudin, J. Pugin, Role of map kinase activation in interleukin-8 production by human beas-2b bronchial epithelial cells submitted to cyclic stretch, *American journal of respiratory cell and molecular biology* 27 (1) (2002) 107–114.
- [116] U. Uhlig, J. Haitsma, T. Goldmann, D. Poelma, B. Lachmann, S. Uhlig, Ventilation-induced activation of the mitogen-activated protein kinase pathway, *European Respiratory Journal* 20 (4) (2002) 946–956.
- [117] M. M. Mascarenhas, R. M. Day, C. D. Ochoa, W.-I. Choi, L. Yu, B. Ouyang, H. G. Garg, C. A. Hales, D. A. Quinn, Low molecular weight hyaluronan from stretched lung enhances interleukin-8 expression, *American journal of respiratory cell and molecular biology* 30 (1) (2004) 51–60.
- [118] N. A. Haseneen, G. G. Vaday, S. Zucker, H. D. Foda, Mechanical stretch induces mmp-2 release and activation in lung endothelium: role of emmprin, *American Journal of Physiology-Lung Cellular and Molecular Physiology* 284 (3) (2003) L541–L547.
- [119] K. G. Birukov, J. R. Jacobson, A. A. Flores, S. Q. Ye, A. A. Birukova, A. D. Verin, J. G. Garcia, Magnitude-dependent regulation of pulmonary endothelial cell barrier function by cyclic stretch, *American Journal of Physiology-Lung Cellular and Molecular Physiology* 285 (4) (2003) L785–L797.
- [120] J. Pugin, I. Dunn, P. Jolliet, D. Tassaux, J.-L. Magnenat, L. P. Nicod, J.-C. Chevrolet, Activation of human macrophages by mechanical ventilation in vitro, *American Journal of Physiology-Lung Cellular and Molecular Physiology* 275 (6) (1998) L1040–L1050.
- [121] W. M. Kuebler, U. Uhlig, T. Goldmann, G. Schael, A. Kerem, K. Exner, C. Martin, E. Vollmer, S. Uhlig, Stretch activates nitric oxide production in pulmonary vascular

- endothelial cells in situ, *American journal of respiratory and critical care medicine* 168 (11) (2003) 1391–1398.
- [122] E. M. Harding Jr, R. J. Robinson, Flow in a terminal alveolar sac model with expanding walls using computational fluid dynamics, *Inhalation toxicology* 22 (8) (2010) 669–678.
- [123] A. R. Clark, K. S. Burrowes, M. H. Tawhai, Contribution of serial and parallel microp-
erfusion to spatial variability in pulmonary inter-and intra-acinar blood flow, *Journal
of applied physiology* 108 (5) (2010) 1116–1126.
- [124] A. V. Kolanjiyil, C. Kleinstreuer, Nanoparticle mass transfer from lung airways to sys-
temic regions part i: whole-lung aerosol dynamics, *Journal of biomechanical engineering*
135 (12) (2013) 121003.
- [125] S. Tang, Y. Li, Y. Yang, Z. Guo, The effect of mechanical-driven volumetric change
on instability patterns of bilayered soft solids, *Soft Matter* 11 (40) (2015) 7911–7919.
- [126] L. Wiechert, R. Metzke, W. A. Wall, Modeling the mechanical behavior of lung tissue
at the microlevel, *Journal of engineering mechanics* 135 (5) (2009) 434–438.
- [127] F. S. Cavalcante, S. Ito, K. Brewer, H. Sakai, A. M. Alencar, M. P. Almeida, J. S.
Andrade Jr, A. Majumdar, E. P. Ingenito, B. Suki, Mechanical interactions between
collagen and proteoglycans: implications for the stability of lung tissue, *Journal of
applied physiology* 98 (2) (2005) 672–679.
- [128] A. Gefen, D. Elad, R. Shiner, Analysis of stress distribution in the alveolar septa
of normal and simulated emphysematic lungs, *Journal of biomechanics* 32 (9) (1999)
891–897.
- [129] B. Chopard, Cellular automata modeling of physical systems, in: *Computational Com-
plexity*, Springer, 2012, pp. 407–433.

- [130] G. B. Ermentrout, L. Edelstein-Keshet, Cellular automata approaches to biological modeling, *Journal of theoretical Biology* 160 (1) (1993) 97–133.
- [131] D. Alemani, F. Pappalardo, M. Pennisi, S. Motta, V. Brusici, Combining cellular automata and lattice boltzmann method to model multiscale avascular tumor growth coupled with nutrient diffusion and immune competition, *Journal of Immunological Methods* 376 (1-2) (2012) 55–68.
- [132] M. Precharattana, W. Triampo, Modeling dynamics of hiv infected cells using stochastic cellular automaton, *Physica A: Statistical Mechanics and its Applications* 407 (2014) 303–311.
- [133] A. Reynolds, K. Koombua, R. M. Pidaparti, K. R. Ward, Cellular automata modeling of pulmonary inflammation, *Molecular & Cellular Biomechanics* 9 (2) (2012) 141–156.
- [134] J. Dutta-Moscato, A. Solovyev, Q. Mi, T. Nishikawa, A. Soto-Gutierrez, I. J. Fox, Y. Vodovotz, A multiscale agent-based in silico model of liver fibrosis progression, *Frontiers in bioengineering and biotechnology* 2 (2014) 18.
- [135] Y. Tanabe, M. Saito, A. Ueno, M. Nakamura, K. Takeishi, K. Nakayama, Mechanical stretch augments pdgf receptor β expression and protein tyrosine phosphorylation in pulmonary artery tissue and smooth muscle cells, *Molecular and cellular biochemistry* 215 (1-2) (2000) 103–113.
- [136] K. Moriyama, A. Ishizaka, M. Nakamura, H. Kubo, T. Kotani, S. Yamamoto, E. N. Ogawa, O. Kajikawa, C. W. Frevert, Y. Kotake, et al., Enhancement of the endotoxin recognition pathway by ventilation with a large tidal volume in rabbits, *American Journal of Physiology-Lung Cellular and Molecular Physiology* 286 (6) (2004) L1114–L1121.
- [137] S. UHLIG, U. UHLIG, Molecular mechanisms of pro-inflammatory responses in over-ventilated lungs, 2001.

- [138] F. Halbertsma, M. Vaneker, G. Scheffer, J. Van der Hoeven, Cytokines and biotrauma in ventilator-induced lung injury: a critical review of the literature, *Neth J Med* 63 (10) (2005) 382–392.
- [139] C.-K. Wong, M. C. Easton, An efficient method for weighted sampling without replacement, *SIAM Journal on Computing* 9 (1) (1980) 111–113.
- [140] K. D. Estrada, N. C. Chesler, Collagen-related gene and protein expression changes in the lung in response to chronic hypoxia, *Biomechanics and modeling in mechanobiology* 8 (4) (2009) 263–272.

APPENDIX A

SUPPLEMENTAL MATERIALS FOR CHAPTER 3

AGING EFFECTS ON ALVEOLAR SACS UNDER MECHANICAL VENTILATION

Table A.1: 50 and 80-year-old Alveolar sacs dimensions.

Morphological parameters				
Parameters	Regression Coefficients (P values)		Measures in this study	
	$(a_0 + a_1 * Age)$		50-year-old	80-year-old
	a_0	a_1		
Lumen Diameter D_L (mm)	240 ± 10 (2.5E-8)	2.6 ± 0.3 (4.0E-4)	0.368	0.448
Alveolus depth D_{alv} (mm)	177 ± 8 (< 2E-16)	-0.87 ± 0.2 (1.1E-4)	0.134	0.108
Mean chord length L_m (mm)	150 ± 20 (4.7E-9)	1.4 ± 0.4 (8.4E-4)	0.223	0.262
Volume (mm³)			0.083	0.104
Wall thickness (mm)			0.025	0.079
Tissue properties parameters				
Bulk modulus (Pa)			2098	2834
Shear modulus (Pa)			308	341

Table A.2: Flow rate waveform

Time	Flowrate waveform
Inhalation	$Flowrate = \frac{TV}{t_{in}}$
Exhalation	$Flowrate = \frac{TV(\exp(t) - \exp(t_t))}{(1 + t_{ex})(\exp(t_t) - \exp(t_{in}))}$
Four breathing cycle patterns	

Table A.3: Morphological and tissue properties of constructed case studies.

Parameters	Case A	Case B	Case C	Case D	Case E	Case F	Case G	Case H	Case I	Case J	Case K	Case L	Case M
Lumen Diameter D_L (mm)	0.219	0.221	0.224	0.226	0.228	0.224	0.224	0.224	0.224	0.224	0.224	0.224	0.224
Alveolus depth D_{alv} (mm)	0.106	0.107	0.108	0.109	0.110	0.108	0.108	0.108	0.108	0.108	0.108	0.108	0.108
Mean chord length L_m (mm)	0.256	0.259	0.262	0.264	0.267	0.262	0.262	0.262	0.262	0.262	0.262	0.262	0.262
Wall thickness (mm)	0.079	0.079	0.079	0.079	0.079	0.077	0.078	0.080	0.081	0.079	0.079	0.079	0.079
Bulk modulus (Pa)	2834	2834	2834	2834	2834	2834	2834	2834	2834	2777	2805	2862	2890
Shear modulus (Pa)	341	341	341	341	341	341	341	341	341	334	337	344	348

Case (A): Duct radius, alveolus depth and mean cord length were decreased by 2% with same alveolar thickness and tissue properties of 80-year-old model, Case (B): Duct radius, alveolus depth and mean cord length were decreased by 1% with same alveolar thickness and tissue properties of 80-year-old model, Case (C): Considered model for 80-year-old alveolar sacs in this study with same alveolar thickness and tissue properties of 80-year-old model (Case 4 in this study), Case (D): Duct radius, alveolus depth and mean cord length were increased by 1% with same alveolar thickness and tissue properties of 80-year-old model, Case (E): Duct radius, alveolus depth and mean cord length were increased by 2% with same alveolar thickness and tissue properties of 80-year-old model, Case (F): Wall thickness was decreased by 2% with same duct radius, alveolus depth, mean cord length and tissue properties of 80-year-old model, Case (G): Wall thickness was decreased by 1% with same duct radius, alveolus depth, mean cord length and tissue properties of 80-year-old model, Case (H): Wall thickness was increased by 1% with same duct radius, alveolus depth, mean cord length and tissue properties of 80-year-old model, Case (I): Wall thickness was increased by 2% with same duct radius, alveolus depth, mean cord length and tissue properties of 80-year-old model, Case (J): Shear and bulk modulus were decreased by 2% with same duct radius, alveolus depth, mean cord length and wall thickness of 80-year-old model, Case (K): Shear and bulk modulus were decreased by 1% with same duct radius, alveolus depth, mean cord length and wall thickness of 80-year-old model, Case (L): Shear and bulk modulus were increased by 1% with same duct radius, alveolus depth, mean cord length and wall thickness of 80-year-old model, Case (M): Shear and bulk modulus were increased by 2% with same duct radius, alveolus depth, mean cord length and wall thickness of 80-year-old model.

Table A.4: z test for compliance and WOB values for considered case studies and measured confidence intervals for alveolar sacs function in elderly.

Parameters	Case A	Case B	Case C	Case D	Case E	Case F	Case G	Case H	Case I	Case J	Case K	Case L	Case M	Mean	SD	Specified value	Confidence interval
Compliance $\times 10^{-7}$	1.16	1.16	1.17	1.15	1.17	1.17	1.16	1.17	1.17	1.18	1.18	1.16	1.15	1.16	9.63E-3	1.17	[1.16 1.17]
Compare to Case C	-0.91%	-0.69%		-1.03%	0.02%	-0.02%	-0.98%	0.44%	0.50%	0.81%	1.04%	-0.24%	-1.8%				
WOB $\times 10^{-7}$	4.53	3.83	4.30	4.19	3.80	4.48	4.37	4.09	4.23	4.42	3.69	4.27	4.22	4.19	2.64E-1	4.30	[4.04 4.33]
Compare to Case C	5.24%	-10.85%		-2.62%	-11.63%	4.19%	1.55%	-4.93%	-1.54%	2.72%	-14.12%	-0.74%	-1.78%				

Negative value in comparison row illustrate the decline in value and positive value illustrate increase in the value.

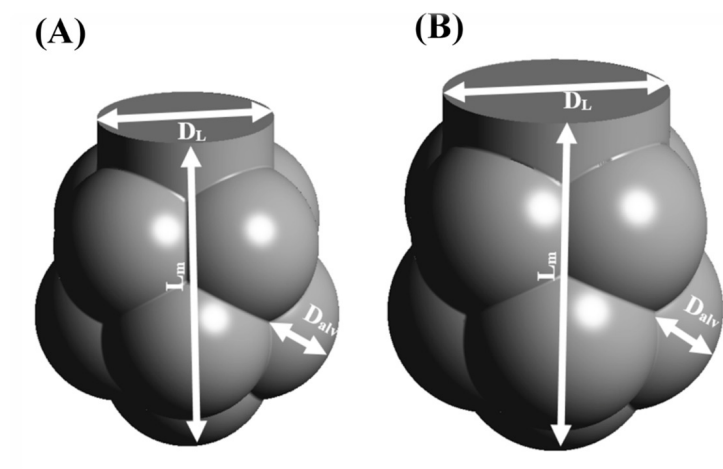


Figure A.1: (A) 50-year-old alveolar sac model, (B) 80-year-old alveolar sac model.

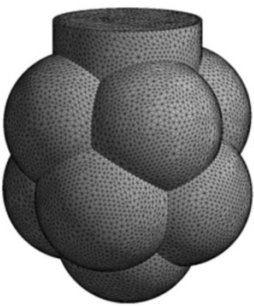
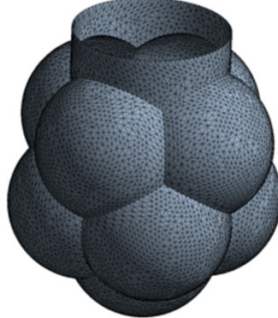
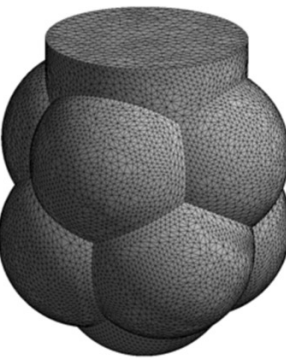
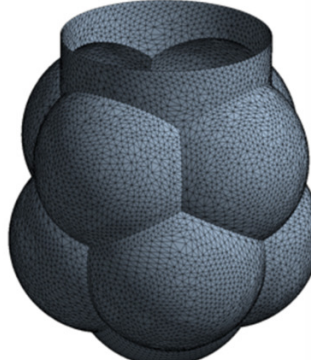
Model	Mesh size	
	Fluid	solid
50-year-old		
Mesh elements	2082543	1784469
80-year-old		
Mesh elements	2104235	1847502

Figure A.2: Mesh size for fluid and solid domain for FSI analysis.

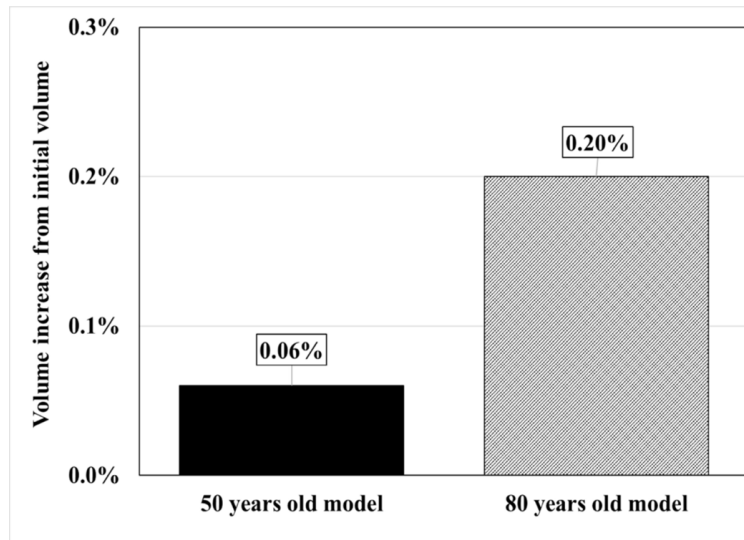


Figure A.3: Volume increase from reference volume in 50 and 80-year-old alveolar sacs .